Theoretical and experimental study of core-shell structured ZnO/ZnS and growth mechanism of un-doped and doped ZnO nanomaterials

By

Leta T. Jule

Promoter: Prof. F.B. Dejene

Co-promoter: Dr. K.T. Roro

SUBMITTED IN PARTIAL FULFILLMENT OF THE
REQUIREMENTS FOR THE DEGREE OF
DOCTOR OF PHILOSOPHY
AT
UNIVERSITY OF THE FREE STATE
REPUBLIC OF SOUTH AFRICA
DECEMBER 2016

Table of Contents

Table of Contents **iv**

Abstract **xvii**

Acknowledgements **xix**

1 Introduction **1**
1.1 Nanostructured ZnO: Historical Overview 1
1.1.1 Luminescent centers and defect Chemistry in ZnO 3
1.1.2 Crystal structures of ZnO 11
1.1.3 Lattice Parameters 12
1.2 Electronic band structure 14
1.3 Basic Properties of ZnO nanostructures 16
1.4 Motivation 17
1.5 Definition of the Research Problem 18
1.6 Objectives of the Research 19
1.7 Outline of the Thesis 19

2 Theoretical Models and the optical response of metal/dielectric composites with electromagnetic wave interactions **22**
2.1 Introduction 22
2.2 Models describing metals and dielectrics 23
2.2.1 Lorentz Model 23
2.2.2 Drude Model 26
2.3 Effective-medium approximation for linear media 28
2.4 Maxwell Garnett theory 29
2.4.1 Coated coherent potential approximation method 32
2.5 Discrete Dipole Approximation 33
2.5.1 Spherical particles: the quasi-static approximation 34
2.6 Modelling optical absorption of nanocomposite using finite difference time domain (FDTD) 37

3 Experimental methods and Characterization techniques **40**
3.1 Growth system and process of ZnO nanostructure materials 40
3.1.1 Precursors 40
3.1.2 Substrate preparation 40
3.1.3 Seed layer preparation 41

3.1.4 Seeding techniques . . . 42
3.1.5 Synthesis of ZnO nanorods . . . 43
3.2 Luminescence in ZnO . . . 45
3.2.1 Free excitons (FX) . . . 47
3.2.2 Bound excitons (BE) . . . 48
3.2.3 Shallow Donor-Acceptor Pair transitions (DAP) . . . 49
3.2.4 Two-electron satellite transitions (TES) . . . 50
3.2.5 Quantum confinement effects . . . 51
3.3 Synthesis of ZnO nanostructures . . . 52
3.3.1 Growth of ZnO nanostructures using chemical bath deposition 54
3.4 Sol-Gel Method . . . 56
3.5 Characterisation techniques . . . 57
3.5.1 X-ray diffraction (XRD) . . . 57
3.5.2 Scanning electron microscopy (SEM) and energy dispersive x-ray spectroscopy (EDX) . . . 59
3.5.3 Photoluminescence (PL) Spectroscopy PL . . . 60
3.5.4 Electron Paramagnetic Resonance (EPR) spectroscopy . . . 62

4 Enhancing absorption in coated semiconductor nanowire/nanorod core-shell arrays using active host matrices 64
4.1 Introduction . . . 64
4.2 Theoretical consideration . . . 66
4.2.1 Background . . . 66
4.2.2 Electrodynamic analysis . . . 67
4.3 Experimental details and Characterizations . . . 71
4.4 Results and discussion . . . 72
4.4.1 Theoretical analysis . . . 72
4.4.2 Experimental analysis . . . 78
4.5 Conclusion . . . 82

5 Rapid synthesis of blue emitting ZnO nanoparticles for fluorescent applications 83
5.1 Introduction . . . 83
5.2 Experiment . . . 84
5.2.1 Sample preparation . . . 84
5.2.2 Characterizations . . . 85
5.3 Results and discussion . . . 85
5.3.1 Structural analysis . . . 85
5.3.2 Morphological analysis . . . 88
5.4 UV-visible spectrophotometer analysis . . . 89
5.5 Photoluminescence analysis . . . 91
5.6 Temperature dependent PL . . . 93
5.7 Conclusion . . . 96

6 Wide visible emission and narrowing band gap in Cd-doped ZnO nanopowders synthesized via sol-gel route 98
6.1 Introduction . . . 98
6.2 Experiment . . . 100
6.2.1 Preparation . . . 100
6.2.2 Characterization . . . 100
6.3 Result and discussions . . . 101
6.3.1 Structural studies . . . 101
6.3.2 Optical properties . . . 104
6.4 Conclusion . . . 111

7 Defect-induced room temperature ferromagnetic properties of the Al-doped and undoped ZnO nanostructure 112
7.1 Introduction . . . 112
7.2 Experiment . . . 114
7.2.1 Preparation . . . 114
7.2.2 Characterization . . . 114
7.3 Result and discussions . . . 115
7.3.1 Structural studies . . . 115
7.4 Conclusion . . . 120
7.4 Conclusion . . . 121

8 Conclusions and future work 122
8.1 Conclusions . . . 122
8.2 Future work . . . 124
8.3 Publications . . . 126

Bibliography 126

List of Figures

1.1 The wurtzite structure model of ZnO. The tetrahedral coordination of ZnO is shown [28]. 4

1.2 Schematic representations of wurtzite ZnO: (a) the primitive unit cell, (b) neighbouring atoms showing tetrahedral coordination where every atom of one kind is surrounded by four atoms of the other kind, and (c) the detailed structure of the wurtzitelattice. Second-nearest-neighbour distances, u, and bond angles $\alpha$and $\beta = 109.47^0$, are also shown [24, 55]. 12

1.3 Low temperature band structure of ZnO showing valence band splitting into three (A, B, C) which is caused by crystal field and spin-orbit splitting [19] (a), and band structure of ZnO calculated using an empirical tight binding Hamiltonian (b). The zero energy in these graphs is taken as the upper edge of the valence band (after [55]). 15

2.1 Lorentz harmonic oscillator [86]. 25

2.2 Hypothetical oscillator response to a driving force at (a) low frequencies, (b) resonance frequency, ω_0, and (c) high frequencies [86]. 25

2.3 Frequency dependence of the real and imaginary parts of the dielectric constant of silver. 27

2.4 Schematic view of a random medium composed of core-shell cylinders of infinite length. The positions of the cylinders are random. The inset is the core-shell dielectric cylinders embedded in the background with a dielectric constant of ε_m. 30

2.5 Schematic view of the CCPA method for random media composed of coreshell dielectric cylinders, illustrated in (a). The coated layer to the actual coreshell cylinders in (b) has the size of r_c and the dielectric constant equal to ε_m. (c) The dashed region indicates the effective scattering unit described in the CCPA method. 32
2.6 (A) Shows schematic view of our model containing unit square cell in the (x, y) plane of a typical core-shell composite structure containing the inclusion and (B) Yee FDTD cell model. 39

3.1 Band diagram illustration of the different processes that make up the photoluminescence spectra: (a) excitation, relaxation and recombination in k-space, and (b) possible mechanisms of e-h recombination [55]. 46
3.2 A typical PL spectrum of a ZnO crystal at room temperature . . . 49
3.3 The X-ray diffractometer used in this study is a Bruker AXS Discover diffractometer. 58
3.4 The SEM equipment coupled with EDX: SHIMADZU Superscan model SSX-550. 60
3.5 Schematic diagrams of typical experimental set-ups for CW-PL measurements using photomultiplier tubes or semiconductor photodiodes. 62

4.1 Structural model for cylindrical core-shell nanowire under consideration together with the relevant parameters. 68
4.2 Imaginary part of refractive index n'' versus z for active host matrices and the numerical values and parameters are $\epsilon_h'' = 0$, $f = 0.001$, $\varepsilon_h' = 2.25$ 74
4.3 Real part of refractive index n' versus dimensionless frequency z with tuned cylindrical nanowire embedded in active host matrices with parameters $\epsilon_h'' = -0.13866$, $\varepsilon_h' = 2.25$ 74
4.4 Imaginary part of refractive index n'' versus dimensionless frequency z with tuned cylindrical nanowire embedded in active host matrices with parameters $\epsilon_h'' = -0.13866$, $\varepsilon_h' = 2.25$ 75
4.5 Imaginary part of refractive index n'' versus frequency z for pure metal cylindrical nanowire in passive host medium $\varepsilon_h'' = 0.0$. 75

4.6 Real part of refractive index n' versus frequency z, for pure metal cylindrical nanowire embedded in passive host(non-absorbing host medium) $\varepsilon_h'' = 0.0$. 76
4.7 SEM micrograph and EDX patterns of ZnS/ZnO core-shell. (a). SEM image A shows after sulphidation of ZnO/ZnS core-shell and image B is the EDX pattern recorded from A. (b). Image C shows the SEM before sulphidation(ZnO nanorod) and image B shows the EDX pattern recorded from C. 78
4.8 XRD patterns of bare ZnO and ZnS/ZnO core-shell). 78
4.9 Two-dimensional plots of the modulus of the local electric field of core-shell structures. The color bar indicates the normal scale in V m^{-1} unit. (a) Resonant state of array of inclusions in the matrix. (b) Field patterns for E_z in the x-y plane (one unit cell) for single rod. (c) Resonant state of single inclusion in the unit cell. (d) Off-resonant state of single inclusion in the matrix 79
4.10 PL intensity vs wavelength emission observed from ZnS coated ZnO nanorod arrays for theoretical comparison. 80

5.1 XRD pattern of ZnO nanoparticles synthesized at various temperatures for 2hr. 86
5.2 Variation of FWHM of (101) x-ray diffraction peaks and estimated particle sizes plotted against decomposition temperature. 87
5.3 Variation of lattice parameter, a and c as a function of temperature. 87
5.4 SEM micrograph and EDX spectrum of ZnO nanoparticles at: (A)300 ^0C. (B)400 ^0C. (C)500 ^0C for $2h$, and D, E and F are the corresponding EDX spectra. 89
5.5 UV-Vis absorbance spectra of ZnO nanoparticles synthesized at different annealing temperatures. 90
5.6 The optical absorption energy band gap estimated using Tauc's plot relation for ZnO nanoparticles synthesized at different annealing temperatures. 91
5.7 PL emission of ZnO nanoparticles synthesized at various temperatures. 93
5.8 Temperature dependent PL emission of ZnO nanoparticles prepared at 200 ^0C. 94

5.9 (A). Temperature dependent PL emission of ZnO nanoparticles prepared at 300 ^0C and (B). shows thermally activated luminescence quenching of the 3.21 eV emission for the ZnO NPs prepared at a temperature of 300 ^0C. 95
5.10 CIE diagram for temperature dependent PL sample and ZnO prepared at various measuring temperature. 96

6.1 XRD patterns of the $Zn_{1-X}Cd_XO$ and undoped ZnO as-synthesized.102
6.2 XRD pattern (Variation of 2θ) vs C-axis lattice constant. 103
6.3 The variation in Crystallite size versus 2θ of FWHM (degree) . . . 103
6.4 SEM image of sample prepared ($Zn_{1-X}Cd_XO$, $0.15 \leq X \leq 0.45$), for X=0.15(A) and X=0.25(B) and corresponding point EDX C and D results 104
6.5 Transmittance spectra of $Zn_{1-X}Cd_XO$, $0.15 \leq X \leq 0.45$ and undoped ZnO. 105
6.6 Absorbance spectra of $Zn_{1-X}Cd_XO$ ($0.15 \leq X \leq 0.45$). 106
6.7 Band gap energy as a function of undoped ZnO and $Zn_{1-X}Cd_XO$, $0.15 \leq X \leq 0.45$ samples calculated using $((\alpha h\nu)^2)$ vs $(h\nu)$. The inset shows the band gap energy as a function of Cd concentration (X). 107
6.8 Room-temperature PL spectra of undoped ZnO and ($Zn_{1-X}Cd_XO$, $0.15 \leq X \leq 0.45$ 108
6.9 Gaussian deconvoluted room temperature PL spectra of powders with undoped ZnO(B), (X=0) and ($Zn_{1-X}Cd_XO$ for $X = 0.45$, as shown in A 109
6.10 FTIR spectra of undoped ZnO and ($Zn_{1-X}Cd_XO$, $0.15 \leq X \leq 0.45$) as-synthesized samples 110
6.11 CIE diagram of undoped ZnO and ($Zn_{1-X}Cd_XO$, $0.15 \leq X \leq 0.45$) samples. 111

7.1 A.XRD patterns of undoped and Al doped ZnO nanocrystalline powders for different Al concentrations B. ω_{scan} (rocking curve) for samples having Al concentration at x=0.15, x=0.20, x=0.25, x=0.30.116

7.2 SEM micrograph and EDX spectrum of ZnO nanoparticles at: (A)undoped ZnO. (B)$x = 0.1$. (C)$x = 0.15$ (D)$x = 0.20$ (E)$x = 0.30$ and F, G, H, I, J and K are the corresponding EDX spectras of $x = 0.0$, $x = 0.1$, $x = 0.15$, $x = 0.20$, $x = 0.25$ and $x = 0.3$, respectively. . . . 118

7.3 PL emission of ZnO nanoparticles synthesized at various temperatures. 119

7.4 A. EPR measurements for the undoped and Al doped ZnO . B. Shows the enlarged EPR measurements which is highlighted in between 250-400 mT 120

List of Tables

1.1 Some recently reported lines emitted from ZnO and the proposed associated deep level defect(s) causing the emission. The conduction and valence bands are abbreviated in the usual way as C.B. and V.B., respectively. 11

1.2 Measured and calculated lattice constants and the u parameter of ZnO [1, 12, 13, 30] 14

5.1 Measured properties of ZnO nanoparticles at various temperature . 86

7.1 The calculated lattice constants of Al doped and undoped ZnO . . 117

Declaration

I (Leta Tesfaye Jule) declare that the thesis hereby submitted by me for the Philosophiae Doctor degree at the University of the Free State is my own independent work and has not previously been submitted by me at another university/faculty. I furthermore, cede copyright of the thesis in favour of the University of the Free State.

Signature..... Date:.....

Keywords

- Core/Shell structure
- Arrays of Nanorods
- Sol-gel
- Chemical bath deposition
- ZnO nanomaterials
- ZnO/ZnS
- Photoluminescence
- Dielectric function
- Effective medium approximation
- Electron paramagnetic resonance
- Room temperature ferromagnetism
- Finite difference time domain
- X-ray diffraction
- Surface plasmon resonance

Abbreviations

- 1D - One dimensional
- A^oX - Neutral acceptor bound exciton
- C - Concentration of a point defect
- CA - Citric acid
- CBD - Chemical bath deposition
- CCPA - Coated coherent potential approximation
- DAP - Donor acceptor pair
- DDA - Discrete Dipole Approximation
- DF - Dielectric function
- DFT - Density functional theory
- DI - De-ionized water
- DLE - Deep Level emission
- D^oX - Neutral donor bound exciton
- EMA - Effective medium approximation
- EDS/EDX - Energy dispersive x-ray spectroscopy
- FDTD - Finite difference time domain
- FWHM - Full width at half maximum
- FTIR - Fourier transform infrared spectroscopy
- FX - Free excitons
- HCP - Hexagonal close packed

- HF - Hydrofluoric acid
- IR - Infrared
- E_{loc} - Local electric field
- MBE - Molecular Beam Epitaxy
- MG - Maxwell Garnett approximation
- MOCVD - Metal-organic chemical vapour deposition
- MOVPE - Metal organic vapour-phase epitaxy
- NBE - Near band edge emission
- EPR - Electron paramagnetic resonance
- PL - Photoluminescence
- RT - Room temperature
- SEM - Scanning electron microscope
- SPR - Surface plasmon resonance
- Si - Silicon
- TES - Two electron satellite
- UV - Ultraviolet
- VBM - Valance band maximum
- XRD - X-ray diffraction
- ZnO - Zinc oxide
- ZnS - Zinc sulphide

Abstract

There is currently widespread interest among researchers in ZnO-ZnS coreshell nanorods as electrodes in prototype solar cells. ZnS has been proposed as a suitable inorganic sensitizer to ZnO because ZnO and ZnS when in intimate contact, form a type-II (staggered) heterojunction with 1.00 eV valence band off-set. Type II core shell nanorods should therefore act to separate electrons and holes radially. This has been confirmed by density functional theory (DFT) calculations, which revealed an active separation of electron hole pairs after photo-excitation. Therefore these structures are similar to coaxial cables, because they allow the movement of the electrons through the core (i.e. ZnO) in one direction and the holes through the outer shell (i.e. ZnS) in the opposite direction.

In this thesis, rapid synthesis of ZnO and controllable growth of ZnO/ZnS core-shell structures has been realized. Moreover, the effect of dopants on the structural, optical, and its magnetic properties are investigated in detail. The final product was analyzed using such techniques as scanning electron microscopy (SEM), photoluminescence (PL) spectroscopy(steady and temperature dependent), Ultra-violet visible (UV-Vis) spectroscopy, Fourier transform infrared spectroscopy (FTIR), Electron paramagnetic resonance (EPR) and X-ray diffraction (XRD).

ZnO nanorod arrays were grown by a two-step chemical bath deposition process on (100) silicon substrates. ZnS coated ZnO nanorods were prepared by a simple, cost effective, two-step chemical synthesis process. This method provides a continuous, uniform ZnS coating on ZnO nanorods at relatively low temperature. The optical properties of the core-shell(ZnO/ZnS) are explored including the case when the absorption of propagating wave by dissipative component is completely compensated by amplification in active (lasing) medium.

Rapid synthesis of blue emitting ZnO nanoparticles for fluorescent applications has been developed. In this method ZnO nanoparticles (NPs), with size $16 - 20$ nm were produced using simple, cost effective and rapid synthesis method. In this method zinc salt (typically zinc acetate dehydrate) is directly annealed in air at a

temperature from $200-500\ ^0C$ for 2 h to form ZnO (NPs). This synthesis method would be ideal for blue light emitting applications as it is catalyst free growth and only requires zinc precursor to produce NPs that can emit visible emission by scalable temperature.

Cd doped ZnO nanopowder has been synthesized by facile sol-gel method. The modulation in optical band gap of the samples decreases from 3.15 eV to 2.76 eV are observed and it is believed to be responsible for the red shift in Ultra-violet visible (UV-Vis) spectroscopy with increase in Cd content. This is explained in terms of possibility of engineering band gap and influencing physical, chemical, and electronic properties which provides a strong impetus to study nanocrystals and other nanodimensional materials. The method employed would be ideal to synthesize materials for devices operating in the visible region as well as for developing heterojunction (Cd:ZnO) structures.

Defect-induced room temperature ferromagnetic properties of the Al-doped ZnO (AZO) and undoped ZnO nanostructure synthesized by sol-gel method has been investigated. Electron Paramagnetic Resonance (EPR) spectroscopy which is an effective tool to investigate the origin and nature of un-paired electrons in an atom shows the electron spin trapped in defected areas become randomly orientated at higher atomic percentages of Al. Based on PL and EPR analysis it was demonstrated that singly ionized oxygen vacancies, play a crucial role in mediating ferromagnetism in the undoped ZnO where as in Al doped ZnO it might be due to Al clustering forming Al-Al short range orders.

Acknowledgements

I express my profound sense of reverence to my promoter Prof F.B. Dejene, for the opportunity to work in his group, his constant guidance, support, motivation and untiring help during the course of my PhD. I have been amazingly fortunate to have a promoter who gave me a full freedom to explore on my own way and at the same time the guidance to recover when my steps faltered. I hope that one day I would become as good an advisor to my students as Prof has been to me. Thank you, Prof once again. My co-promoter, Dr. Kittessa Roro, has always been there to listen and give some brotherly advice. I am deeply grateful to him for the crucial discussions that helped me sort out the chemistry aspect of my work. I am also thankful to him for his brotherly and friendly approach all over the time.

It is my pleasure to acknowledge all my current and previous colleagues at UFS Physics department, specially Dr. Moges, Dr. Ali Wako, Dr. Abdub Ali, Dr. Tshabalala, Dr. L.F Koao, and my fellow researchers Nebiyu Debelo, Seithati Tebele, Lephoto Mantwa, Ungula Jatan, Winfred Mweni, Thembikosi Malevu, Meiki Lebeko, and to all the staff members of the Physics department for their enormous support and providing a good atmosphere in the department and lab. I will always be grateful to them for helping me to develop the scientific approach and attitude. Dr. Zelalem Urgessa from NMMU, I am very thankful for your encouragement, for numerous discussions on related topics that helped me improve my knowledge in the area and support during the entire course of my studies you are the man in need and indeed. Prof J.R. Botha are also owed my thanks and acknowledgments. It would not have been possible to carry out this research without the financial support from University of the Free State Research Directorate. Wolkite University, Ethiopia is also acknowledged for the study leave. Finally, and most importantly, I would like to thank my wife Lalise. Your support, encouragement, patience and unwavering love were undeniably and I owe you love and respect than I can say with this little space. I would like to thank my lovely daughter Milki for that wonderful smile and playful time that you were always able to create. I thank my parents, brothers and sisters, for their faith in me and allowing me to be as ambitious as I wanted. It was under their watchful eye that I gained so much drive and an ability to tackle challenges head on.

Chapter 1

Introduction

1.1 Nanostructured ZnO: Historical Overview

Zinc oxide (ZnO), a II-VI direct wide bandgap semiconductor, has been studied by the scientific community since the 1930s [1]. Although it has unique and interesting properties, such as a relatively high exciton binding energy (60 meV), and a wide bandgap (3.34 eV), and is piezoelectric, biologically safe and biocompatible [2], researchers work with ZnO has previously been focused on obtaining stable p-type dopants for ZnO. In addition to these excellent properties, ZnO possesses a large number of extrinsic and intrinsic deep-level impurities and complexes (clusters) that emit light of different colors, including violet, blue, green, yellow, orange and red, i.e., all constituents of white light [3, 4, 5]. Because of this, ZnO is considered to be attractive for applications requiring luminescent materials. ZnO, especially in its nanostructure form, is currently attracting intense global interest for photonic applications [2]. ZnO has the additional advantages of being easy to grow and possessing the richest known family of nanostructures [5]. The present global interest in ZnO nanostructures is motivated by the possibility of growing them on any p-type substrate and hence producing high quality pn heterojunctions. The interest in optoelectronic applications arises from the possibility of developing low energy and environmentally friendly white light emitting technologies and laser diodes that operate above room temperature [3]. The renewed interest in utilizing the excellent properties of ZnO in optoelectronic devices is mainly due to the ZnO ambipolar doping problem mentioned above. This problem frequently occurs in

wideband gap materials, in which it is very easy to dope the material with one polarity but is very difficult to dope the same material with the other polarity [6]. As ZnO is naturally n-type, it is very difficult to dope it with materials of p-type polarity. Several laboratories have reported p-type ZnO, but their results were difficult to reproduce in other laboratories and hence remain controversial. Elements from group I, including Li, Na, and K, as well as elements like Cu and Ag, are supposed to be good acceptors when replacing a Zn site, and they form deep acceptors with ionization energies around a few hundred meV above the valence band [7]. This implies that under normal conditions, i.e., at equilibrium, doping can be achieved without any ionization leading to free holes.

Moreover, at high levels of doping with such elements, interstitial Li (or Ag) atoms will act as donors and compensate many acceptors [8, 9]. Another possibility for doping ZnO to p-type is to use elements from group V on the O site, including N, P, Sb, and As. Nevertheless, most efforts to use these elements have led to poorly reproducible results. An elegant summary of all of these efforts is documented in Look et al. [10, 11]. Most recently, there have been successful reports of doping ZnO with N, forming a level with ionization energy of around 100 meV, less than the 160 meV ionization energy of the standard Mg acceptor in GaN [6]. Nevertheless, due to the existence of other native deep levels close to the conduction band, the compensation effect makes these efforts unsuccessful in producing stable and highly doped p-type ZnO materials. The difficulty in doping ZnO to p-type polarity has led researchers to seek to create heterojunctions with other p-type semiconductor materials to enable ZnO to be used in optoelectronic devices. These efforts began by growing n-type ZnO thin films on p-type substrates. However, due to lattice mismatches, most of these efforts have not led to the development of device-quality heterojunctions. The efforts in growing thin films of n-type ZnO on different p-type substrates, along with many of the fundamental properties of ZnO, are described in the comprehensive review written by Ozgur et al. [1].

Nanostructures, especially nanorods or nanowires, possess a relatively large surface area to volume ratio, enabling them to release stress and strain due to lattice mismatch with other materials. In addition, ZnO has been shown to be able to produce a rich family of different nanostructures; as a wurtzite structure, ZnO has a total of 13 different facet growth directions: (0001), $(01-10)$, $(2-1-10)$. Together with a pair of polar surfaces 0001, this uniquely structured material has been demonstrated to form a diverse group of nanostructures: nanorods, nanobelts, nanocombs, nanosprings, nanorings, nanobows, nanojunction arrays, and nanopropeller arrays, which are formed largely due to the highly ionic character of the polar surfaces [12]. Some ZnO nanostructures (namely tetrapods) were unintentionally synthesized as early as 1944 [13]. At that time, there were no microscopes with sufficient resolution to view the synthesized structures, which have since been identified as tetrapods.

The different growth methods used to obtain ZnO nanostructures can be divided into two main groups: low ($< 100\ ^0C$) and high (up to $1000\ ^0C$) temperature techniques. Willander et al. provide a thorough review of these different growth techniques [2]. High quality ZnO nanostructures have been grown on a variety of crystalline as well as amorphous (polymer) substrates and formed excellent pn heterojunctions, in contrast to thin films of ZnO, which have shown very limited success in forming heterojunctions. One advantage of n-ZnO nanorods on any p-substrate is that each nanorod will form a discrete, separated pn junction, and hence a large-area light emitting diode can be designed without compromising the junction area, which would lead to large reverse leakage currents. This is an important property that is advantageous for large-area lighting commercialization.

1.1.1 Luminescent centers and defect Chemistry in ZnO

Efficient donors and acceptors have energy levels near the conduction and valence bands, respectively; deep centers also exist with energy levels deep in the

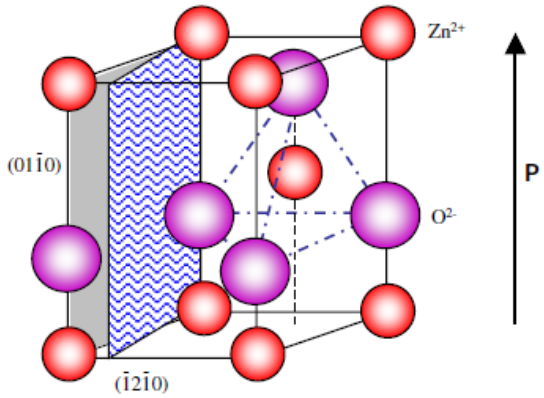

Figure 1.1: The wurtzite structure model of ZnO. The tetrahedral coordination of ZnO is shown [28].

forbidden gap. The room temperature photoluminescence (PL) spectrum of ZnO nanorods/nanowires with diameters larger than 20 nm is similar to the PL spectra of bulk ZnO. This room temperature PL spectrum is normally characterized by near-band-edge (NBE) ultra-violet (UV) emission and at least one broad band emission due to deep levels, called DLE. DLE refers to the broad band extending from just above 400 nm up to 750 nm, i.e., the whole visible spectrum. The broadness of the band results from the fact that it represents a superposition of many different deep levels emitting at the same time. Different reports have suggested different deep levels as the origin of the observed emissions. Before discussing the origin of the deep band emissions, it is important to discuss most of the known deep levels in ZnO and some of their important properties such as their formation energy and contribution to conductivity.

Although no consensus exists on the origin of the broad deep band emission, the broad nature of the emission suggests the possibility that it is a combination of many emissions. The deep levels of ZnO are divided into extrinsic and intrinsic deep levels. The possible intrinsic native deep levels in ZnO are oxygen vacancy (V_O), zinc vacancy (V_{Zn}), oxygen interstitial (O_i), zinc interstitial (Z_{ni}), oxygen anti-site (O_{Zn}), and zinc anti-site (ZnO). This is in addition to native defect clusters, which are usually formed by the combination of two point defects or one point defect and one extrinsic element, e.g., a $V_O Zn_i$ cluster formed by Z_{ni}

and V_O. This V_O Zn_i cluster is one of the clusters that has been previously identified and is situated 2.16 eV below the conduction band minimum. These native point defects often directly or indirectly control doping, compensation, minority carrier lifetime and luminescence efficiency in semiconductors [14]. Native defects are often invoked to explain the fact that ZnO always exhibits a high level of unintentional n-type conductivity. Even the difficulty in obtaining stable p-type doping is closely related to a compensation effect connected to intrinsic native defects that lie in the forbidden gap (deep centers). The concentration of a point defect depends on its formation energy. At thermodynamic equilibrium and in dilute cases (no defect-defect interaction), the concentration of a point defect (C) is given by [14].

$$C = N_{sites} exp(\frac{-E^f}{k_B T}), \tag{1.1.1}$$

where c is the point defect concentration, E^f is the formation energy, N_{sites} is the number of available sites to accommodate the defect, k_B is Boltzmanns constant, and T represents temperature. According to Eqs. (1.1.1) defects with high formation energies will occur at low concentrations. The formation energy E^f of point defects is not constant, but rather depends on the growth parameters and annealing conditions [15]. The formation energy of an oxygen vacancy depends on the abundance of oxygen and zinc atoms in the growth environment. Furthermore, if the vacancy is charged then the formation energy depends on the Fermi level (E_F), i.e., the electron chemical potential. The chemical potential depends on the growth conditions, which can either be oxygen-rich, zinc-rich or in between these two extremes. Hence, the chemical potential is usually treated as a variable and is chosen according to certain rules. In reality, the growth environment controls the concentration of native defects in ZnO. For further details on the limitations of chemical potential values, the reader is advised to Janotti et al. and van de Walle et al. [14, 15]. As discussed above, these deep levels introduce levels in the bandgap of the semiconductor that involve transitions between different charge states. The transition levels can be experimentally observed when the final charge

state fully relaxes to its equilibrium configuration after the transition, such as in deep level transient spectroscopy (DLTS) [16].

Conventionally, if the transition level is situated such that the defect is most likely to be ionized at room temperature or at the device operating temperature, then this is called a shallow transition level [14]. If the transition level is unlikely to be ionized at room temperature, then it is a deep transition level. The first step in the discussion on deep level native defects in ZnO is to consider V_O. V_O and Zn_i have long been suggested to be sources of the observed unintentional doping in ZnO, which is due to shallow levels situated $30 - 40$ meV below the conduction band minima [17, 18]. The assignment of V_O or Zn_i to the unintentional n-type doping originated from the fact that the growth of ZnO crystals was typically performed in a Zn-rich environment, and hence the dominant native defects were assumed to be V_O and Z_{ni}. Nevertheless, recent careful theoretical study revealed that this claim was incorrect for both V_O and Zn_i, as will be discussed below [14]. The formation energy of V_O was found to be quite high in n-ZnO material, even under extreme conditions, where it has a value of 3.27 eV. According to Eq. (1.1.1), V_O will always occur in low concentrations under equilibrium conditions, and it is not expected to be the source of the unintentional n-type doping. According to the energy calculations, isolated V_O cannot be the source of electrons in the conduction band in ZnO. In fact, in p-type doped ZnO, V_O assumes a 2^+ charge state and hence provides a potential source of compensation in p-type ZnO. This theoretical investigation [14] was consistent with experimental evidence from positron annihilation spectroscopy studies [19, 20], that studied grown and electron-irradiated ZnO samples. It has been shown experimentally that the dominant defect in electron-irradiated n-ZnO samples is V_{Zn}, with the Fermi level located 0.2 eV below the conduction band minima [14, 19, 20]. Neutral V_O was also detected in these experiments. These results imply that charged V_O, if present, will only be in low concentrations below the detection limit due to their

high formation energy as discussed above. Nevertheless, other experimental measurements have shown that native defects, and especially V_O deep level defects, can contribute to the unintentional n-type conductivity of ZnO when present as complexes, but not as isolated native point defects [21]. On the other hand, V_{Zn} has the lowest formation energy of all of the native defects in n-type ZnO, while its formation energy in p-type ZnO is quite high [14]. This energy is low enough for V_{Zn}^{2-} to occur in modestly doped ZnO and to act as a compensating center. Zinc vacancies usually introduce partially occupied states in the bandgap. These states are derived from the broken bonds of the oxygen as nearest four neighbors and lie close to the valence band minima. These states are partially filled and can accommodate an electron, causing V_{Zn} to act as an acceptor. However, quantitative calculations showed that V_{Zn} levels are deep acceptors. On the other hand, zinc vacancies are not believed to contribute to the p-type doping of ZnO due to the high formation energy of V_{Zn} in p-type ZnO [14].

V_{Zn} has been observed in many as-grown n-ZnO materials and are more favorable when growth is performed in oxygen-rich conditions [14, 19]. Zinc vacancies are situated 0.9 eV above the valence band minima, and hence a transition from the conduction band (or from a shallow donor) would yield a luminescence around 2.4 eV. This corresponds to the green luminescence observed in ZnO samples grown by many techniques, appearing at $2.4 - 2.5$ eV. Hence, V_{Zn} is widely accepted to contribute to the broad band emission at this green wavelength, although V_O was also suggested as early as 1954 [22] to be the source of this green emission (see discussion below). On the other hand, for n-type ZnO, i.e., for a Fermi level close to the conduction band, interstitial zinc has high formation energy even under Zn-rich conditions, with a formation energy that reaches 6 eV. This implies that under equilibrium conditions, Zn_i will be present in low concentrations and cannot contribute to the unintentional doping of ZnO. Moreover, the formation energy of Zn_i^{2+} decreases rapidly as the Fermi level decreases toward the valence band minima. This implies that Zn_i is a potential source of compensation in p-type ZnO

[14]. The excess of oxygen in the ZnO lattice can be accommodated through the existence of oxygen interstitials, which can exist in electrically active or inactive forms. Electrically active O_i occupies an octahedral site [14] and introduces states that can accept two electrons in the lower part of the ZnO bandgap. The result is a deep acceptor transition with states situated 0.72 eV and 1.59 eV above the valence band minima. The other form of O_i is an electrically inactive configuration, which has quite high formation energies for both forms of O_i, except under extremely O-rich environments. This implies that O_i is not expected to be present in high concentrations under equilibrium conditions. The remaining native defects are anti-sites. Zinc anti-sites or oxygen anti-sites consist of zinc or oxygen atoms sitting at the wrong lattice position.

All calculations have agreed that ZnO forms shallow donors [23, 24]. The final native defect is oxygen occupying an anti-site. Oxygen anti-sites can be created under non-equilibrium conditions, for example by irradiation or ion implantation [14, 25]. Recent calculations indicated that O_{Zn} is a deep acceptor level with two possible transitions situated 1.52 eV and 1.77 eV above the valence band minima. All of the native defects discussed above can exist in different charged states or in a neutral state, and the formation of complexes between native defects and other extrinsic species in ZnO has also been reported. As mentioned above, most of these native defects introduce deep levels at different positions in the bandgap, and hence a rather large number of luminescence lines with different energies can be observed. This explains why all of the visible colors have been experimentally observed in different ZnO samples. The main known extrinsic deep-level defects in ZnO are Li, Cu, Fe, Mn, and OH, each of which have been reported to emit at different wavelengths as discussed in more detail by Ozgur and Klingshirn et al. [1, 6]. Different deep levels can produce different lines of the same color; one example of this is ZnO:Cu and ZnO:Co, which emit different green colors [6]. This phenomenon is an additional source of the discrepancy in explaining the observed emission of ZnO. Finally, hydrogen also plays an important role in the properties

of the native defects. Hydrogen is not a deep level in ZnO, but we mention it due to its important role as a donor. Unlike other semiconductors where hydrogen can be positive or negative, hydrogen in ZnO is always positive (H^+), i.e., it acts as a donor and possesses low ionization energy [22]. As mentioned above, the origin of the deep level emission (DLE) band has been controversial for decades. Below, we will briefly discuss some of the different opinions about the origin of the DLE based on different findings. The common bands observed in ZnO are green luminescence, yellow luminescence, and red luminescence DLE bands [11]. The green luminescence band, which appears at energies of $2.4 - 2.5$ eV, is the most thoroughly investigated DLE band in ZnO and has been the subject of the most debate. Several studies have been published regarding the origin of this band, and they have used different experimental setups and different samples grown under various conditions. The green luminescence has been observed in samples grown by a variety of techniques.

There may be multiple sources of this luminescence because different transitions can lead to quite similar luminescent emission wavelengths. Zinc vacancies, one of the most probable native defects in ZnO, have been suggested by many authors to be the single source of this emission; see [26, 27, 28]. Oxygen vacancies have also been suggested by many authors [29, 30, 31]. In addition, zinc interstitials, oxygen interstitials, and other extrinsic deep levels including Cu have all been proposed as sources of the green luminescence emission in ZnO. More recently, the green emission band has been explained as originating from more than one deep level defect. In this recent investigation, V_O and V_{Zn}, which have different optical characteristics, were both found to contribute to the broad green luminescence band [32, 33, 34]. The yellow emission band that appears at 2.2 eV was first observed in a Li-doped ZnO layer [9, 35]. Li is located 0.8 eV above the valence band and constitutes a deep acceptor level in ZnO. Yellow emission has also been attributed to native deep level defects in ZnO, namely to oxygen interstitials [36, 37]. The yellow emission band was also observed with metastable

behavior in undoped bulk ZnO [11]. Under irradiation by a He-Cd laser, the green luminescence band mentioned above was gradually bleached, and yellow emission emerged and saturated with an excitation density of 10-3 W/cm2, implying that the associated deep level is present at a low density. The yellow emission band was recently observed in ZnO nanorods grown by low temperature (90) ^0C chemical growth in different laboratories [38]. The origin of this band in these low-temperature grown samples was attributed to O_i or the presence of Li impurities in the initial growth material. A $Zn(OH)_2$ group attached to the surface of ZnO nanorods grown by chemical methods has also been proposed as a possible source of the yellow deep-level defect emission band in these samples [39]. Yellow emission has been observed in many different grown ZnO nanorods, and it was demonstrated that the emission can be replaced by the green and red bands upon post-growth annealing [39]. This was explained by the fact that upon proper post-growth annealing, the hydroxyl group can desorbs and hence modify the emission from that of the as-grown ZnO nanorods [39]. Orange, orange-red and red emission bands have also been observed in ZnO [39]. The orange emission, which is not very common in ZnO, was proposed to be due to transitions related to oxygen interstitials [40], the orange-red emission was recently attributed to transitions associated with zinc vacancy complexes [41], and the red emission was proposed to be due to transitions associated with zinc interstitials [42]. The summary of recent studies are given by Table 1.1.

From the preceding discussion on the properties of the commonly reported deep level centers in ZnO and their associated possible transitions, it is clear that ZnO can emit luminescence over the entire visible region. Although no consensus has been reached regarding the origin of the different observed colors, partly due to the different defect configurations in different samples [51, 52, 53], ZnO provides the potential for creating white light emitting diodes, especially considering the recent progress in the growth and reproducibility of ZnO nanostructures grown on a variety of other p-type substrates [2]. The development of low temperature

Table 1.1: Some recently reported lines emitted from ZnO and the proposed associated deep level defect(s) causing the emission. The conduction and valence bands are abbreviated in the usual way as C.B. and V.B., respectively.

Emission color (nm)	Proposed deep level transition
Violet	Zn_i to V.B. [43]
Blue	Zn_i to V_{Zn} or C.B. to V_{Zn} [43, 44, 45]
Green	C.B. to V_O, or to V_{Zn}, or C.B. to both V_O and V_{Zn} [46, 47]
Yellow	C.B. to Li, or C.B. to O_i [48]
Orange	C.B. to O_i or Zn_i to O_i [43, 49]
Red	Lattice disorder along the c-axis (i.e. due to Zn_i) [50]

chemical growth approaches as suitable techniques for large area synthesis of ZnO nanorods with excellent luminescence properties on any substrate opens up new possibilities for developing hybrid ZnO pn junctions. One of these hybrid junctions is a combination of ZnO nanorods and p-type semiconducting polymers.

1.1.2 Crystal structures of ZnO

ZnO is a II-VI compound semiconductor whose ionicity resides at the borderline between covalent and ionic semiconductor. The crystal structures shared by ZnO are wurtzite, zinc blende, and rocksalt [1, 54]. At ambient conditions, the thermodynamically stable phase is wurtzite. The zinc-blende ZnO structure can be stabilized only by growth on cubic substrates, and the rocksalt (NaCl) structure may be obtained at relatively high pressures. Wurtzite zinc oxide has a hexagonal structure (space group C6mc) with lattice parameters $a = 0.3296$ and $c = 0.52065$ nm. The structure of ZnO can be simply described as a number of alternating

planes composed of tetrahedrally coordinated O^{2-} and Zn^{2+} ions, stacked alternately along the c-axis (figure 1). The tetrahedral coordination in ZnO results in noncentral symmetric structure and consequently piezoelectricity and pyroelectricity. Another important characteristic of ZnO is polar surfaces. The most common polar surface is the basal plane. The oppositely charged ions produce positively charged $Zn-(0001)$ and negatively charged $O-(000\bar{1})$ surfaces, resulting in a normal dipole moment and spontaneous polarization along the c-axis as well as a divergence in surface energy. To maintain a stable structure, the polar surfaces generally have facets or exhibit massive surface reconstructions, but $ZnO-\pm(0001)$ are exceptions: they are atomically flat, stable and without reconstruction [1, 2]. Efforts to understand the superior stability of the $ZnO-\pm(0001)$ polar surfaces are at the forefront of research in todays surface physics [3, 4]. The other two most commonly observed facets for ZnO are $2\bar{1}\bar{1}0$ and $40\bar{1}\bar{1}0$, which are non-polar surfaces and have lower energy than the 0001 facets

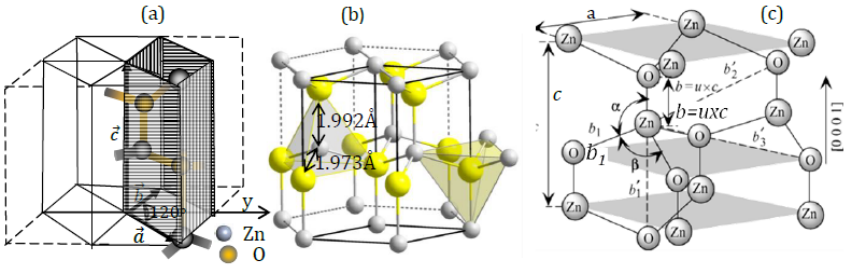

Figure 1.2: Schematic representations of wurtzite ZnO: (a) the primitive unit cell, (b) neighbouring atoms showing tetrahedral coordination where every atom of one kind is surrounded by four atoms of the other kind, and (c) the detailed structure of the wurtzitelattice. Second-nearest-neighbour distances, u, and bond angles $\alpha$and $\beta = 109.47^0$, are also shown [24, 55].

1.1.3 Lattice Parameters

Lattice parameters of ZnO have been investigated over many decades [28, 56, 57]. The lattice parameters of a semiconductor usually depend on the following factors: (i) free electron concentration acting via deformation potential of a conduction band minimumoccupied by these electrons, (ii) concentration of foreign

atoms and defects and their difference of ionic radii with respect to the substituted matrix ion, (iii) external strains (e.g., those induced by substrate), and (iv) temperature. The lattice parameters of any crystalline material are commonly and most accurately measured by highresolution X-ray diffraction (HRXRD) using the Bond method [31] for a set of symmetrical and asymmetrical reflections. Table 1.2 tabulates measured and calculated lattice parameters, c/a ratio, and u parameter reported by several groups for ZnO crystallized in wurtzite, zinc blende, and rocksalt structures for comparison. The room-temperature lattice constants determined by various experimental measurements and theoretical calculations for the wurtzite ZnO are in good agreement with each other. The lattice constants mostly range from 3.2475 $\dot{A}$ to 3.2501 $\dot{A}$ for the a-parameter and from 5.2042 to 5.2075 $\dot{A}$ for the c-parameter. The data produced in earlier investigations, reviewed by Reeber [30], are also consistent with the values given in Table 1.2. The c/a ratio and u parameter vary in a slightly wider range, from 1.593 to 1.6035 and 0.383 to 0.3856, respectively. The deviation from that of the ideal wurtzite crystal is probably due to lattice stability and ionicity. It has been reported that free charge is the dominant factor responsible for expanding the lattice proportional to the deformation potential of the conduction band minimum and inversely proportional to the carrier density and bulk modulus. The point defects such as zinc antisites, oxygen vacancies, and extended defects, such as threading dislocations, also increase the lattice constant, albeit to a lesser extent in the heteroepitaxial layers. For the zinc blende polytype of ZnO, the calculated lattice constants based on modern ab-initio technique are predicted to be 4.60 and 4.619 $\dot{A}$. Zinc blende ZnO films have been grown by using ZnS buffer layers [6]. The lattice constant was estimated to be 4.463, 4.37, and 4.47 $\dot{A}$ by using the spacing of RHEED pattern, albeit spotty, comparing the XRD peak position, and examining the transmission electron microscopy (TEM) images, respectively. These values are far from wurtzite phase indicating the formation of zinc blende ZnO. The lattice constant measured with the RHEED technique is in very good agreement with the theoretical predictions.

Table 1.2: Measured and calculated lattice constants and the u parameter of ZnO [1, 12, 13, 30]

a (Ang.)	c (Ang.)	c/a	u
3.2496	5.2042	1.6018	0.3819
3.2501	5.2071	1.6021	0.3817
3.2860	5.241	1.595	0.383
3.2498	5.2066	1.6021	0.383

1.2 Electronic band structure

Considering that ZnO is a candidate semiconductor for optoelectronic device applications, a clear understanding of the band structure is of critical importance in explaining the optical and electrical properties. As described earlier, ZnO lacks stable and reproducible p-type doping. As a result, other p-type materials have to be combined with ZnO in the same structure for device applications.

Several theoretical approaches of varying degrees of complexity, involving the Local Density Approximation (LDA), the Self-interaction corrected Pseudo Potential (Sic-PP) method, or the empirical tightbinding Hamiltonian, have been employed to calculate the band structure [58]. Experimental data have also been published regarding the band structure and electronic states of wurtzite ZnO [59]. UV reflection/absorption or emission techniques have been used to measure the electronic core levels in solids. These methods measure the energy difference between the upper valence-band states and the bottom conduction-band states. In ZnO, the valence band consists of three bands labelled A, B and C, by spin-orbit and crystal-field splitting [19]. This splitting is schematically illustrated in Fig. 1.3. The A and C sub-bands are known to possess Γ7 symmetry, while the B band has Γ9 symmetry. These three bands correspond to light holes (A), heavy holes (B) and the crystal field split band (C)[19]. The band splitting values are measured at 4.2 K [19].

The conduction band of wurtzite ZnO is constructed from s-like states and it

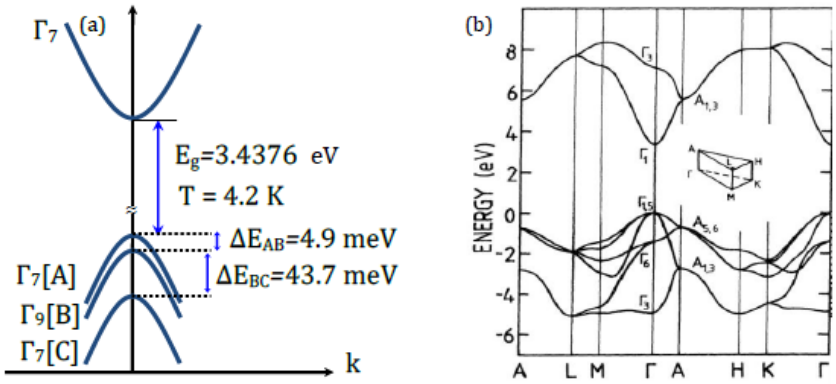

Figure 1.3: Low temperature band structure of ZnO showing valence band splitting into three (A, B, C) which is caused by crystal field and spin-orbit splitting [19] (a), and band structure of ZnO calculated using an empirical tight binding Hamiltonian (b). The zero energy in these graphs is taken as the upper edge of the valence band (after [55]).

is symmetrical about the Γ point, while the valence band is constructed mainly from p-like states. The band structure E(k) for ZnO, calculated by Ivanovet al.[52] using an empirical tight binding Hamiltonian, is given along the symmetry lines in the Brillouin zone in Fig. 1.3(b). The optical band gap between occupied and empty bands (i.e. between Γ1.5 and Γ1) in ZnO is about 3.37 eV. This energy represents the energy difference between full and empty states. The top filled states are called the valence band and the maximum energy of the valence band of states is called the VBM. The lowest band of empty states above the gap is called the conduction band with the lowest point in that band called the CBM. In this figure, the VBM and CBM coincide at $k = 0$, the Γ point, indicating that ZnO is a direct band gap semiconductor. In Fig. 1.3(b), six valence bands can be seen between 6 eV and 0 eV. According to Ivanovet al.[52] these are derived from the $2p$ orbitals of oxygen. For the conduction band there are two bands visible (above $\sim$ 3 eV). These states are strongly localized on the Zn and correspond to unoccupied Zn $3s$ levels.

1.3 Basic Properties of ZnO nanostructures

It is worth noting that as the dimension of the semiconductor materials continuously shrinks down to nanometer or even smaller scale, some of their physical properties undergo changes known as the "quantum size effects". For example, quantum confinement increases the band gap energy of quasi-one-dimensional (Q1D) ZnO, which has been confirmed by photoluminescence. Bandgap of ZnO nanoparticles also demonstrates such size dependence. X-ray absorption spectroscopy and scanning photoelectron microscopy reveal the enhancement of surface states with the downsizing of ZnO nanorods. In addition, the carrier concentration in 1D systems can be significantly affected by the surface states, as suggested from nanowire chemical sensing studies. Understanding the fundamental physical properties is crucial to the rational design of functional devices. Investigation of the properties of individual ZnO nanostructures is essential for developing their potential as the building blocks for future nanoscale devices. Even though research focusing on ZnO goes back many decades, the renewed interest is fueled by availability of high-quality substrates, precursor and dopants to produce p-type conduction and ferromagnetic behavior when doped with transitions metals, both of which remain controversial. There are still significant challenges that have to be overcome in order to produce efficient ZnO devices. These include:

- (i) Understanding the residual n-type conductivity in unintentionally doped ZnO.
- (ii) The achievement of stable and repeatable p-type conductivity.
- (iii) Controlling native defects and possible compensation processes.

Another main obstacle for the commercialization of ZnO based homojunction devices is the absence of stable and reproducible p-type doping with high hole concentrations and large carrier mobility. The major problems associated with this are the low solubility of most acceptor-type dopants, difficulties of substituting on

the host atom sites, the relative deepness of the acceptor states and the spontaneous formation of compensating donor-like defects. As a consequence, p-doping of ZnO is still an unsolved problem. Nonetheless, the unique properties of ZnO ensure continued worldwide research to explore and control its properties. Apart from the difficulty in achieving p-type conductivity for all types of ZnO materials (bulk, thin film and nanostructures), the reproducible growth of nanostructures is another issue which has attracted considerable attention. It is widely acknowledged that the morphology of ZnO nanostructures is highly sensitive to the growth environment (i.e temperature, pressure, substrates, precursors and their concentrations, the VI/II ratio or pH, etc). This sensitivity makes it very difficult to control the growth process for the reproducible formation of a desired morphology over large areas.

1.4 Motivation

Obtaining controllable, reliable, reproducible and high conductive p-type doping in ZnO has proved to be very difficult task, due to the low formation energies for intrinsic donor defects such as zinc interstitials (Zn_i) and oxygen vacancies (V_O) which can compensate the accepters. The efficiency of light emitting diodes can be limited by the low carrier concentration and mobility of holes suggesting that the excellent properties of ZnO might be best utilized by constructing heterojunctions with other semiconductors. The growth of n-type ZnO on other p-type materials could provide an alternative way to realize ZnO based p-n heterojunctions. In this way, the most significant impediment to the widespread exploitation of ZnO-related materials in electronic and photonic applications is the difficulty in carrier doping, particularly as it relates to achieving p-type material. ZnO n-type conductivity is relatively easy to realized via excess Zn or with Al, Ga, or In doping. With respect to p-type doping, ZnO displays significant resistance to the formation of shallow acceptor levels. Difficulty in achieving bipolor (n- and p-type) doping in a wide bandgap material is not unusual. In addition, there

have been several explanations put forward in explaining doping difficulties in wide bandgap semiconductors. First, there can be compensation by native point defects or dopant atoms that locate on interstitial sites. The defect compensates for the substitutional impurity level through the formation of a deep level trap. In some cases, strong lattice relaxations can drive the dopant energy level deeper within the gap. In other systems, one may simply have a low solubility for the chosen dopant limiting the accessible extrinsic carrier density. The emphasis of the present very active period of ZnO research includes the material for electronic circuits that is transparent in the visible and/or usable at elevated temperatures, a diluted or ferromagnetic material, when doped with Co, Mn, Fe, V, etc., for semiconductor spintronics, a transparent, highly conducting oxide (TCO), when doped with Al, Ga, In, etc., as a cheaper alternative to ITO. For several of the above-mentioned applications a stable, high, and reproducible p-doping is obligatory. Though progress has been made in this crucial field, as will be outlined below, this aspect still forms a major problem.

1.5 Definition of the Research Problem

The optical properties of a semiconductor are dependent on both the intrinsic and the extrinsic defects in the crystal structure. The investigations of the optical and structural properties of ZnO has a long history that started in the 1960s. The optical properties of ZnO, bulk and nanostructures have been investigated extensively by luminescence techniques at low and room temperatures. The photoluminescence (PL) spectra of ZnO shows ultra-violet (UV) emission band and a broad emission band as discussed by various authors so far [1]. The UV emission band is commonly attributed to transition recombinations of free excitons in the near band-edge of ZnO. The broad emission band in the visible region (420 nm - 750 nm) is attributed to deep level defects in ZnO. There are many different deep level defects in the crystal structure of ZnO and they affect the optical and electrical properties of ZnO. The luminescence defects and their possible transitions

in ZnO indicate that ZnO has a potential to emit excellent luminescence covering the whole visible region and it has the potential to be used in the fabrication and development of white light emitting diodes. It is also very crucial to understand the electrical and magnetic properties of ZnO for applications in nanoelectronics. The electrical behavior of undoped ZnO nanostructures is n-type and it is widely believed that it is due to native defects such as oxygen vacancies and zinc interstitials. The electron mobility in undoped ZnO nanostructures is not constant and it depends on growth method and doping concentration which is approximately $120 - 440\ cm^2\ V^{-1}s^{-1}$ at room temperature. In the following, we emphasis on the synthesis of ZnO nanostructures in addition to doping with various dopant to study the ferromagnetic, structural and optical properties of ZnO nanoparticles which has been investigated both theoretically and experimentally.

1.6 Objectives of the Research

The objective of the research is to:

- Investigate on the optical absorption enhancement of ZnO/ZnS core-shell nanorods embedded in active host medium both theoretically and experimentally.
- To synthesize ZnO nanoparticles using rapid and cost effective method which can be used for both fundamental and practical applications.
- Study the effect of Cd dopant on optical, structural and luminescence properties of ZnO, in particular the effect of concentration on band gap engineering and phase segregation of the alloy of ZnO.
- Investigate on the origin of room temperature ferromagnetic properties of ZnO by doping with various concentration of Al.

1.7 Outline of the Thesis

The thesis consists of eight chapters:

- Chapter 1: Deals with the general overview of the thesis. It includes the basic properties of ZnO, luminescence and fundamentals, the general objectives of the study.

- Chapter 2: Deals with the theoretical models used in the study for numerical calculations in particular: the electromagnetic wave interaction with metal/dielecric core-shell will be explained; two different models for describing metals will be discussed: the Lorentz model and the Drude model. Both models approximately describe the optical properties of metallic structures and the plasmonic properties that arise when the structures have dimensions on the order of nanometers. The models which are combined with numerical simulation used to calculate the optical absorption in the case of ZnO/ZnS core-shell structure are systematical related with the experimental section of the study, the details of the models are discussed under this chapter.

- Chapter 3: A detailed description of the experimental methods and procedures used in growing the nanostructures by chemical bath deposition (CBD) and sol-gel techniques are explained in this chapter. Luminescence in ZnO, methodology and the characterization tools are discussed under this section.

- Chapter 4: Presents the theoretically and experimental study on the interaction of radiation field phenomena interacting with arrays of nanowire/nanorod coreshell embedded in active host matrices. The experiment done on ZnS(shell)-coated by sulphidation process on ZnO(shell) nanorod arrays grown on (100) silicon substrate by chemical bath deposition (CBD) has been used for theoretical comparison. On the basis of more elaborated modeling approach and extended effective medium theory, the effective polarizability, the resonant conditions and the refractive index of electromagnetic mode dispersion of the coreshell nanowire arrays are derived under this chapter.

- Chapter 5: Under this section a systematic study on rapid synthesis of

blue emitting ZnO nanoparticles for fluorescent applications has been reported. In particular, the influence of growth temperature, temperature dependent photoluminescence study on the structural and optical properties of ZnO nanostructures is described under this chapter. The method developed demonstrates about ZnO nanoparticles (NPs), produced using simple, cost effective and rapid synthesis method. This synthesis method, only requires zinc precursor to produce NPs that can emit visible emission without external doping, the detail of the study are discussed.

- Chapter 6: Devoted to the discussion on wide visible emission and narrowing band gap in Cd-doped ZnO nanopowders synthesized via sol-gel route. In addition the effect of Cd dopant on structural and optical properties are discussed under this chapter.

- Chapter 7: Discusses about defect-induced room temperature ferromagnetic properties of the Al-doped and undoped ZnO nanostructures. The effects of the Al concentration on structural, optical and magnetic properties of the AZO ($Zn_{1-X}Al_XO$, $0.1 \leq X \leq 0.30$) are also presented in this chapter.

- Chapter 8: Finally, a summary of the results obtained in this work and a proposed direction for future work is presented.

Chapter 2

Theoretical Models and the optical response of metal/dielectric composites with electromagnetic wave interactions

2.1 Introduction

Interaction of light with nanocomposites reveals novel optical phenomena indicating unrivalled optical properties of these materials. The linear and nonlinear optical response of metal nanoparticles is specified by oscillations of the surface electrons in the Coulomb potential formed by the positively charged ionic core. This type of excitation is called the Surface Plasmon (SP). In 1908 Mie proposed a solution of Maxwells equations for spherical particles interacting with plane electromagnetic waves, which explains the origin of surface plasmon resonance (SPR) in the extinction spectra and colouration of metal colloids. During the last century optical properties of nanoparticles have extensively been studied and metal-dielectric nanocomposites have found various applications in different fields of science and technology [60, 61, 62]. Since the optical properties of metal nanoparticles are governed by SPR, they are strongly dependent on the nanoparticles size, shape, concentration and spatial distribution as well as on the properties of the surrounding matrix. Control over these parameters enables such metal-dielectric nanocomposites to become promising media for development of novel non-linear materials, nanodevices and optical elements [63, 64, 65].

An electromagnetic wave propagating through different media is affected by interactions with each medium as it traverses across the boundary between one medium and another. The two main interactions between incident light and a discrete particle are absorption and scattering. Scattering can be inelastic, where the wavelength of the scattered radiation is different from the incident wavelength, or elastic, where the scattered radiation has the same wavelength as the incident light. Examples of elastic scattering are Rayleigh scattering from small, dielectric (nonabsorbing) spherical particles and Mie scattering from spherical particles with no limitations on size or dielectric properties [66, 67, 68, 69, 70, 71, 72]. The discussion on electromagnetic waves has been limited to the propagation of waves and interactions with simple structures composed of arbitrary media. In the following section, two different models for describing metals will be discussed: the Lorentz model and the Drude model. Both models approximately describe the optical properties of metallic structures and the plasmonic properties that arise when the structures have dimensions on the order of nanometers. Specifically, the manifestation of surface plasmons in bulk metals, discrete particles, and metal/dielectric will be discussed. The section will conclude with a brief description of different models and theories of light scattering and absorption [73, 74, 75, 76, 77, 78].

2.2 Models describing metals and dielectrics

2.2.1 Lorentz Model

A plasma model is used to describe the optical properties of metals due to the free electron movement of the conduction electrons through a fixed positive, ionic background. The model was developed by H. A. Lorentz as a classical approach to describe optical properties of materials by assuming that electrons and ions of a medium are simple harmonic oscillators and neglecting material properties such as the lattice potential and electron-electron interactions. The simple oscillator model is of great use in determining optical properties of a material because it can describe a variety of optical excitations [79, 80, 81, 82, 83]. The microscopic model

of a polarizable material becomes a macroscopic system of independent, isotropic, and identical harmonic oscillators which are subjected to an applied electric field, E, which acts as a driving force. The oscillation response to an applied local electric field, E_{local}, for an electron with an effective mass, m, and a charge, e, is given by

$$m\frac{d^2x}{dt^2} + m\gamma\frac{dx}{dt} + Kx = eE_{loc}, \tag{2.2.1}$$

where x is the distance displaced from equilibrium, Kx is the restoring force for an electron with a spring constant, K. The oscillation of electrons is damped as a result of collisions, which adds a damping term to the equation, $m\gamma$, where the collision frequency, $\gamma = \frac{1}{\tau}$, and τ is the relaxation time for a free electron plasma which at room temperature is typically on the order of 10^{-14} making $\tau = 100THz$. Since the electric field has a harmonic time dependence [84],

$$E(t) = E_0e^{-i\omega t}, \tag{2.2.2}$$

with a frequency, ω, and time, t, the solution to the equation for an electron becomes

$$x(t) = x_0e^{-i\omega t}, \tag{2.2.3}$$

where phase shifts between the driving force of the electric field and the electron response is contained in the complex amplitude, x_0 [85]. The oscillatory solution to Eq. 2.2.1 becomes:

$$x(t) = E(t)\frac{e}{m(\omega_0^2 - \omega^2 - i\gamma\omega)}, \tag{2.2.4}$$

with $\omega_0^2 = \frac{K}{m}$. A schematic of a Lorentz harmonic is shown in Fig. 2.1.

In most systems, there is a certain degree of collisions that occur which means $\gamma \neq 0$ and the phase of the driving field and oscillating electrons have a displacement, D,

$$D = Ae^{(i\theta)}(\frac{eE}{m}), \tag{2.2.5}$$

with phase angle, θ ,

$$\theta = \tan^{-1}[\frac{\omega\gamma}{\omega_0^2 - \omega^2}], \tag{2.2.6}$$

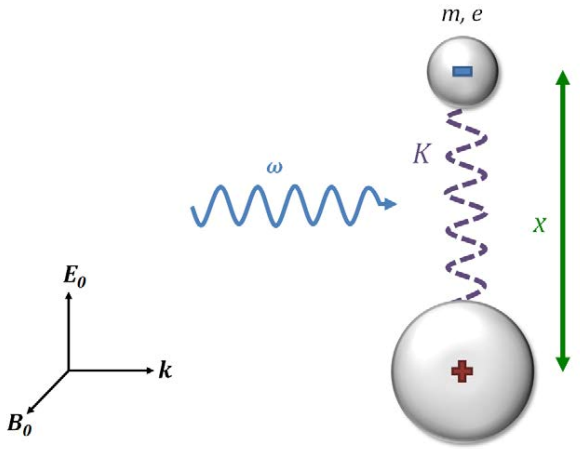

Figure 2.1: Lorentz harmonic oscillator [86].

and amplitude, A,

$$A = \tan^{-1}[\frac{1}{[(\omega_0^2 - \omega^2)^2 + \omega^2\gamma^2]^{\frac{1}{2}}}], \tag{2.2.7}$$

The consequence of the phase difference results in the maximum amplitude occurring when the frequencies $\omega_0 \cong \omega$. If $\gamma \ll \omega_0$, the height of the maximum amplitude is inversely proportional to γ and the full width at half maximum (FWHM) is proportional to γ. Fig. 2.2 shows a plot for the amplitude and phase relation for a hypothetical oscillator. At low frequencies, the oscillator response is in phase with the driving force where $\theta \cong 0$and $\omega \ll \omega_0$ as shown in Fig.2.2 (a). At the resonance frequency, the amplitude is at a maximum and the phase lag is $\theta = 90^0$. Near ω_0 a 180^0 phase change occurs. As a result, at high frequencies, $\omega \gg \omega_0$ the oscillator response and the driving force are 180^0out of phase. For

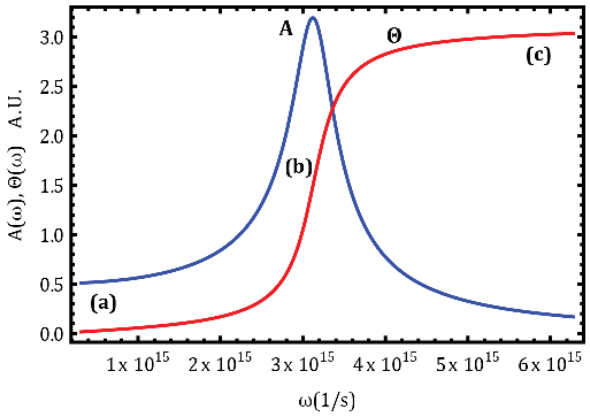

Figure 2.2: Hypothetical oscillator response to a driving force at (a) low frequencies, (b) resonance frequency, ω_0, and (c) high frequencies [86].

a single oscillator, the induced dipole moment is $p = ex$. For a large number of oscillators, n, the dipole moment per unit volume becomes,

$$P = -nex, \tag{2.2.8}$$

and when combined with Eq.2.2.4 becomes

$$P = \frac{\omega_p^2}{\omega_0^2 - \omega^2 - i\omega\gamma} E\varepsilon_0, \tag{2.2.9}$$

where the plasma frequency, is given by

$$\omega_p^2 = \frac{ne^2}{\varepsilon_0 m}, \tag{2.2.10}$$

The optical constants for the collection of oscillators can then be derived out, where the dielectric function for the bulk material is given by

$$\varepsilon(\omega) = 1 + \chi = 1 + \frac{\omega_p^2}{\omega_0^2 - \omega^2 - i\omega\gamma}, \tag{2.2.11}$$

which can be decomposed into the real, ε_1, and imaginary, ε_2, components of the complex dielectric function, $\varepsilon(\omega) = \varepsilon_1(\omega) + i\varepsilon_2(\omega)$ as

$$\varepsilon_1(\omega) = 1 + \chi' = 1 + \frac{\omega_p^2(\omega_0^2 - \omega^2)}{(\omega_0^2 - \omega^2)^2 + \omega^2\gamma^2}, \tag{2.2.12}$$

$$\varepsilon_2(\omega) = \chi'' = \frac{\omega_p^2\omega\gamma}{(\omega_0^2 - \omega^2)^2 + \omega^2\gamma^2}, \tag{2.2.13}$$

At the plasma frequency, ω_0, the imaginary part of the dielectric constant is at a maximum as shown in Fig. 2.3 for silver

2.2.2 Drude Model

In metals, the conduction and valence band overlap allowing for electrons near the Fermi level to be excited to different energy and momentum states by the absorption of photons with very little energy [87, 88, 89]. These intraband transitions give rise to free electrons which can be taken into account by modification of the Lorentz model. When the spring constant in Eq.2.2.1 is set to zero, it essentially clips the springs of the harmonic oscillators with K = 0 and $\omega_0 = 0$ to transform Eq.2.2.4 into

$$x(t) = E(t)\frac{e}{m(\omega^2 + i\gamma\omega)}, \tag{2.2.14}$$

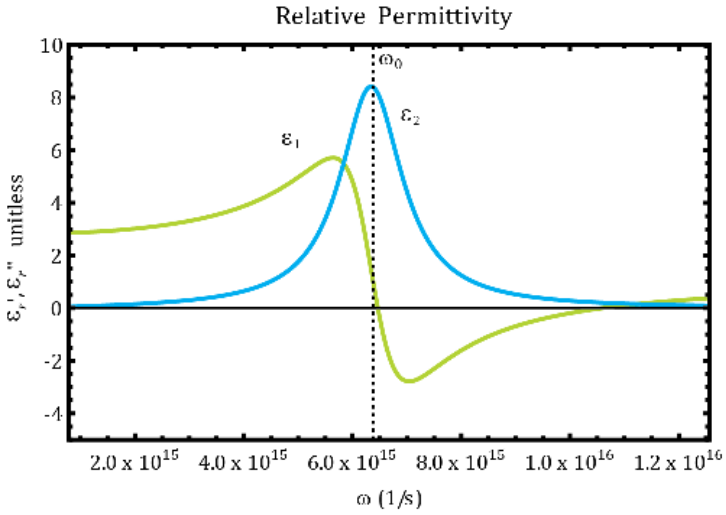

Figure 2.3: Frequency dependence of the real and imaginary parts of the dielectric constant of silver.

When the polarization in Eq.2.2.8 is combined with equation Eq.2.2.14, it becomes

$$P = -n\frac{e^2}{m(\omega^2 + i\gamma\omega)}E, \tag{2.2.15}$$

gives the relation between D and E in terms of frequency and electric permittivity as

$$D = \varepsilon_0(1 - \frac{\omega_p^2}{\omega^2 + i\gamma\omega})E, \tag{2.2.16}$$

The new dielectric function for the free electrons becomes

$$\varepsilon(\omega) = 1 - \frac{\omega_p^2}{\omega^2 + i\gamma\omega}, \tag{2.2.17}$$

which can be decomposed into the real, ε_1, and imaginary, ε_2 of the complex dielectric function as

$$\varepsilon_1(\omega) = 1 - \frac{\omega_p^2\tau^2}{1 + \omega^2\tau^2}, \tag{2.2.18}$$

$$\varepsilon_2(\omega) = \frac{\omega_p^2\tau^2}{\omega(1 + \omega^2\tau^2)}, \tag{2.2.19}$$

Eq. 2.2.17 demonstrates that the dielectric constant can become zero near the plasma frequency where the material can support collective modes of oscillating electrons in phase with each other. By tuning the geometry of the structure, the oscillation can occur at negative values of the dielectric constant.

2.3 Effective-medium approximation for linear media

The effective-medium approximation (EMA) is a method of treating a macroscopically inhomogeneous medium, i.e., a medium in which quantities such as the conductivity, dielectric function, or elastic modulus vary in space. Many materials fall into this broad category [90, 91, 92]. One example is a metaldielectric composite, consisting of a collection of metallic and dielectric grains arranged in some ordered or random fashion. Another example is a porous rock. If that rock is filled with salt water, then it is also a composite of an electrical insulator (the rock matrix) and an electrical conductor (the salt water). Yet a third example is a polycrystalline sample of an anisotropic material. Each grain in that polycrystal is, in essence, a different material, since it has a different conductivity or dielectric tensor. (Of course, the tensors in the different grains are generally related by a similarity transformation). A polycrystalline elastic material is a more complicated version of the same problem, since each grain has a different fourth-rank tensor. Quantitative models for the properties of heterogeneous materials have been discussed since the early 19^{th} century. This long-standing attention has led to the presentation of numerous effective medium formulations, being either purely phenomenological or based on more or less sound theories, as treated in several reviews. During the last few years, the interest in the optical properties of metal-dielectric mixtures has soared owing to their importance for efficient photothermal conversion of solar energy. Two effective medium theories have become particularly popular; these are usually ascribed to Garnett (known as the Maxwell Garnett theory) and to Bruggeman [93, 94, 95]. The differences between the mathematical structures of the two theories have been known for some years, but a more intuitive physical understanding for the circumstances under which the two formulations apply is only presently emerging. All these EMA calculations are particularly appropriate for composites and polycrystals in which the grains of the various components are randomly and symmetrically distributed, so that none

of the components is identifiable as a host in which the others are preferentially embedded [96, 97].

2.4 Maxwell Garnett theory

The Maxwell Garnett(MG) approximation, also known as the Clausius-Mossotti approximation, is one of the most widely used methods for calculating the bulk dielectric properties of inhomogeneous materials [98, 99]. It is useful when one of the components can be considered as a host in which inclusions of the other components are embedded. It involves an exact calculation of the field induced in the uniform host by a single spherical or ellipsoidal inclusion and an approximate treatment of its distortion by the electrostatic interaction between the different inclusions. This distortion is caused by the charge dipoles and higher multipoles induced in the other inclusions. The induced dipole moments cause the longest range distortions and their average effect is included in the MG approximation which results in a uniform field inside all the inclusions. This approach has been extensively used for studying the properties of two-component mixtures in which both the host and the inclusions are isotropic materials with scalar dielectric coefficients. It has also been applied in the study of the Hall effect in inhomogeneous materials, where the components have tensor electrical conductivities under applied magnetic field. There are many possible locally anisotropic inhomogeneous materials in which the local dielectric coefficient is a tensor. Of these, the most commonly studied are polycrystalline aggregates of a single anisotropic component. In these materials the inhomogeneity is provided by the random variation of the crystal orientation throughout the system. Many of these studies use the effective-medium approximation [100]. This approximation is based on a self-consistent procedure in which a grain of one of the components is assumed to have a convenient shape (usually spherical or ellipsoidal) and to be embedded in an effective medium whose properties are determined self-consistently.

Consider a random medium composed of core-shell dielectric cylinders of infinite length, shown in Fig. 2.4, embedded in a background medium with a dielectric constant of ε_m. The volume fraction occupied by the inclusions is f and the structure of the core-shell cylinders is shown in the inset of Fig. 2.4. As known, when the incident wavelength λ is much larger than the size of the inclusions, the electromagnetic response of the inclusion can be regarded as a point dipole $\overrightarrow{P}$, and the summation over the total responses of the inclusions within a unit space gives the electric polarization of the random medium [85, 101].

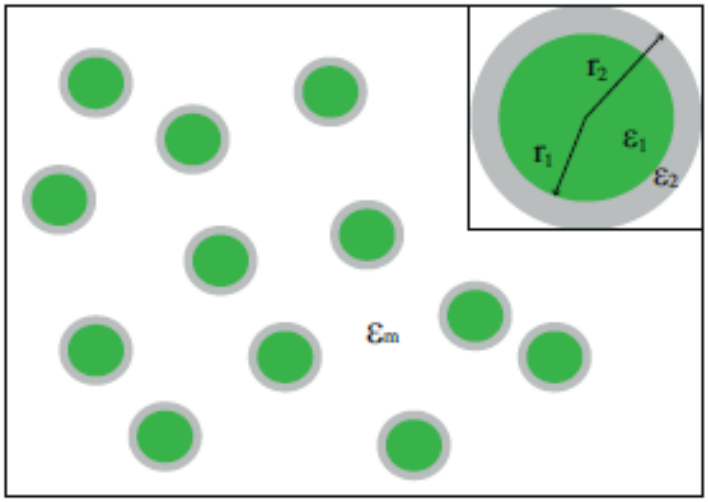

Figure 2.4: Schematic view of a random medium composed of core-shell cylinders of infinite length. The positions of the cylinders are random. The inset is the core-shell dielectric cylinders embedded in the background with a dielectric constant of ε_m.

$$\overrightarrow{P} = \frac{\sum \overrightarrow{P_i}}{\Delta V}, \tag{2.4.1}$$

According to the relation between electric displacement $\overrightarrow{D}$ and electric field $\overrightarrow{E}$, i.e.

$$\overrightarrow{D} = \varepsilon_0 \overrightarrow{E} + \overrightarrow{P}, \tag{2.4.2}$$

the effective dielectric constant to describe the macroscopic effects of the electromagnetic responses of the inclusions can be defined via

$$\overrightarrow{D} = \varepsilon_{eff} \overrightarrow{E}, \tag{2.4.3}$$

Moreover, the average electric displacement and electric field can be given by the weighted average determined by the corresponding values distributed within the respective layers

$$\overrightarrow{D} = f[\eta\varepsilon_1\overrightarrow{E}_1 + (1-\eta)\varepsilon_2\overrightarrow{E}_2] + (1-f)\varepsilon_m\overrightarrow{E}_e, \tag{2.4.4}$$

$$\overrightarrow{E} = f[\eta\overrightarrow{E}_1 + (1-\eta)\overrightarrow{E}_2] + (1-f)\overrightarrow{E}_e, \tag{2.4.5}$$

where f is the volume fraction occupied by core-shell cylinders, $\eta = \frac{r_1^2}{r_2^2}$, $\overrightarrow{E}_1$, $\overrightarrow{E}_2$ and $\overrightarrow{E}_e$ are the electric field distributed within the core-shell, layer of the cylinder,and the background medium, respectively. According to Eqs. 2.4.3, 2.4.4 and 2.4.5 and the formulae for the electric field $E_i(i = 1, 2)$ within the core-shell cylinders, generally, the formulae for the effective dielectric constant ε_{eff} for a random medium composed of core-shell cylinders of infinite length is approximately given by

$$\varepsilon_{eff} = \frac{\varepsilon_m + f[\eta\varepsilon_1 a_1 + (1-\eta)\varepsilon_2 a_2 - \varepsilon_m]}{1 + f[\eta a_1 + (1-\eta)a_2 - 1}, \tag{2.4.6}$$

where the parameters a_1 and a_2 are defined as the ratios between $\frac{\overrightarrow{E_i}}{\overrightarrow{E_e}}$ (i=1,2). The Eq. 2.4.6 is also known as the Maxwell-Garnett formula. Considering the boundary conditions,the electric fields within the multilayered cylinder for S-mode waves are continuous, i.e. $\overrightarrow{E_1} = \overrightarrow{E_2} = \overrightarrow{E_e}$, therefore, $a_1 = a_2 = 1$ Thus, according to Eq. 2.4.6, the effective dielectric constant ε_{eff} for S-mode waves can be written directly by

$$\varepsilon_{eff} = (1-f)\varepsilon_m + f[\eta\varepsilon_1 + (1-\eta)\varepsilon_2], \tag{2.4.7}$$

However,the case for P-mode waves is more complicated,and herein,the field distribution of the electric fields within the coreshell cylinders for P mode is derived and a_1 and a_2 are respectively given by

$$a_1 = \frac{4\varepsilon_m\varepsilon_2}{(\varepsilon_1+\varepsilon_2)(\varepsilon_2+\varepsilon_m) - \eta(\varepsilon_2-\varepsilon_1)(\varepsilon_2-\varepsilon_m)}, \tag{2.4.8}$$

$$a_2 = \frac{2\varepsilon_m(\varepsilon_1+\varepsilon_2)}{(\varepsilon_1+\varepsilon_2)(\varepsilon_2+\varepsilon_m) - \eta(\varepsilon_2-\varepsilon_1)(\varepsilon_2-\varepsilon_m)}, \tag{2.4.9}$$

Therefore, the final solution of ε_{eff} for P-mode waves can be obtained subsequently.

2.4.1 Coated coherent potential approximation method

The coated coherent potential approximation (CCPA) method is conducted as well to calculate the effective index of the random system composed of core-shell dielectric cylinders of infinite length [102, 103]. The mechanism of the CCPA method is based on the physical idea that the distribution of the electromagnetic energy within a random medium should be homogeneous after being configurationally averaged over the correlation length of the random media. Therefore, the averaged forward-scattering amplitude of a cylindrical region within the random medium should be approximately equal to zero. In addition, in order to take into account the effects of the structural factor for the multiple scatterings occurring within the random medium, a coated layer is involved to the real cylinder, which is embedded in the effective medium as an effective scattering unit. The radius of the coated layer is given by $r_c = r_2 f^{-1/2}$. The schematic view of the CCPA method is shown in Fig. 2.5. It has been shown by Busch et al. that the effective medium obtained by the CCPA method for random media composed of dielectric spheres are in reasonable agreement with experiments [104, 105]. According to the

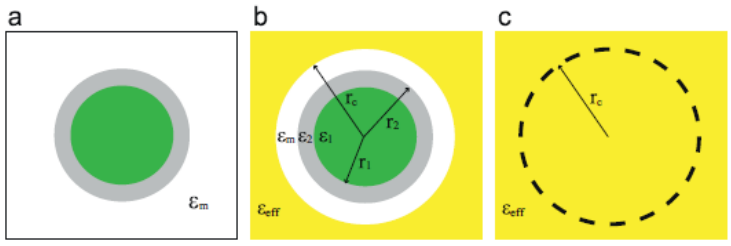

Figure 2.5: Schematic view of the CCPA method for random media composed of coreshell dielectric cylinders, illustrated in (a). The coated layer to the actual coreshell cylinders in (b) has the size of r_c and the dielectric constant equal to ε_m. (c) The dashed region indicates the effective scattering unit described in the CCPA method.

CCPA theory which gives that the coated scattering unit illuminated by a plane wave has a scattering pattern similar to that of its averaged counterpart, thus, the

electromagnetic energy contained in the coated cylinder in Fig. 2.5(b) should be equal to that contained in the dashed volume in Fig. 2.5 (c), which subsequently gives the main equation for the CCPA method as follows:

$$\int_0^{r_c} d^3\overrightarrow{r}\,\rho_E^{(1)}(\overrightarrow{r}) = \int_0^{r_c} d^3\overrightarrow{r}\,\rho_E^{(2)}(\overrightarrow{r}), \tag{2.4.10}$$

where $\rho_E^{(1)}$ and $\rho_E^{(2)}$ represent the electromagnetic energy density within the three-layered cylinder in Fig. 2.5 (b) and that of the averaged volume with an effective ε_{eff} in Fig. 2.5 (c), respectively. In addition, as known, the energy density for an electromagnetic vectorial field is given by

$$\rho_E(\overrightarrow{r}) = \frac{1}{2}[\varepsilon(\overrightarrow{r})|\overrightarrow{E}(\overrightarrow{r})|^2 + \mu(\overrightarrow{r})|\overrightarrow{H}(\overrightarrow{r}|)^2], \tag{2.4.11}$$

here we only deal with non-magnetic materials, so $\frac{\mu}{\mu_0} = 1$. The self-consistent equation, i.e. Eq. 2.4.10, can be solved by an iterative procedure.

2.5 Discrete Dipole Approximation

The Discrete Dipole Approximation (DDA) is developed by Purcell and Pennypacker, it is numerical technique for computing electromagnetic scattering and absorption by targets of arbitrary shape [94, 95], where the continuum target is approximated by a finite point array. In response to the local electric field each point acquires a dipole moment and the scattering problem can then be solved in a self-consistent way. Thus, in principle this method is completely flexible regarding the geometry of the target, the only limitation is given by the need to use an inter dipole separation that is small compared to any structural lengths in the target and to the wavelength. For a finite array of point dipoles the scattering problem may be solved exactly, so the only approximation that is present in the DDA is the replacement of the continuum target by an array of N-point dipoles. The basic idea of the DDA was already known in 1964, but it was limited to structures that were small compared to the wavelength. This limitation disappeared, when Purcell and Pennypacker introduced the DDA to study interstellar dust grains in

1973 [96]. The DDA the problem of electromagnetic scattering of an incident light wave can then be cast to the following simple matrix equation as

$$\overline{AP} = \overline{E_{inc}}, \tag{2.5.1}$$

where $\overline{E_{inc}}$ is a 3N-dimensional (complex) vector of the incident electric field at the N lattice sites, $\overline{P}$ is a 3N-dimensional (complex) vector of the (unknown) dipole polarizations, and $\overline{A}$ is a 3Nx3N complex matrix.

Assuming a point lattice with N occupied sites and an index j = 1, . . . , N running over these elements. Each dipole j is characterized by a polarizability tensor α_j , which is diagonal with equal components if the material is isotropic (i.e., α_j may be treated as a scalar quantity in this case) where all individual dipole polarizability tensors can be simultaneously diagonalized, although it is straightforward to generalize the problem to non diagonal tensors. Let P_j be the instantaneous complex dipole moment of dipole j, and E_{ext}, j the instantaneous complex electric field at position j due to the incident radiation plus the other N-1 oscillating dipoles. Then we get

$$P_j = \alpha_j E_{ext,j}, \tag{2.5.2}$$

$$P_j = \alpha_j (E_{inc,j} - \sum A_{jk} P_k), \tag{2.5.3}$$

in this case $j \neq k$ where E_{inc}, j corresponds to the electric field of the incident plane wave at position j.

$$E_{inc}, j = E_0 e^{(ik.r_j - i\omega t)} \alpha_j, \tag{2.5.4}$$

and $\sum A_{jk} P_k$ is the contribution to the electric field at position j due to the dipole at position k.

2.5.1 Spherical particles: the quasi-static approximation

As described in the previous section, applying electrostatic theory to the problem of scattering and absorption of electromagnetic radiation by small metal spheres (radius $a \ll \lambda$) enables some understanding of the fundamental physical processes

to be gained. The simplest scenario to consider consists of a non-magnetic ($\mu = \mu_0$) sphere surrounded by a homogeneous, linear and isotropic medium that is non-absorbing [106, 107]. It is assumed that the particle initially experiences a uniformly polarised field throughout the entire volume of the sphere. Phase shifts that would exist in a non-uniform field are neglected, thus multipolar resonances predicted by Mie theory are restricted to the dipole mode [108]. The mode is induced by the movement of the electrons relative to the positively charged ion cores of the atomic nuclei under the influence of the externally applied electric field. Provided the permittivities of the sphere and the external medium are different a charge is developed at the surface resulting in a polarisation field within the particle. The external field is modified by the electromagnetic field generated by the polarisation charge [109]. Standard methods in electrostatics can be applied to derive expressions for the electric fields inside (E_1) and outside (E_2) the sphere from the scalar potentials $\varphi_1(r, \theta)$ and $\varphi_2(r, \theta)$ using

$$E_i = -\nabla\varphi_i, i = 1, 2, \tag{2.5.5}$$

and the Laplace equation

$$\nabla\varphi_i = 0, \tag{2.5.6}$$

The boundary conditions at the interface (r = a) between the sphere and the medium necessitate that the potential is continuous $\varphi_1 = \varphi_2$ and that their radial derivatives satisfy

$$\varepsilon_1 \frac{\partial\varphi_1}{\partial r} = \varepsilon_2 \frac{\partial\varphi_2}{\partial r}, \tag{2.5.7}$$

where ε_1 is the complex permittivity of the particle and ε_2 is the permittivity of the external medium. A further condition is that far from the particle the field is unperturbed by the particle

$$E_2 = E_0(r \to \infty), \tag{2.5.8}$$

$$\varphi_2 = -E_0 z = -E_0 r\cos(\theta), \tag{2.5.9}$$

and is equal to the incident field now defined as $E_0 = E_0 z$. Solving Eq. 2.5.6 and applying the boundary conditions yields the following expressions for the potential inside φ_1 and outside φ_2 the sphere,

$$\varphi_1 = \frac{3\varepsilon_2}{\varepsilon_1 + 2\varepsilon_2} E_0 r \cos(\theta), \tag{2.5.10}$$

$$\varphi_2 = -E_0 r \cos(\theta) + a^3 E_0 \frac{\varepsilon_1 - \varepsilon_2}{\varepsilon_1 + 2\varepsilon_2} \frac{\cos(\theta)}{r^2}, \tag{2.5.11}$$

Instantly one can see by comparison with Eq. 2.5.9 that the field outside of the sphere is a superposition of the incident field and the field generated by the particle. By comparison with the equation for the potential due to an ideal dipole

$$\varphi = \frac{p.r}{4\Pi\varepsilon_2 r^3} = \frac{p}{4\Pi\varepsilon_2} \frac{\cos(\theta)}{r^2}, \tag{2.5.12}$$

where p is the dipole moment, the second term in Eq. 2.5.11 is identified as being that of an ideal dipole with moment

$$P = 4\Pi a^3 \frac{\varepsilon_1 - \varepsilon_2}{\varepsilon_1 + 2\varepsilon_2} \varepsilon_2 E_0, \tag{2.5.13}$$

and polarisability α,

$$\alpha = 4\Pi a^3 \frac{\varepsilon_1 - \varepsilon_2}{\varepsilon_1 + 2\varepsilon_2}, \tag{2.5.14}$$

The derivation above has required a spatially constant electric field and has neglected the application of a time-varying electric field. An electromagnetic wave incident on a sphere as defined above naturally has a time-varying electric field and therefore when applying electrostatic theory to these situations is often referred to as the quasi-static approximation. This acknowledges that although spatially invariant at an instant in time, the particle experiences a field with a time dependent phase. The polarisability is related to the absorption and scattering cross-sections by

$$C_{sca} = \frac{k^4}{6\Pi} |\alpha^2|, \tag{2.5.15}$$

$$C_{abs} = k Im\{\alpha\}, \tag{2.5.16}$$

yielding, upon substitution of the polarisability in equation 2.5.14

$$C_{sca} = \Pi a^2 \frac{8}{3} x^4 |\frac{\varepsilon_1 - \varepsilon_2}{\varepsilon_1 + 2\varepsilon_2}|^2, \tag{2.5.17}$$

$$C_{abs} = \Pi a^2 4x Im\{\frac{\varepsilon_1 - \varepsilon_2}{\varepsilon_1 + 2\varepsilon_2}\}, \tag{2.5.18}$$

where $x = ka = \frac{2\Pi a n_2}{\lambda}$ is the size parameter. From these relations it is clear how the absorption, scattering and extinction from a particle small compared to the wavelength depend on the size, wavelength and relative permittivities of the particle and the external medium. For a small particle consisting of a material with a dielectric function only weakly dependent on the frequency of the incident radiation and satisfying the conditions above the absorption is proportional to $\frac{1}{\lambda}$ and the scattering intensity proportional to $\frac{1}{\lambda^4}$. This is known as Rayleigh scattering after Lord Rayleigh who used the relationship to explain the color of a clear blue sky in 1871.

2.6 Modelling optical absorption of nanocomposite using finite difference time domain (FDTD)

Nowadays, nanocomposites attract attention as media with predefined optical properties required for different applications. The design and study of optical properties of nanocomposites is an important problem of contemporary material science [110]. Due to the practical necessities, nanocomposites are often made as thin films and have optical properties which are different from the properties of bulk objects made from the same material [111]. The main reason for these differences consists in the presence of a strongly inhomogeneous local field at the interfaces. These interface effects, for example, are the reason for depolarization phenomena. Transition to the nanoscale has lead to increased interest in many new problems including the localized surface plasmon resonances and increased local field enhancement. Whereas the properties can be understood partly as the result of the behaviors of the constituent materials under the electric field excitation, in many cases the topological features of the interfaces have been shown to play a critical role. For example, the superlens effect, in a self-similar chain of nanoparticles can be used to prepare a subwavelength scale energy localization in the narrow gap separating two neighboring nanoparticles, has been a subject

of recent study, [112, 113] invisibility dips occur in the scattering spectrum of a pair of metallic nanoparticles, which originates from a destructive interference between each surface plasmon mode, and metal nanoparticles, when placed on top of a high-index substrate, can efficiently couple light into the substrate. Despite substantial development to investigate the shape anisotropy for topologically non-trivial structures, many important questions are not yet answered. Of particular interest are the numerical simulations studies, e.g., finite-difference time-domain (FDTD), discrete dipole approximation (DDA), and boundary element method (BEM), which provided important insights into the mechanisms that control the transport properties.

One route to investigating the electromagnetic interaction with nanostructures is through the FDTD method, which is ideally suited for this endeavor. Finite-difference time-domain or Yee's method (see Fig. 2.6 (B)) (named after the Chinese American applied mathematician Kane S. Yee, born 1934) is a numerical analysis technique used for modeling computational electrodynamics (finding approximate solutions to the associated system of differential equations). Since it is a time-domain method, FDTD solutions can cover a wide frequency range with a single simulation run, and treat nonlinear material properties in a natural way. To motivate our approach in the theoretical part, we begin by discussing the computational method performed in this study. First principles calculations presented in this thesis were performed using the FDTD method implemented in the Lumerical FDTD Solutions simulation package. The essential features of our model can be summarized as follows. We use a cubic cell with $1200 \times 1200 \times 1200\ nm^3$ dimensions for these simulations (see Fig. 2.6 (A)). The system was discretized into uniform cubic Yee cells with a side equal to 2 nm, and a time step $\Delta t = 10^{-18}$ s, which satisfies the Courant-Friedrich-Lewy stability criterion[114]. To absorb the outgoing radiation, the computational domain was surrounded by a region of many cells of perfectly matched layers. The coreshell scatterer is illuminated with an incident plane wave, of amplitude E_0, on the XZ plane. We use a Cartesian

coordinate (TFSF) system as a reference system using a total-fieldscattered-field source simulate a plane wave pulse, which is launched in the -Y direction. TFSF sources are used to separate the computation region into two distinct regions, i.e., one that contains the total field (the sum of the incident field and the scattered field), whereas the second region contains only the scattered field. An $exp(-i\omega t)$ time convention is assumed. An appealing approach to this problem is the use of core-shell inclusions. Although the theoretical model of the effective permittivity of coated inclusions has received a substantial amount of interest, most of the analyses cover the composition range far from the resonance and are based on the quasistatic dipole approximation [115, 116].

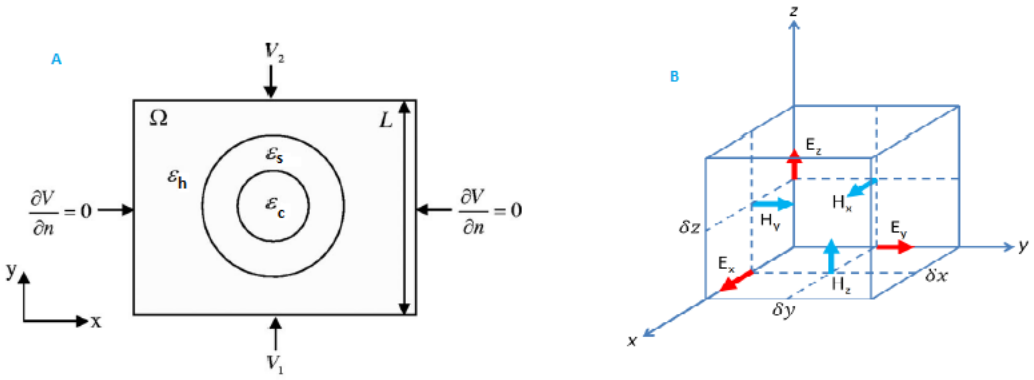

Figure 2.6: (A) Shows schematic view of our model containing unit square cell in the (x, y) plane of a typical core-shell composite structure containing the inclusion and (B) Yee FDTD cell model.

Chapter 3

Experimental methods and Characterization techniques

3.1 Growth system and process of ZnO nanostructure materials

3.1.1 Precursors

The chemicals used in this work were purchased from Sigma Aldrich and used without further purification. Zinc acetate dihydrate ($Zn(CH_3COO)_2 2H_2O$), zinc dichloride ($ZnCl_2$), zinc nitrate hexahydrate ($Zn(NO_3)26H_2O$) and zinc sulphate ($ZnSO_4$) were used as zinc precursors. Ammonium hydroxide (NH_4OH) hexamine ($C_6H_{12}N_4$), sodium hydroxide (NaOH), potassium hydroxide (KOH) and lithium hydroxide (LiOH) were used as the hydroxide sources. Ethanol (98%), doubly de-ionized water ($\rho = 18M\Omega.cm$), 2-propanol and methanol were used as solvents. The passivating agents used were L-cysteine, citric acid and poly(vinylpyrrolidone) (PVP). These materials, apart from acting as passivating agents, also act as chelating and structural directing agents [117].

3.1.2 Substrate preparation

Silicon (100) was chosen as a substrate since large wafers are readily available; it has well known micro-electronic properties and is cheap. The Si substrates were

cleaned by successively rinsing three times in ultra-pure boiling trichloroethylene (TCE), acetone and methanol, followed by rinsing in DI water.The substrates were etched in 10% hydrofluoric acid (HF) for 1 min before a final rinse in DI water, and then were blown dry in nitrogen gas.

3.1.3 Seed layer preparation

Two methods were used to synthesise the ZnO seed layer: the solvothermal reaction of zinc acetate dihydrate with different hydroxide precursors and the thermal decomposition of zinc acetate dihydrate in ethanol. In the first method,the zinc precursor (zinc acetate dihydrate) was dissolved in ethanol or 2-propanol at room temperature. At the same time, the hydroxide precursor (NaOH, LiOH or KOH) was dissolved in ethanol or 2-propanol at room temperature. These two precursors were then mixed at different temperatures, depending on the growth conditions being investigated. The temperatures ranged from 0 ^0C (ice bath) to 60 ^0C (hot plate) and the mixture was continuously stirred for two hours. It was found that, irrespective of the alcohol or hydroxide used, for reactions that occurred at temperatures between 40 ^0C and 60 ^0C the final product formed a precipitate at the bottom of the reaction beaker after cooling to room temperature. The top of the solution, which looked relatively clear, was decanted and the remaining solution centrifuged and washed several times, yielding a powder. The powder was finally dispersed in methanol and then spin-coated onto a pre-cleaned substrate. In the second method, different amounts (depending on the desired concentrations) of zinc acetate dihydrate were dissolved in pure ethanol and agitated at 30C for 30 min. In addition, 10 mg PVP was dissolved in 10 ml of ethanol at the same temperature. The PVP solution was then added to 20 ml of the zinc acetate solution. PVP forms a shell surrounding the particles to prevent them from aggregating thus promoting the formation of mono-dispersed nanoparticles. The resultant solution was allowed to react for an additional 30 min, after which it was spin coated onto a Si (100) substrate using a spin coater operated at 2000 rpm for 30 s. Each

substrate was spin coated multiple times (according to the experimental conditions desired). The coated substrate was then annealed in flowing O_2 at 300 ^0C, which exceeds the thermal decomposition temperature of zinc acetate dihydrate (250 ^0C), after which the coating and annealing processes described above were repeated once more. Further details of the techniques and the results obtained are discussed in the fourth chapter of experimental section.

3.1.4 Seeding techniques

Both spin coating and dip coating were used to prepare the seed layers. It was found that spin coating yielded a more uniform distribution of nanoparticles compared to dip coating. Because of this, spin coating was chosen as the better seeding technique, and was used in all samples prepared for this investigation. Based on several attempts, the spin coating speed and spinning time was set to be 3000 rpm and 30 sec, respectively.

The thermal decomposition approach to seed layer fabrication can produce high quality ZnO nanoparticles which are free of defects. It is reproducible, simple and economical. The best conditions found to produce the desired objectives are as follows:

- Metal salt: Zinc acetate (usually the dihydrate form) as the metallic salt.
- Solvent: An organic solvent. However, there is no clear conclusion as to which is best, since reports have shown that methanol, ethanol, isopropanol, n-butanol and 2 methoxyethanol all yield good quality ZnO films [118]. In general, alcohols (ethanol in the present case) were preferred for the experiments since the formation of $Zn(OH)_2$ (instead of ZnO) was found to be favoured when water was used.
- Concentration: Based on the objective of achieving evenly dispersed nanoparticles on the substrate, concentrations of 0.5 mM to 1 mM of zinc acetate resulted in better orientation and distribution of subsequently grown nanorods.

Higher concentrations can be used, but results in a higher density of nanoparticles on the substrate, which in turn leads to the formation of a continuous thin film due to the high density of rods.

- Coating: As previously stated, spin coating yielded more uniform and repeatable results. It is an easy technique to use and both the spin time and spin speed are readily controlled.

- Coating time: This parameter is dependent of the concentration of solvent used. For 1 mM zinc acetate in ethanol, repeated coating (typically two times) followed by annealing at 300 ^0C for 30 min in oxygen between coatings. In addition sonicating in ethanol bath after annealing to remove any by-products yielded the best results.

3.1.5 Synthesis of ZnO nanorods

ZnO nanorods were grown using a combination of zinc nitrate hexahydrate as a zinc precursor and ammonium hydroxide or hexamine as a source of hydroxyl groups. These two precursors were dissolved separately in DI water at room temperature. The zinc precursor was placed in a water bath while being stirred. When the temperature of the solution reached $\sim 40\ ^0C$, the hydroxide precursor was added drop-by drop. The solutions were mixed for approximately 1 min. The seed coated substrate was placed in the sample holder as soon as mixing was complete, and the reaction vessel was covered. The growth of the rods is summarised briefly:

- Metal salt: Zinc nitrate (usually in hexahydrate form) was used as the metal salt. It dissolves in water at room temperature. Other zinc salts can also be used, but care should be taken as the anion group of the zinc molecule reacts with the cation group of the hydroxide and can cause complications. Since both the zinc and hydroxide precursors contain nitrogen-based cations, no secondary phases/by-products were expected or observed in this research.

- Hydroxide source: Ammonium hydroxide and hexamine were used. Both precursors dissolve in water at room temperature.

- Solvent: De-ionized water, ethanol and 2-propanol

- VI/II ratio: This ratio depended on the type of hydroxide source used. Using NH4OH as a hydroxide source, a VI/II ratio of around 1 : 1 resulted in nanoparticles while a higher ratio of 40 : 1 resulted in the formation of nanorods. When using hexamine as the hydroxide source, a 1 : 1 ratio yielded nanorods. This difference is due to the different decomposition mechanisms of the two precursors.

- Concentration: The precursor concentrations were varied while keeping the VI/II ratio constant. In general, low concentrations produced thinner nanorods and higher concentrations produced longer, thicker rods. However, the precursor concentration was not the only factor affecting the length and radius of the rods but also depends on growth temperature.

- Mixing conditions: A water bath was preheated to the desired growth temperature before placing the zinc solution in the bath. When the zinc solution reached the required temperature (varied from $25 - 80\ ^0C$), the hydroxide precursor was added drop by drop. Formation of zinc hydroxide phase was observed when mixed at temperatures below $40\ ^0C$. Mixing at temperatures greater than $60\ ^0C$ resulted in fast precipitation resulting in less efficient growth on the substrate. The optimum mixing temperature was found to be $40\ ^0C$.

- Cooling rate: The sudden termination of growth, or the removal of the sample from the growth solution after cooling to room temperature, shown to affect the morphology of the rods [119]. The tip morphology also depends on the pH of the solution and the growth rate [120]. No detailed experiments were conducted to evaluate this, however the samples grown in this study

were removed from the water bath before cooling to room temperature.

- Drying process: The samples were rinsed several times in DI water and gently blown dry using nitrogen gas.

Synthesis of ZnO nanorods using a simple CDB technique which involves a two-step process are summarized as:

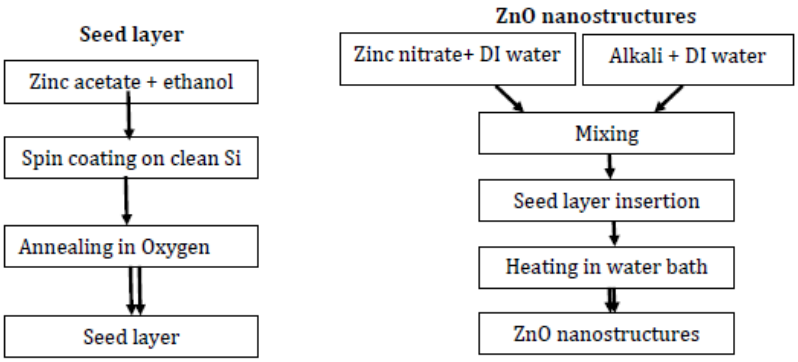

3.2 Luminescence in ZnO

Light emission through any process other than blackbody radiation is called luminescence and requires external excitation as it is a non-equilibrium process. Based on the excitation source, luminescence is referred to either as photoluminescence (PL) (caused by absorption of photons), electroluminescence (EL) (caused by electric current), cathodoluminescence (CL) (caused by an electron beam), chemoluminescence (caused by chemical reactions) or thermoluminescence (caused by heat). In this section, the basic principles of PL and the possible emission lines in ZnO are described [121, 122].

Luminescence in semiconductors is the direct result of electron transitions from higher to lower energy levels. PL is a powerful tool to study point defects in wide-band gap semiconductors. Fig. 4.10(a) shows the simplified band structure of a semiconductor near the centre of the first Brillouin zone, where a material with band gap energy Eg is irradiated by a laser with energy $h\nu > E_g$,resulting in the excitation of an electron into the conduction band (arrow 1) and leaving a hole

behind in the valence band. An electron-hole (e-h) pair is thus generated. The electrons and holes thermalize to the lowest energy state of their respective bands via phonon emission (shown by the red-wavy arrows) before recombining (arrow 2) across the fundamental band gap or the defect levels within the band gap and emitting photons of the corresponding energies in two basic mechanisms [123]. These

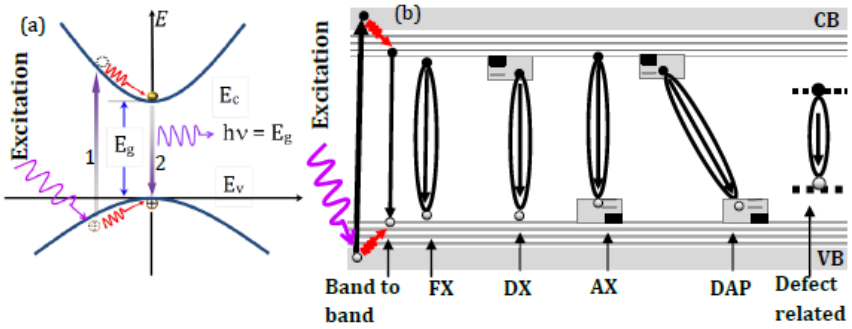

Figure 3.1: Band diagram illustration of the different processes that make up the photoluminescence spectra: (a) excitation, relaxation and recombination in k-space, and (b) possible mechanisms of e-h recombination [55].

are radiative and non-radiative recombination. When the electronhole recombination results in photon emission, the process is called radiative recombination. A recombination process that does not produce photons is known by non-radiative recombination in which the energy is exchanged with the lattice as heat through phonon emissions within defect states in semiconductor or transferred its energy to other carriers. Non-radiative recombination occurs mainly through three physical mechanisms, but cannot be detected by PL. These are Auger recombination, recombination at defects in the bulk, and surface recombination. During Auger recombination the e-h pair energy is transferred to a third free carrier that will move to a higher energy in the conduction band (in the case of an electron) or to a lower energy in the valence band (in the case of a hole). The e-h pair thus recombines without photon emission. This is a three-body process because an electron and two holes or a hole and two electrons are involved. Since this is a three-particle interaction, it is normally only significant in non-equilibrium conditions when the carrier density is very high. For this reason, it only occurs under

very high injection levels or for materials with high equilibrium carrier concentrations. Based on the wide band gap and non-degeneracy of the valence band, it is suggested that Auger recombination is not important in ZnO [124, 125, 126].

Recombination at defects in the bulk and surface regions of ZnO are expected to be the major non-radiative recombination processes. In particular, surface related non-radiative recombination is most pronounced in nanostructures [127].

Fig. 4.10(b) illustrates commonly observed radiative recombination mechanisms. The optical transitions in a semiconductor can either be intrinsic or extrinsic. Intrinsic transitions deal with the transitions from conduction to valence band, including excitonic effects due to coulomb interactions. Extrinsic transitions are related to dopants and defects that create discrete energy levels inside the band gap and hence influence the optical properties. In the case of ZnO, a PL spectrum at room temperature usually contains two emission bands resulting from both effects. These emission bands can be categorized as near band edge emission (NBE), associated with intrinsic effects, and deep level emission (DLE), caused by extrinsic effects. Brief descriptions of the possible transitions are discussed below.

3.2.1 Free excitons (FX)

It is possible for an electron and a hole to become bound together into a hydrogen atomlike arrangement which can move in a crystal. This coulomb-coupled electron-hole pair is called an exciton. In a pure material without any defects or impurities (an intrinsic semiconductor), an e-h pair is perfectly free to move throughout the material, and thus this type of particle is called a free exciton (FX). Since the coulomb interaction lowers the energy of the electron-hole pair, the difference between the electron and hole energies of the coupled pair is less than that of the band gap energy. Mathematically,

$$E_G = E_{Fx} + E_{bind}, \tag{3.2.1}$$

where E_{bind} is the binding energy of the exciton and E_{Fx} is the energy of free exciton. Considering the hydrogen atom-like arrangement

$$E_{bind} = -\frac{R}{n^2}, R = \frac{\mu}{m_0}\frac{1}{k_0^2}R_H and \mu = \frac{m_e m_h}{m_e + m_h}, \tag{3.2.2}$$

where n is the principal quantum number, R_H is the Rydberg constant for the hydrogen atom, k_0 is the static dielectric constant and m_e,$m_h$are the electron and hole effective masses. Hence:

$$E_{Fx} = E_G - \frac{\mu}{m_0}\frac{1}{(nk_0)^2}, \tag{3.2.3}$$

The ground state ($n = 1$) exciton binding energy in ZnO is $\sim 60meV$ [9].

3.2.2 Bound excitons (BE)

In most materials there are finite concentrations of impurities or defects. Any disruption of the periodicity of a lattice (due to impurities, vacancies, dislocations and even large scale defects such as surfaces) may either destroy an exciton or localize it. As a result, it is possible for excitons to be trapped at these defects; the resulting configuration is called a bound exciton (BE). Energy is the fundamental criterion that determines whether or not a free exciton can be trapped. If the total energy of the system is reduced when the free exciton is in the vicinity of the defect, then it is energetically favourable for the exciton to remain near the defect and the exciton becomes bound via van der Waals interactions (in the case of the exciton binding to a neutral acceptor or donor). An exciton bound to an ionized donor (D^+X)/acceptor (A^-X) is a complex consisting of a donor (acceptor) ion and an e-h pair. A neutral donor (D^0X)/acceptor (A^0X) bound exciton consists of a donor (acceptor) element and an e-h pair. The photon energy emitted from any of these transitions is given by:

$$E_{BE} = E_{Fx} - E_{loc}, \tag{3.2.4}$$

where E_{loc} is the exciton localization energy, which is the energy required to remove the exciton from the impurity. This localization energy is related to the impurity

binding energy E_i using the Haynes empirical rule [128]:

$$E_{loc} = a + bE_i, \tag{3.2.5}$$

where a and b are constants and are determined by fitting to experimental values. The PL spectrum of ZnO usually exhibits a large variety of different luminescence lines covering almost the whole visible and near UV spectral range from 1.8 eV to 3.37 eV. The strongest luminescence is typically found near the fundamental band edge, with particularly diverse emission lines at low temperatures, which originate from the radiative recombination of free and bound excitons [129]. The room temperature PL spectrum of ZnO usually contains two emission bands as shown in Fig. 3.2. These emission bands can be categorized as NBE emission and DLE. The NBE emission is caused by free excitons recombination, while the DLE is caused by carriers bound to deep levels.

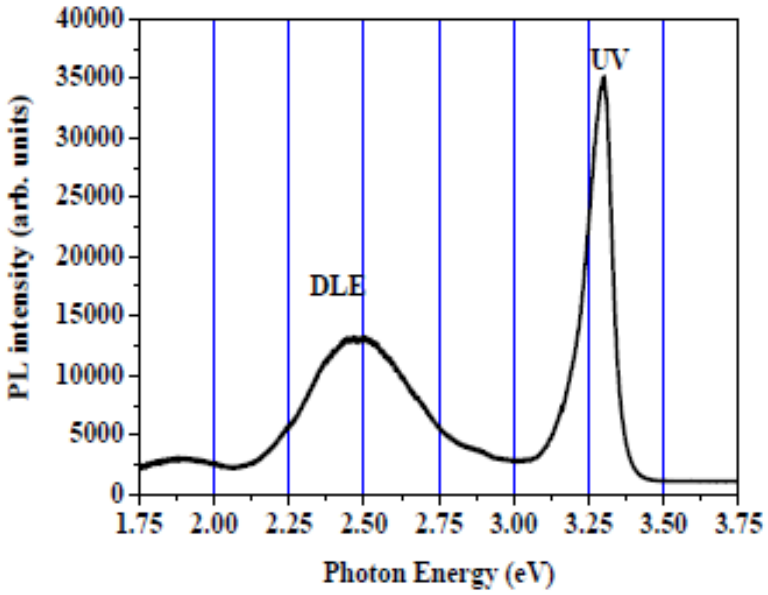

Figure 3.2: A typical PL spectrum of a ZnO crystal at room temperature

3.2.3 Shallow Donor-Acceptor Pair transitions (DAP)

When donor and acceptor impurities both present in material at a close proximity so that their wave function overlaps, a loosely bound donor electron can radiatively

recombine with a hole on to a neutral acceptor. This process is called donor-acceptor pair (DAP) recombination. The emission energy of the DAP is a function of the inter-pair distance (r) through the final state interaction between the donor and the acceptor. Using conservation of energy, if an electron from a donor (with binding energy E_d) recombines with a hole on an acceptor (with binding energy E_a) which is at a distance r from the donor, E_{DAP} can be related to E_G as:

$$E_G = E_d + E_a + E_{DAP} + U, \tag{3.2.6}$$

where U is the coulomb interaction energy of the ionized donor and acceptor pair (i.e. in their final state), and is given by:

$$U = K_s \frac{e(-e)}{r} = \frac{-e^2}{4\Pi\varepsilon_s r}, \tag{3.2.7}$$

where ε_s is the relative permittivity of the material. Hence

$$E_{DAP} = E_G - (E_a + E_d) + \frac{e^2}{4\Pi\varepsilon_s r}, \tag{3.2.8}$$

Since acceptors and donors are located in a lattice, only discrete values of r can be assumed. The bigger the separation of the pair, the smaller the Coulomb interaction and thus the lower the photon energy is. The emission intensity should then increase as the pair separation decreases. In the case of partially ionic bonding as in ZnO, such a transition causes polarization of the crystal lattice, which leads to lattice distortions. As a result, the DAP transition is always followed by phonon replica transitions. In ZnO, the energy separation between longitudinal (LO) phonon replicas is 72 meV [2].

3.2.4 Two-electron satellite transitions (TES)

Another characteristic of the neutral-donor-bound-exciton transition is the two-electron satellite (TES) transition in the spectral region of $3.32 - 3.34$ eV [130]. These transitions involve radiative recombination of an exciton bound to a neutral donor, leaving the donor in the excited state, thereby leading to a transition energy

which is less than the DBE energy by an amount equal to the energy difference between the first excited and ground states of the donor. In the effective-mass approximation, the energy level E_{TES} of the TES is given by:

$$E_{TES} = E_{D^0X} - E_D(1 - \frac{1}{n^2}), \tag{3.2.9}$$

For first excited state (n = 2):

$$E_{TES} = E_{D^0X} - \frac{3}{4}E_D, \tag{3.2.10}$$

Re arranging, the donor binding energy can be given by:

$$E_D = \frac{4}{3}(E_{D^0X} - E_{TES}), \tag{3.2.11}$$

This implies that knowing the energy positions E_{D^0X} and E_{TES} of the D^0X and its corresponding TES transition, the related donor binding energy, E_D, can be obtained. The same formulation holds for A^0X, but the A^0X transition and consequently its corresponding TES are seldom observed in ZnO.

3.2.5 Quantum confinement effects

Quantum confinement occurs in nanocrystals when their size is reduced so that it approaches the size of the exciton Bohr radius (the size of an exciton in a bulk crystal). For ZnO, the exciton Bohr radius is $\sim$ 2.34 nm [131]. PL can be used to observe the quantum confinement effect in nanostructures. However, there are few reports on this effect in ZnO nanostructures. Experimental evidence of quantum confinement effects have been reported by Guet al.[132], where PL and absorption spectra from nanorods with radii of 1.1 nm were found to be blue shifted compared to the spectra of bulk materials. Lu et al.[133] also observed quantum confinement effects in the PL spectra of quantum dots with diameter as large as 15 nm and 6 nm in height. The quantum dots studied by Lu et al. exhibited a strong free exciton adsorption at 3.41 eV at room temperature, significantly larger than that in bulk ZnO (3.37 eV), representing a 90 meV blue-shift.

3.3 Synthesis of ZnO nanostructures

Nano-materials have attracted tremendous interest due to their noticeable performance in electronics, optics and photonics. These materials are typically classified in three groups: zero-dimensional, one-dimensional and two-dimensional. Zero-dimensional (0D) nanostructures, referred to as quantum dots or nanoparticles with an aspect ratio near unity, have been extensively used in biological applications [134, 135, 136, 137]. Two-dimensional (2D) nano-materials, such as thin films, have also been widely used for optical coatings, corrosion protection and semiconductor thin film devices. One-dimensional (1D) semiconductor nanostructures such as nanowires, nanorods, nanofibres, nanobelts, and nanotubes, have been of intense interest in both academic research and industrial applications because of their potential as building blocks for other structures [138, 139]. One dimensional nanostructures are useful materials for investigating the dependence of electrical and thermal transport or mechanical properties on dimensionality and size reduction [140, 141]. They also play an important role as both interconnects and functional units in the fabrication of electronic, optoelectronic, electrochemical and electromechanical nanodevices [142, 143]. Among the 1D nanostructure, ZnO nanowire is one of the most important nano-materials for nanotechnology today [144, 145, 146].

Among various synthesis method, vapour phase synthesis is probably the most extensively explored approach in the formation of 1D nanostructure [147]. A typical vapour phase synthesis method takes place in a closed chamber containing a gaseous environment. The vapour species are first produced by evaporation, chemical reduction and gaseous reactions. The species are then transferred and condensed onto the surface of a solid substrate. Generally, the vapour phase synthesis process is carried out at temperatures higher than the decomposition temperature of the precursors. Solution phase synthesis has many advantages when compared to vapour phase synthesis, such as low cost, low temperature,

scalability and ease of handling. Generally, liquid phase reactions occur at relatively low temperatures ($< 200\ ^0C$) compared to vapour phase synthesis methods. Thus, solution synthesis methods allow for a greater choice of substrates, including inorganic and organic substrates. Due to these many advantages, liquid phase synthesis methods have attracted increasing interest. In liquid phase synthesis, the growth process can be carried out either in aqueous or organic solutions, or a mixture of the two. A number of specific methods have been developed, two of which are used in the present study are:

- The sol-gel technique [148] is a wet chemical technique used in the fabrication of metal oxides from a chemical solution, and this acts as a precursor for an integrated network (gel) of discrete particles. The precursor solution can be either deposited on the substrate to form a film, cast into a suitable container with the desired shape, or used to synthesize powders.

- Chemical bath deposition [149]. CBD is a technique that produces a solid film on a substrate during a single immersion through the control of the kinetics of formation of the solid. It is the aqueous analogue of chemical vapour deposition (CVD), since both processes involve the mass transport of reactants, chemical reaction, nucleation, desorption, and growth. CBD is particularly suitable since it does not require high-pressure containers and is also entirely recyclable, safe and environmentally friendly, because only water or alcohols is used as a solvent. The safety hazards of organic solvents and their eventual evaporation and potential toxicity are avoided using this method. In addition, because no organic solvents or surfactants are present, the purity of the materials is substantially improved. Nanostructures produced using this method is self-assembled without any external manipulation. The by-products (residual salts) are easily washed out by water due to their high solubility. In most cases, no additional heat or chemical treatment is necessary, which represents a significant improvement compared with surfactant, template, or membrane based synthesis methods. This method is

thus an increasingly important complement to other solution-based techniques in the fabrication of nanostructures. The details of the methods are discussed in the next sections.

3.3.1 Growth of ZnO nanostructures using chemical bath deposition

The first recorded report of CBD crystal growth was published in 1933 by Bruckman who produced a PbS thin film from a solution containing lead acetate, thiourea and sodium hydroxide [150]. Since then CBD has been used to deposit films of a variety of semiconductors. Despite the experimental simplicity, it is a complicated task to understand the mechanisms involved in the deposition process. The overall approach involves several steps, beginning with dissociation in solution and thermal treatment for the desired crystal growth. During each step, a variety of parameters must be controlled. These include the concentrations of the precursors, the molar ratio of the metal to the base precursors, pH of the solution, growth time, growth temperature and the like. These parameters are discussed in more detail in chapter 4. The large number of variables and the co-dependency amongst the variables makes CBD tiresome and causes difficulties on the cause-effect relationship between variables. In principle, CBD can be used to deposit any compound that satisfies the following two basic requirements: (1) the source of cations (metal) and anions (hydroxide) must dissolve preferably in water (or alcohol) and must form a crystal; and (2) the formed crystal must be insoluble and chemically stable in the solvent used. The crystal formed can grow either by homogeneous nucleation in solution and/or by hetero-nucleation on a substrate. Homogeneous nucleation can occur due to local fluctuations in the solution concentration, temperature, or other variables. The first stage of the growth is collision between individual ions or molecules to form embryos. These embryos grow by collecting individual species that collide with them. In this type of growth, adsorption of ions on the embryo is expected to be the most probable

growth mechanism. If the concentration of embryos in the solution is large, collisions between embryos can also play an important role. Heterogeneous nucleation may take place as a result of two distinct mechanisms. The first one is a growth mechanism involving the reaction of atomic species at the surface of stable nuclei pre-coated onto the substrate or impurities on it. It corresponds to an atom-by-atom process, also called "ion-by-ion" [90]. The second deposition mechanism is associated with the oriented attachment (for polar crystals) of particles formed by homogeneous nucleation on the wetting/seed layer pre-coated onto the substrate [91, 92]. It can be considered a cluster-by-cluster growth. Whatever mechanism dominates, the general steps in such solution growth are expected to be: generation of growth species, diffusion from the bulk to the growth surface, adsorption and surface growth.

The balance between homogeneous and heterogeneous nucleation processes depends on the deposition mechanism. One of the key parameters for synthesizing nanostructures in solution is controlling the supersaturation of the reactants. Although quantitative information is not readily available to fully understand supersaturation during the nucleation and crystal growth processes of 1D nanostructure, some general guidelines can still be of use. It is generally believed that high supersaturation levels favour homogeneous nucleation, whereas low supersaturation levels favour heterogeneous nucleation [77]. In order to maintain low supersaturation levels during the growth process, the nutrient supply has to be finely controlled. The formation of larger nuclei, which leads to precipitation, when the objective is to grow on pre-seeded substrates, is a waste of reagents. One common technique is the use of seeding layers to facilitate heterogeneous nucleation. Moreover, seeding of the substrate with nanoparticles lowers the thermodynamic barrier by providing nucleation sites, and hence improves the aspect ratios and optical properties, and ensures uniformity in the growth of ZnO nanostructures [93, 94]. This implies that any factor that will improve the seed layer will improve the as synthesized nanostructures. In addition to supersaturation, the other

main parameters that affect these nucleation processes are pH and temperature. Temperature in particular is an important thermodynamic factor and plays a key role in controlling crystal growth rate. Higher temperatures enhance the kinetic energy of the precursors and this favours homogeneous nucleation in the solution.

3.4 Sol-Gel Method

The obtaining of ZnO nanopowders by the sol-gel method is the subject of much interest, in view of the simplicity, low cost, reliability, repeatability and relatively mild conditions of synthesis, which are such as to enable the surface modification of zinc oxide with selected organic compounds. This changes in properties and extends its range of applications. The favourable optical properties of nanoparticles obtained by the sol-gel method have become a common topic of research. Benhebal et al. [47] prepared ZnO powder by sol-gel method from zinc acetate dihydrate, oxalic acid, using ethanol as solvent. The obtained product was characterized by using techniques such as nitrogen adsorption isotherms, X-ray difration (XRD), scanning electron microscopy (SEM), an UV-Vis spectroscopy. The prepared zinc oxide has a hexagonal wurtzite structure with the particles of a spherically shaped. A surface area obtained by the BET method of the calcined ZnO powder is equal to 10 m^2/g, characteristic of a material with low prosity, or a crystallized material. The sol-gel method was also used to obtain nanocrystalline zinc oxide by Risti et al. [112]. A solution of tetramethylammonium hydroxide (TMAH) was added to a solution of zinc 2-ethylhexanoate (ZEH) in propan-2-ol. The resulting colloidal suspension was left for 30 min (alternatively for 24 h), and was then washed with ethanol and water. TMAH is a strong organic base, which comparably with an inorganic base (e.g., NaOH) is characterized by a pH of ~ 14. This high pH means that metal oxides are not contaminated with the cation from the base, which may have an effect on the ohmic conductance of the oxide material. A determination was made of the effect of the quantity of ZEH used and the maturing time of the

colloidal solution. TEM images showed that the ZnO particles obtained have sizes of the order of 2050 nm. The quantity of ZEH has a negligible effect on the particle size. Yue et al. [113] also obtained ZnO by the sol-gel method. High-filling, unifrom, ordered ZnO nanotubes have been successully prepared by sol-gel method into ultrathin AAO membrane. Integrating the ultrathin AAO membranes with the sol-gel technique may help to fabricate high-quality 1D nanomaterials and to extend its application as a template for nanostructures growth. In the present work, sol-gel technique has been used, the effect of dopants(Cd, Al) on ZnO structures, optical and magnetic properties are studied.

3.5 Characterisation techniques

Different characterisation techniques were used to investigate the structural, optical and magnetic properties of the samples. Scanning electron microscopy (SEM) was used to investigate the morphology of the nanorods, while their crystallinity and crystal structure were determined using a powder x-ray diffractometer (XRD). Energy dispersive x-ray spectroscopy (EDX) was used to estimate the elemental composition of the samples. The optical properties were investigated by microphotoluminescence (PL) measurements. Finally,the ferromagnetic properties of the samples are analyzed using electron paramagnetic resonance (EPR). A brief introduction to these techniques is presented in the following sections.

3.5.1 X-ray diffraction (XRD)

X-ray diffraction provides structural and physical information of crystalline materials. In particular, XRD analysis can provide the crystalline quality and dominant crystallographic planes of the given material. In addition, the diffraction spectrum also provides information regarding the types of phases present in the material and can be used to calculate the approximate average grain size using Scherrers equation [113]. In this study, a Philips PW 1840 powder and Bruker

D8 (Bruker Corporation of Germany) diffraction system with a resolution of 0.02 ^{0} for 2θ and a $Cu - K\alpha$ x-ray beam ($\lambda = 1.5405\dot{A}$) was used.The x-ray scans were performed between 2θ values of 30 ^{0} and 80 ^{0} using a step size of 0.05. The crystalline quality, the type of phases present in the samples and the orientation of the rods with respect to the substrate surface were deduced from the analysis. The typical X-ray diffractometer used in this study is a Bruker AXS Discover diffractometer for the samples prepared by sol-gel route is shown in Fig. 7.1. In

Figure 3.3: The X-ray diffractometer used in this study is a Bruker AXS Discover diffractometer.

almost all samples of the rods, peaks related to the (0002) plane were observed to dominate the spectrum. The relative intensity of this diffraction plane with respect to other dominant planes, $(10\bar{1}0)$ and $(10\bar{1}1)$, were used as a measure of the alignment of the rods. The diffraction of the (0002) plane for ZnO is at 34.43 ^{0}, with $d_{0002} = 2.60\ \dot{A}$. For the samples prepared by sol-gel techniques it is explained under each section of the chapters.

3.5.2 Scanning electron microscopy (SEM) and energy dispersive x-ray spectroscopy (EDX)

Scanning electron microscopy is useful for the exploration of a diversity of specimens in various fields such as materials science, semiconductor research and microelectronics [114]. In the present study SEM has primarily been used for surface visualization of the ZnO samples. The surface morphology and elemental composition of the ZnO powders were investigated using a Shimadzu Superscan SSX-550 electron microscope equiped with an energy dispersive x-ray spectroscope (EDX). Like XRD, it is a non-destructive technique commonly used for surface analysis. It is capable of producing high resolution images, both planar and in cross-sectional views. Electron microscopy takes advantage of the wave nature of rapidly moving electrons. In the microscope, a beam of electrons is generated in a vacuum. The beam is collimated by electromagnetic condenser lenses, focused by an objective lens, and then scanned across the surface of the sample by electromagnetic deflection coils. The primary imaging method is by collecting secondary electrons that are released by the sample. The electrons are detected by a scintillation material that produces flashes of light from the electrons. The light flashes are then detected and amplified by a photomultiplier tube. By correlating the sample scan position with the resulting signal, an image can be formed that is strikingly similar to what would be seen through an optical microscope. Beside the emitted electrons, x-rays are also produced by the interaction of electrons with the sample. These x-rays are characteristic of the elements present in the sample and can be detected in a scanning electron microscope coupled with an x-ray analyzer such as the energy dispersive x-ray spectrometer (EDX) [115]. The typical SEM equipment coupled with EDX: SHIMADZU Superscan model SSX-550 used in the study is shown in Fig. 1.2

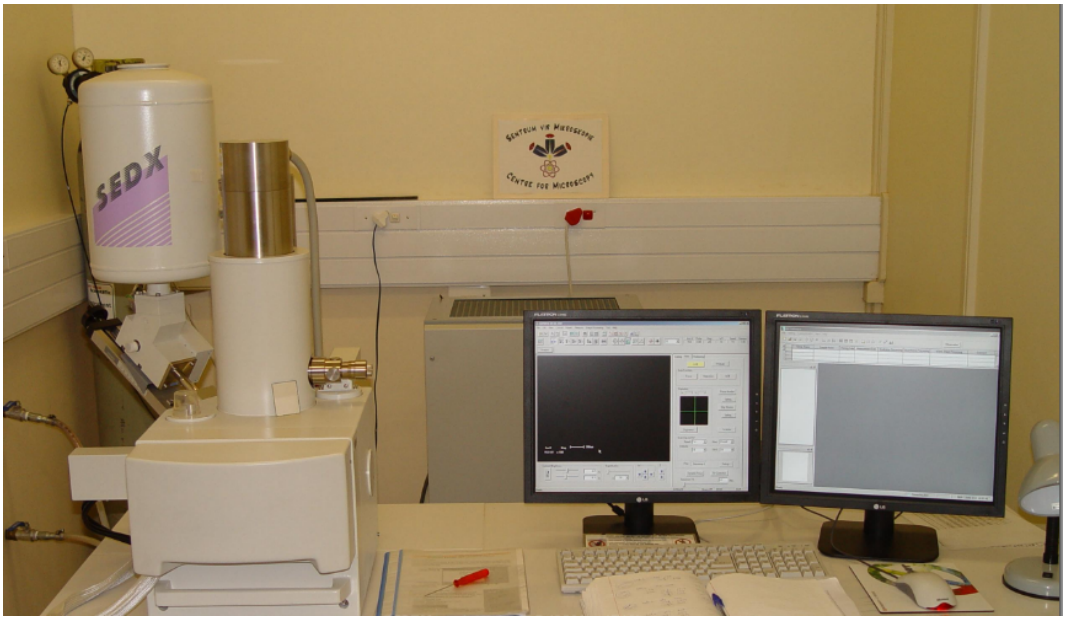

Figure 3.4: The SEM equipment coupled with EDX: SHIMADZU Superscan model SSX-550.

3.5.3 Photoluminescence (PL) Spectroscopy PL

PL is a process in which a substance absorbs photons and then re-radiates photons. PL is a non-destructive technique requiring no or little preparation of a sample. Different types of samples (powder, liquid or bulk semiconducting material) can be characterised. PL measurements are usually performed using two different excitation conditions. Firstly, when excitation is with a continuous beam, the material can reach a steady state. The PL measured under these conditions, called continuous wave (CW) or steady state PL, provides information mainly on the position of the electronic levels participating in the radiative recombination processes. Secondly, when PL is excited using light pulses of suitable duration, time-resolved PL (TRPL) is obtained and the excited state lifetime, which provides information on carrier dynamics and recombination kinetics, can be extracted.

For CW-PL, the sample is excited by a laser with energy greater than its band gap and the luminescence intensity is measured as a function of wavelength or energy. The heart of this optical measurement system is a monochromator, which is used to differentiate between emissions at different photon energies, resulting in

a plot of light intensity as a function of energy. Optical measurements provide information both about the host semiconductor, through intrinsic optical processes, and about the wide variety of impurities or defects which are endemic in all real semiconductor materials, through extrinsic optical processes. It is particularly suited for the detection of shallow-level impurities, but can also be applied to certain deep-level impurities/defects, provided that their recombination is radiative [116]. Fig. 3.5 depicts an experimental set-up for CW-PL measurements using photomultiplier tubes or semiconductor photodiodes. The luminescence is spectrally analysed using a grating monochromator and, depending on the emitted photon energy, detected using either a photomultiplier tube or a photodiode. In this study, a PC controlled monochromator was used for wavelength tuning. The laser radiation was chopped by a mechanical chopper to allow signal amplification with a lock-in amplifier; alternatively, photon counting techniques may be used.

In this study, the PL characterization system employed were; a SPEX 18700.5 m spectrometer system, equipped with a HeCd laser lamp as the excitation source and a Cary Eclipse fluorescence spectrophotometer (Model: LS 55). Samples for the laser system were excited at 325 nm and emission observed in the wavelength range 400 to 600 nm at room temperature. In addition a mini-PL UV laser system 5.0 (Photon systems, USA), which uses a Ne- Cu laser with an excitation wavelength of 248.6 nm, and a closed-cycle He cryostat with a Kimmon IK 3252R-E He-Cd laser (excitation $\lambda = 325$ nm).

Low temperature PL is used to obtain specific information about the centres which promote impurity related recombination, the donors and acceptors, and this can only be obtained when the carriers are "frozen out" in these centres. There is also a dramatic reduction in the spectral broadening caused by the coupling of carriers with phonons, called vibronic processes, at low temperatures.

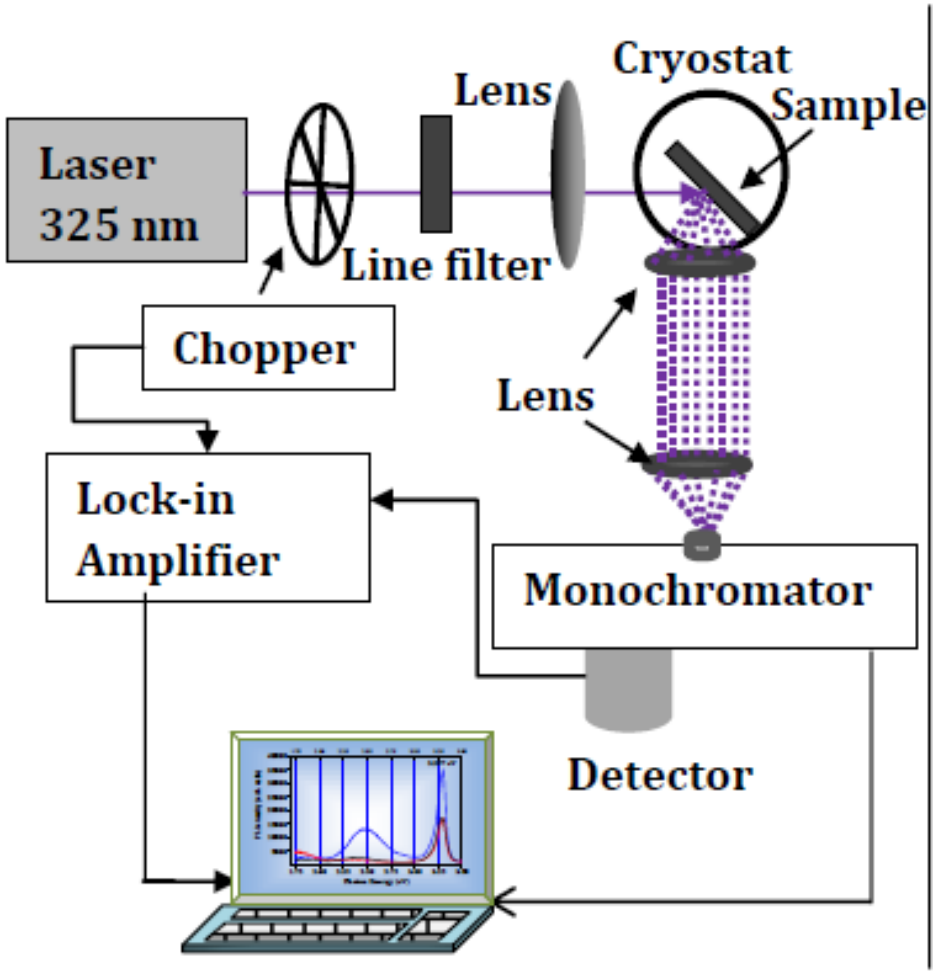

Figure 3.5: Schematic diagrams of typical experimental set-ups for CW-PL measurements using photomultiplier tubes or semiconductor photodiodes.

3.5.4 Electron Paramagnetic Resonance (EPR) spectroscopy

EPR is an effective tool to investigate the origin and nature of un-paired electrons in an atom. These un-paired electrons which are $10,000$ times lighter than atoms have their intrinsic spin contributing to some sort of magnetism. Incorporating transition metal i.e. Mn is believed to alter the electron spin (magnetism) of semiconducting materials hence called diluted magnetic semiconductors. The microwave absorption measurements were carried out using a JEOL electron paramagnetic resonance (EPR) spectrometer operating at 9.4 GHz (x-band) at room temperature ($298K$). The samples were mounted in the cavity centre at a position where the microwave magnetic field is maximum. The DC static field HDC

was slowly swept between 0 and 500 mT. The microwave power was kept at 5 mW to avoid saturation. The DC field was modulated with a superposed ac field whose amplitude was varied between 1 mT and 6 mT at 100 kHz frequency. The microwave response was measured as a derivative of microwave absorption signal. In this study, the origin of ferromagnetism in Al doped ZnO has been investigated using EPR measurements.

Chapter 4

Enhancing absorption in coated semiconductor nanowire/nanorod core-shell arrays using active host matrices

4.1 Introduction

One-dimensional nanostructures often exhibit fascinating physical properties that are not observed in their bulk counterparts [60, 61, 62, 63]. Nanowire/nanorods photovoltaics (PV) has been the subject of research with a view to enhancing the energy conversion efficiency and reducing the material and fabrication costs compared with bulk and thin-film PV [64]. Core-shell nanowire/nanorod arrays are both an ideal platform for fundamental interfacial studies as well as a promising geometry for high and efficient optical absorption [65]. This occurs because of the core-shell geometry which increases the number of nearly degenerate resonances by largely removing the polarization dependence of $1D$ nanowires [66].

Interaction of light with nanocomposites exhibit novel optical phenomena which unrivalled optical properties of these materials. Since the optical properties of heterogeneous metal-semiconductor(core-shell) composites can be efficiently tailored by surface plasmon resonance(SPR), they are strongly dependent on the nanoparticles size, shape, concentration(filling factor) or spatial distribution and surrounding matrix [67]. Control over these parameters enables such composite

core-shell to become promising media for development of novel non-linear materials, nanodevices and optical elements. Recent studies by Oener et al. [68] shows that the utilization of metal-semiconductor core-shell nanospheres or nanorods for plasmon mediated charge carrier dynamics for photovoltaics and photocatalysis. Other group, S. A. Mann et al., [69] reported that core-shell geometry efficiently couples light normally reflected and scattered by the metal core into photonic resonances in the shell eliminating the so-called shadowing losses by embedding metal nanowires in an ultrathin semiconducting shell. The group used Finite-difference time-domain(FDTD) simulation to confirm that placing core-shell nanowires on low-index substrates like glass or plastic only leads to minor perturbations, primarily by increasing the radiative loss rate in the cavity and thus requiring a different shell thickness to maintain critically coupled resonances. This hybrid core-shell geometry makes semiconductor nanowire/nanorods, an emerging and powerful class of materials for showing optimal absorption efficiency due to their unique electronic, optical, and chemical properties [70]. Among other fascinating applications, nanowire/nanorod core-shell are perhaps the most prospective materials for nanoscale sensors, light emitting diodes, solar cells, and so forth [71, 72].

The core-shell geometry of nanowire/nanorod is thought to be able to enhance the efficiency of charge collection by shortening the paths traveled by minority carriers [73, 74]. Specifically, ZnO/ZnS core-shell nanorod heterostructures have attracted a great amount of theoretical and experimental interests because of the typical type II band gap alignment that is of high benefit for the amelioration of photovoltaic and photocatalytic properties in comparison with the individual counterparts. Strong light confinement in nanowire/nanorods structures has enabled advances in diverse photonic applications from nanolasers to photovoltaic devices [75, 76, 77, 78].

Considering available technologies, the use of cylindrical core-shell arrays structures is better suited for many optics and optoelectronics applications reported so

far in Refs.[79, 80, 81, 81, 83, 84]. Compared to spherical models, to understand the energy balance between absorption and scattering processes cylindrical model is very efficient, for instance in this kinds of structures, the scattering of light is increased by three orders of magnitude[85]. Despite the fact that earlier studies[86] discussed the benefit of core-shell nanorod/nanowire arrays, the contribution of amplifying host matrices for optimal absorption was not explored.

In this work, the effect of active elements in composites having core-shell nanowire/nanorod arrays were investigated theoretically and experimentally. Indeed the theoretical calculations are compared with experimental work done on the growth of ZnO/ZnS nanorod core-shell arrays.

4.2 Theoretical consideration

4.2.1 Background

The concept of an effective permittivity is useful to describe the optical response of a metamaterial molded into arbitrary shapes, rather than having to deal with the detailed arrangement of particles. Theoretically, the permittivity and refractive index have been calculated from polarizability of the core-shell arrays by considering the wavelength outside cylindrical core-shell composite, which is larger compared to cylindrical diameters. Metal/Semiconductor composite core-shell at the resonant frequencies, close to the plasma frequency of the coated shell, show strong anomalous dispersion even at comparatively small volume fractions of the inclusions and a very high level of losses. The losses in the composites can be considerably reduced by introducing gain elements into the host matrix of the composites or by using alternative layers of composite and gaining medium. Literature reports that an array of nanowire/nanorods can exhibit superb absorptivity even at a fairly sparse arrangement [87, 88, 89], therefore to explain these properties the rigorous solution of the Maxwell equations is imperative.

Formally, the effect of active elements in composites can be described by introducing a negative part in the dielectric function of the host matrix [90, 91, 92, 93].

For instance metamaterials can be synthesized by embedding artificially fabricated inclusions in a specified host medium or on a host surface, this provides the designer with a large collections of independent parameters(or degrees of freedom), such as the properties of host materials, the size, shape, and composition of the inclusions [94]. By depositing a layer of shell on the nanowires to fabricate core/shell nanowires, the surface states of the core will be modified [95, 96, 97, 98], the band gap of the core material can be tailored, and as a result, the properties including photoluminescence(PL) of the core will be improved.

4.2.2 Electrodynamic analysis

To gain greater insight into how the shape and array of the core-shell nanorod/nanowire distribution influences the effective dielectric response, the discussion starts with presenting core-shell nanowire as cylindrical geometry for theoretical discussion and nanorod for experimental comparison.

Let us consider core-shell cylindrical nanowire/nanorod with radius r_c coated by metallic nanoshell of radius r_s centered at the origin and extending along the z-axis to infinity, embedded in a homogeneous dielectric environment(host medium) with permittivity ε_h where, $r_c < r_s$ (see Fig. 4.1). The nanowire/nanorod is illuminated by a uniform, quasi-static electric field, $E = E_0 e^{i(kx-\omega t)}$ where k is the complex wave vector given by $k = \frac{n\omega}{c}$ and has form $k = k' + k''$, [99]. In the model retardation effect is neglected and only dipolar interaction is under consideration: diameter of the nanowire/nanorod is much smaller than the wavelength of the excitation field. The incident electric field is assumed not to vary spatially over the dimensions of the nanowire while maintaining its time dependence.

The dielectric functions (DFs) of the core, shell, and host matrix are denoted as ε_c, ε_s, and ε_h respectively. The distribution of the potential in a cylindrical core-shell arrays embedded in a dielectric host matrix in an external constant electric field, can be written as:

$$\phi_h = -E_h(r - \frac{D_n}{r^{n-1}})\cos\theta, r \geq r_2. \tag{4.2.1}$$

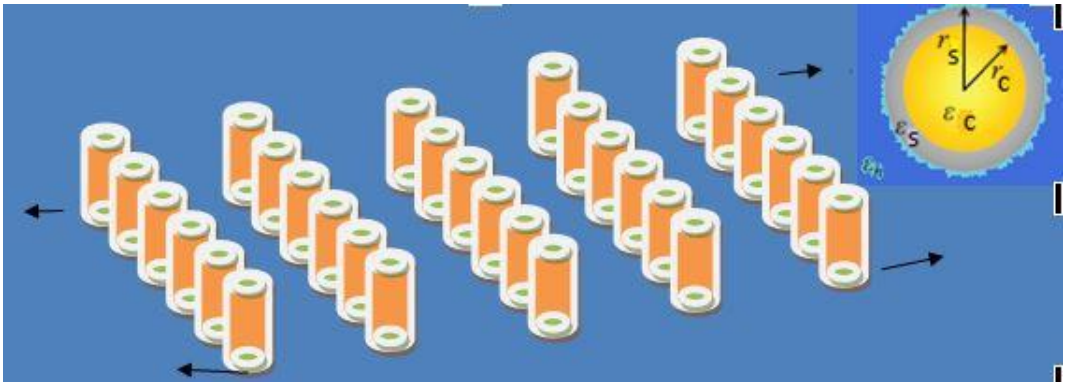

Figure 4.1: Structural model for cylindrical core-shell nanowire under consideration together with the relevant parameters.

.

where, E_h is the applied field, perpendicular to the axis of the nanorod/nanowire), the local field in these arrays can be considerably enhanced if a frequency of the incident radiation is close to the surface plasmon frequency. The local field E in the semiconductor core of the inclusion can be obtained with the help of the relation $E = AE_h$ where A is an enhancement factor discussed in Ref.[92, 93]. Here n is the dimension of the problem: $n = 3$ for the spherical(quantum dot) and $n = 2$ for the cylindrical inclusion(nanorod/nanowire, respectively

$$D = \beta r_c^2, \beta = 1 - 2\frac{\delta}{\Delta} \tag{4.2.2}$$

where Δ is given by

$$\Delta = \varepsilon_c^2 + q\varepsilon_c + \epsilon_s\varepsilon_h, \delta = \varepsilon_h[(\frac{2}{p} - 1)\varepsilon_c + \varepsilon_d] \tag{4.2.3}$$

$p = 1 - (r_c/r_s)^2$ is the metal fraction of cylindrical core-shell nanowire/nanorod.

$$q = (\frac{2}{p} - 1)\varepsilon_d + (\frac{2}{p} - 1)\varepsilon_h \tag{4.2.4}$$

where the dielectric permittivity of metallic shell has Drude form;

$$\varepsilon_s = \varepsilon_s' + i\varepsilon_s'' \tag{4.2.5}$$

$$\varepsilon_s' = \varepsilon_\infty - \frac{1}{z^2 + \gamma^2}, \quad \varepsilon_s'' = \frac{\gamma}{z(z^2 + \gamma^2)} \tag{4.2.6}$$

Considering $z = \frac{\omega}{\omega_p}$ and $\gamma = \frac{\nu}{\omega_p}$ (ω is the frequency of the incident radiation, ω_p is the plasma frequency of the metal part, and ν is the electron collision frequency).

In the model the dielectric permittivity of the host medium is given by

$$\varepsilon_h = \varepsilon'_h + i\varepsilon''_h \tag{4.2.7}$$

in this case we consider $\varepsilon'_h = 2.25$, $\varepsilon''_h = 0$ for passive host matrices and $\varepsilon'_h = 2.25$ (glass matrix), $\varepsilon''_h = -0.13866$,(polymers) for active host matrices, and for semiconductor core ε_c has real value, $\varepsilon_c = 9$, through out the paper for numerical purposes. As a result of the dielectric permittivity of the shell and the host medium(real and imaginary values), the polarizability takes complex form.

$$\beta = \beta' + i\beta'' \tag{4.2.8}$$

$$\beta' = 1 - 2\frac{\delta'\Delta' + \delta''\Delta''}{\Delta'^2 + \Delta''^2}, \beta'' = 2\frac{\delta'\Delta'' - \delta''\Delta'}{\Delta'^2 + \Delta''^2} \tag{4.2.9}$$

where

$$\delta' = (\frac{2}{p} - 1)[\varepsilon'_s\varepsilon'_h - \varepsilon''_s\varepsilon''_h] + \varepsilon_c\varepsilon'_h \tag{4.2.10}$$

$$\delta'' = (\frac{2}{p} - 1)[\varepsilon'_s\varepsilon''_h + \varepsilon''_s\varepsilon'_h] + \varepsilon_c\varepsilon''_h \tag{4.2.11}$$

$$\Delta' = {\varepsilon'_s}^2 + q'\varepsilon'_s + \varepsilon_c\varepsilon'_h - {\varepsilon''_s}^2 - q''\varepsilon''_s \tag{4.2.12}$$

$$\Delta'' = (q' + 2\varepsilon'_s)\varepsilon''_s + \varepsilon_c\varepsilon''_h + q''\varepsilon'_s \tag{4.2.13}$$

$$q' = (\frac{2}{p} - 1)\varepsilon_c + (\frac{2}{p} - 1)\varepsilon'_h \tag{4.2.14}$$

$$q'' = (\frac{2}{p} - 1)\varepsilon''_h \tag{4.2.15}$$

The double prime variables stands for imaginary part of the function.

Effective medium theory and Clausius-Mossoti equation for a composite with cylindrical nanowire/nanorod core-shell has the form [84]: $\frac{\epsilon_{eff}-\epsilon_h}{\epsilon_{eff}+\epsilon_h} = \frac{ND}{2}$. Where N is a density number of the nanowire/nanorod in the host medium and D is effective polarizabilty of the cylindrical nanowires. Maxwell Garnett mixing formula for the cylindrical nanowire of our study interest is given by ε_{eff}=$\varepsilon_h(1 + \frac{2f\beta}{1-f\beta})$ where β is the polarizability of the nanowire and f is the volume fraction of the nanowire given by f=$\frac{4\Pi}{3}r_s^3N$. For non magnetic medium $\mu = \mu_0$ index of refraction R can be

expressed in terms of the effective dielectric constant as $n^2 = \varepsilon_{eff}$. Therefore, it is possible to determine the refractive index of the composite from the above expression as $n^2 = \varepsilon_h(1 + \frac{2f\beta}{1-f\beta})$. Since quantities like ε_h, ε_s and β are complex it is important to express n^2 in terms of imaginary and real parts as:

$$n^2 = (\epsilon'_h + i\epsilon''_h)[1 + 2f\frac{\beta' + i\beta''}{(1 - f\beta') - if\beta''}] \tag{4.2.16}$$

$$= (\epsilon'_h + i\epsilon''_h)[1 + \frac{2f\beta' - 2f^2(\beta'^2 + i\beta''^2) + 2if\beta''}{\Delta_f}] \tag{4.2.17}$$

$$= (\epsilon'_h + i\epsilon''_h)[1 + \frac{2f\beta' - 2f^2|\beta|^2 + 2if\beta''}{\Delta_f}] \tag{4.2.18}$$

this expression can be written as real

$$b_r = \epsilon'_h + 2f[\frac{(\beta' - 2f|\beta|^2)\epsilon'_h - \beta''\epsilon''_h}{\Delta_f}] \tag{4.2.19}$$

and imaginary

$$b_I = \epsilon''_h + 2f[\frac{(\beta' - 2f|\beta|^2)\epsilon''_h + \beta''\epsilon'_h}{\Delta_f}] \tag{4.2.20}$$

where

$$\Delta_f = 1 - f\beta' + f^2|\beta|^2 \tag{4.2.21}$$

n^2 can be re-written as $n^2 = b_r + ib_I$, and equivalent to $n = n' + in''$.

$$n'^2 = \frac{1}{2}(\sqrt{b_r^2 + b_I^2} + b_r) \tag{4.2.22}$$

$$n''^2 = \frac{1}{2}(\sqrt{b_r^2 + b_I^2} - b_r) \tag{4.2.23}$$

The cylindrical assumed particles in the composites are polarizable, with light-induced dipoles, where the dipole moments interact within uniform electric field given by: $E = E_0 e^{i(k'x-\omega t)}\ e^{-k''x}$, and the term $e^{-k''x}$ implies that the wave decays as it propagates in the nanowire/nanorod core-shell arrays. Taking into account the relation, i.e: $I \sim E^2$ and combined with Lambert-Beer law $I = I_0 e^{-\alpha_{abs}x}$, where α_{abs} is the absorption coefficient. The enhanced absorptance was attributed to a field concentration (waveguiding) in the nanowire as presented in Refs.[104, 105]. Hence, the absorption coefficient can be written as:

$$\alpha_{abs} = 2k'' = \frac{2n''\omega}{c} \tag{4.2.24}$$

In our case it can be written as

$$\alpha_{abs} = \frac{2n'' z_r \omega_p}{c} \tag{4.2.25}$$

where $z_r = z$. The typical length of light propagation(absorption length) l, absorbance($A(\lambda)$), transmittance $T(\lambda)$ were calculated. We noticed that for the coated cylindrical core-shell nanowire/nanorod, absorption length can be found by the help of $l = \frac{1}{\alpha_{abs}}$. The expressions for Absorbance and $A(\lambda) = \frac{2tn'' z_r \omega_p}{c} = n'' t(\frac{2\Pi}{\lambda})$ where $t = r_s - r_c$ and transmittance; $T(\lambda) = -\log A(\lambda)$ are used for numerical calculation.

4.3 Experimental details and Characterizations

The chemicals used in this study were purchased from Sigma Aldrich and used without any additional purification. The ZnO/ZnS core-shell nanorods were grown as follows: Initially ZnO nanorod arrays (rods are mostly not vertical, but rather quite random in orientation) were grown by a two-step chemical bath deposition process as described in Refs. [106, 107]. (100) silicon substrates were sequentially cleaned in acetone, ethanol and Milli-Q water (in an ultrasonic bath) and then finally blown dry using N_2. ZnO nanoparticles, of 5 nm in diameter, were seeded onto the pre-cleaned Si substrates via spin coating, using a solution of zinc acetate dihydrate dissolved in ethanol. Next, the seeded substrate was annealed at 300^oC in oxygen for 30 min. Following that, the annealed seeded substrate was immersed in a chemical bath for the growth of ZnO nanorods. Sulphidation is a two-step process as well and is described next. ZnS coated ZnO nanorods were prepared via a self-assembling route described in Refs.[108], using a solution based chemical reaction. Firstly ZnO nanorod arrays was immersed in a 160 $mmol$ Na_2S solution for 90 min at 75^0C. Upon removal, the sample was rinsed in Milli-Q water and dried in N_2. During the second step, a 160 $mmol$ zinc nitrate hexahydrate solution was prepared and heated up to 75^0C within an oil bath. Once the temperature was stabilized at 75^0C, secondly it was dipped vertically into this solution for another 90 min. The sample was finally rinsed in Milli-Q water and dried in nitrogen gas.

Surface morphological analysis of the products was carried out and analyzed using a JEOL JSM $7100F$ scanning electron microscope (SEM), operated at $5kV$. The crystalline structure and faces of the rods was analyzed using an X-ray powder diffractometer, using a CuKa line (0.154 nm). PL spectra were collected between $89K$ and room temperature with a Mini-PL UV laser system 5.0 (Photon system, USA) which employ a NeCu laser with excitation wavelength of 248.6 nm were used for characterizing.

4.4 Results and discussion

4.4.1 Theoretical analysis

In order to understand the origin of the lasing in active host medium we consider homogeneous cylindrical core-shell nanowire/nanorod arrays embedded in active host medium. It is known that the local field in these composite can be considerably enhanced if a frequency of the incident external radiation field is close to the surface plasmon frequency [109, 110, 111, 112, 113]. Therefore, at intense incident electromagnetic fields (laser radiation), it is necessary to consider the effect of dielectric functions of the core, the shell and host material. From theoretical point of view, we choose two conditions from the dispersion relation; ($\varepsilon_h'' = 2.25$) (glass matrix) and ($\varepsilon_h'' < 0$)(polymers), under which such a medium can demonstrate very low loss or even gain leading to lasing in the composite(core-shell). It is demonstrated that with $p = 0.9$ in passive host matrix, $n'' = 0.025$ at the resonant frequency $z_r = 0.4$ and $\omega_p = 1.6 \times 10^{16}$ it is shown that $\alpha_{abs} = 1.07 \times 10^4 cm^{-1}$, the typical length of light propagation in the nanowire can be $l = 9.4 \times 10^{-5} cm$. However for pure metal cylindrical nanowire (without core) of nanowire $p = 1$ in passive host matrix, $n'' = 0.033$ at the resonant frequency $z_r = 0.385$, we get that $\alpha_{abs} = 1.4 \times 10^4 cm^{-1}$ and the typical length of light propagation in the nanowire(absorption length) can be $l = 7.14 \times 10^{-5} cm$. According to this obtained results in passive host matrix their is strong absorption. In order to create condition for considerable propagation of light in the nanowire arrays, it is necessary to

decrease n'' which can be done by introducing a negative values dielectric function of the host matrix $\epsilon_h'' < 0$. The host matrix with negative $\epsilon_h'' < 0$ amplify the incident electromagnetic wave rather than absorbing, [114, 115, 116, 117]. For cylindrical core-shell nanowire/nanorod with tuned inclusions(active host matrix) with metal fraction $p = 0.9$ ($\varepsilon_h'' = -0.13866$), and $n'' = 0.045$ at the resonant frequency $z_r = 0.4$ the numerical result gives $\alpha_{abs} = 1.92 \times 10^6 cm^{-1}$ and $l = 5.2 \times 10^{-3} cm$ which suggests the enhanced absorption is greater than the expected Lambert-Beer Law if we introduce negative value for dielectric function of active host medium.

From a Febry-Perot resonator [118, 141] the on-resonance condition can be shown as, $m\lambda = 2nL$, where λ is the on-resonance wavelength, n is the effective refractive index, L is the length, of the optical path and m is the mode number. This phenomenon is systematically related to PL emission intensity for experimental comparison [119, 120, 121]. We observe a strong blue-shift of the resonance as the p value increased from 0.4 to 0.9 (see Fig. 4.2) this is due to the fact that, the field nature is highly dipolar results in good light coupling between the interfaces(the shell and host medium). The dipolar resonance is shifted to the red as the shell(ZnS) thickness is increased compared with bare ZnO as depicted in the experimental section. A resonance shift $\Delta\lambda$ due to the change of refractive index Δn can be expressed by $\frac{\Delta\lambda}{\lambda} = \frac{\Delta n}{n}$. A typical wave length corresponding to the resonant frequency (z_r)= $0.323\omega_p$ for metallic shell of diameter $30nm$ with $p = 0.9$ is about $400nm$. By using the same condition of (z_r) and λ values: $(0.35\omega_p,\ 369.6nm)$, $(0.2\omega_p,\ 589.04nm)$, $(0.45\omega_p,\ 384.04nm)$, we find that the resonance is shifted to the red(Fig. 4.10).

It is known that in the absence of laser generation in the limit of weak fields, the active composite(below the laser generation threshold)can be described by Maxwell equations [60, 122, 123]. It allows us to use α obtained with the help of the long wave approximation. It is shown that in Fig. 4.2 the local field in the

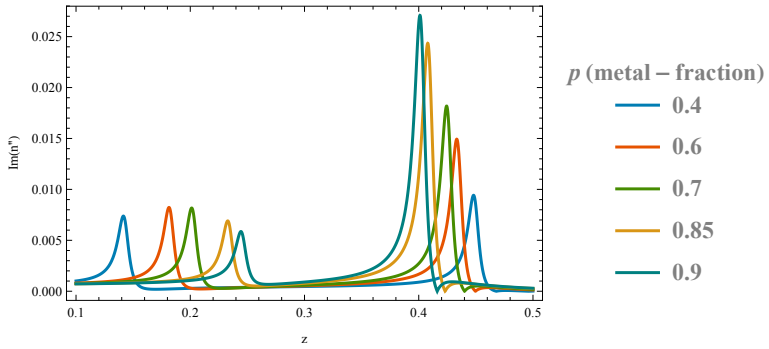

Figure 4.2: Imaginary part of refractive index n'' versus z for active host matrices and the numerical values and parameters are $\epsilon_h'' = 0$, $f = 0.001$, $\varepsilon_h' = 2.25$

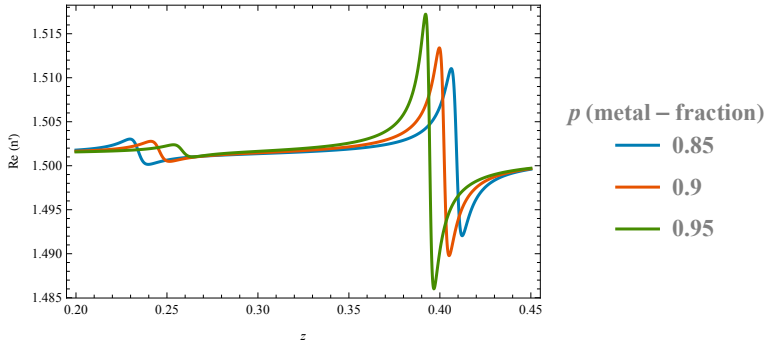

Figure 4.3: Real part of refractive index n' versus dimensionless frequency z with tuned cylindrical nanowire embedded in active host matrices with parameters $\epsilon_h'' = -0.13866$, $\varepsilon_h' = 2.25$

composite core-shell has two maxima which is blue shifted as volume fraction(p) increases suggesting the enhancement of local electric field in the core-shell. It appears that the optical absorption and refractive index change as a function of the photon energy for various shell thickness. The value of p is chosen from simulation(Wolfram Mathematica 9), the resonance using different value of p where the second maximum is enhanced. Unfortunately, for very small γ and arbitrary p the situation can be traced only numerically. The positions and values of the maxima strongly depend on p (at fixed rest parameters). For example, for $p < 0.4$; the second maximum is lower than the first one and very small. It is clear that the nonlinear part of the dielectric function(DF) of the host medium is important only if the electric fields are comparable with the inner atomic fields [124, 125, 126]. At present, such fields may be achieved in laser radiation. Another interesting property of a pure metal shell and metal-shell on semiconductor core is the abnormal

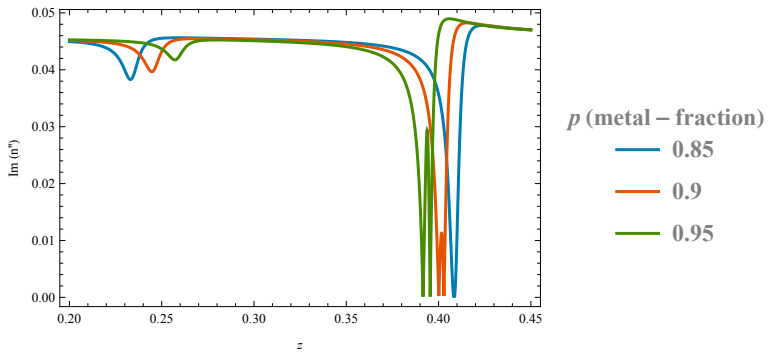

Figure 4.4: Imaginary part of refractive index n'' versus dimensionless frequency z with tuned cylindrical nanowire embedded in active host matrices with parameters $\epsilon_h'' = -0.13866$, $\varepsilon_h' = 2.25$

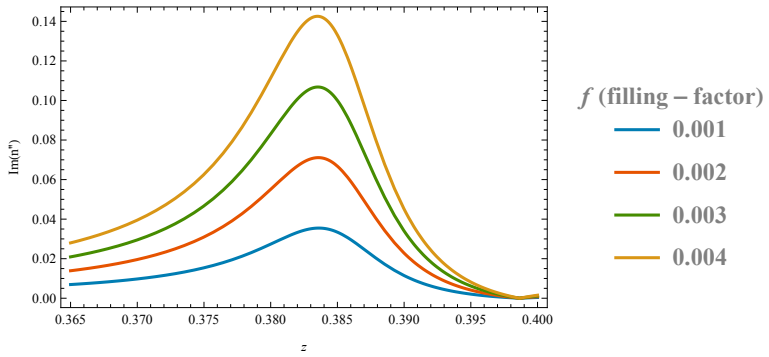

Figure 4.5: Imaginary part of refractive index n'' versus frequency z for pure metal cylindrical nanowire in passive host medium $\varepsilon_h'' = 0.0$.

enhancement of the local field, when the frequency of the incident electromagnetic wave approaches the surface plasmon frequency of the metal shell [97, 98, 99].

For $p > 0.4$, it becomes more important with further increment in p both maxima becoming higher and closer moving to higher frequencies. It would be relevant to note that the resonant frequencies are related with the plasma vibrations of the metal shell and the two interfaces, i.e,semiconductor(core)- metal(shell) and metal(shell)-host matrix. Basically, the restrictions on p imply the existence of the plasma vibrations(p is not very small) as well as the macroscopic properties of the semiconductor core(p is not very close to unit)[127]. Fig. 4.3 shows the n' real value of refractive index of the core-shell versus the dimensionless frequency z, which have been calculated with the help of Eq. 4.2.22 and Eq. 4.2.23. In this case the value of the volume fraction determines the change of refractive index, as one changes position from core center to the shell the threshold energy would be

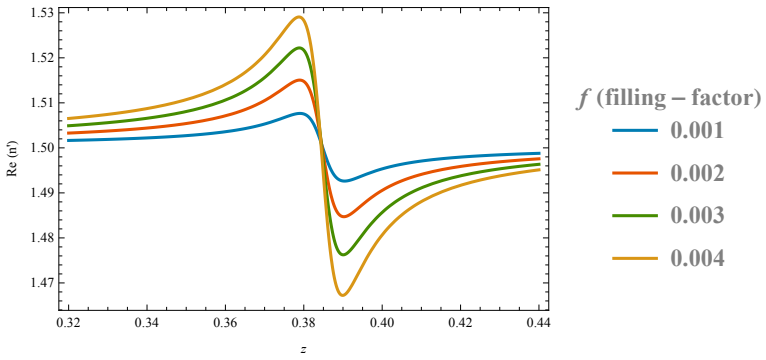

Figure 4.6: Real part of refractive index n' versus frequency z, for pure metal cylindrical nanowire embedded in passive host(non-absorbing host medium) $\varepsilon_h'' = 0.0$.

redly shifted. Similar red shift phenomenon has also been observed in the most cases studied when the impurity(doping) is displaced from the core-center to the shell-center discussed in Refs.[128, 129].

The main characteristic of the nanorod core-shell array under consideration is a strong absorption of light at resonant frequencies. The absorption coefficient of the composites can be evaluated with the help of Eq. 4.2.25. Further decrease in (ε_h'')results in the appearance of the fork like structure of the right minimum of n''. The same effect can be obtained by increasing the volume fraction f by keeping $(\varepsilon_h'' < 0)$ constant as shown in Fig. 4.3 and Fig. 4.4. It is worth noting that obtaining the minima of n'' for both types of the core-shell embedded in active and passive matrices require fine tuning of $(\varepsilon_h'' < 0)$ as the dipolar resonance residing at the core-shell interface, is more sensitive to the host environment [60, 130, 131, 132]. Anantha et. al. [103] recently reports negative losses are important to design a 'fiber-optic bundle' that consists of a multilayer stack of alternating thin layers of lossy metal(silver) and an amplifying positive dielectric medium (an optically pumped semiconductor, for example) to transfer images with good subwavelength resolution across large stack thicknesses (of the order of a few wavelengths) [111]. For example, to exactly counter the effects of absorption in the negative medium one can use semiconductor laser material such as GaN or AlGaAs for the positive medium and silver for the negative medium. Using blue/ultra-violet light to pump

the AlGaAs, one can make the AlGaAs now optically amplifying in the red region of the spectrum, where one can satisfy the perfect-lens condition for the real parts of the dielectric constant. By adjusting the pump laser intensity, the imaginary part of the positive gain medium can be tuned [150].

Fig. 4.5 depicts when filling factor(f) is increased the intensity of refractive index is highly enhanced suggesting the shell thickness and the density of the packed nanorod arrays can play great role to improve the photoluminescence and similar results are discussed for the nanowire antenna emission in ref. [149], in the present work it can be confirmed with the help of Fig. 4.10, when the core is coated the emission (PL) intensity increases and very broad. However, the same quantities of the passive composite with pure metal shell obtained using Eq. 4.2.22 shows the real part of refractive index(see Fig. 4.6 6) versus frequency showing asymmetric profile enhancement as the value of f increases suggesting f increases with continues coating. The absolute values of the maxima and minima of n' in active host matrices at the gain levels considered here practically do not change compared to those of passive host matrices which is in agreement with results reported in Ref. [133, 134]. We note that in our structural model of ZnO/ZnS core-shell nanowire, the strain effect can reduces the energy of the transition between the core-shell which may provide a degree of freedom for band gap engineering in heterostructure materials. Similarly findings suggested the strain can be used to reduce the total system band gap in ZnO/ZnTe core-shell nanowires and strain induced band gap in Si are discussed [102]. Moreover, the proposed theoretical model derived via polarization in an external electric field may be valuable in controlling and designing highly absorbing electrostatic resonance and emission from nanorod/nanowire arrays particularly for hybrid PV application. In light of the present model we suggest cylindrical core-shell could be the optimal geometrical configuration in order to enhance optical absorptance. Experimentalists may be benefited from such theoretical model, for instance how thickness of the shell,

filling factor or arrays (densely packed nanowires) and their geometrical configuration can affect absorption particularly in heterostructures comprised materials for PV application.

4.4.2 Experimental analysis

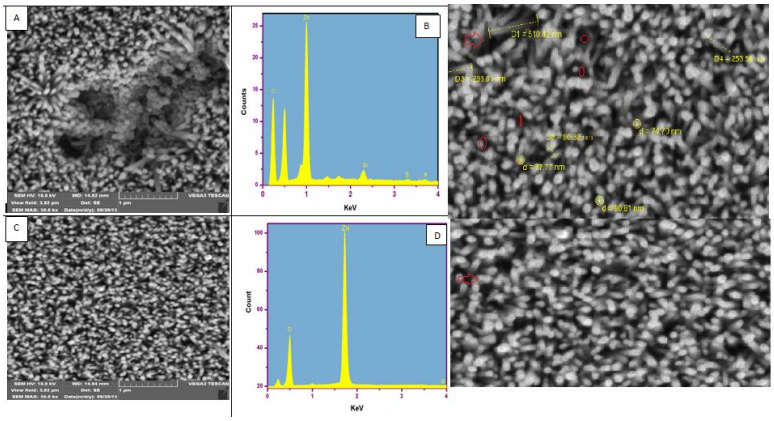

Figure 4.7: SEM micrograph and EDX patterns of ZnS/ZnO core-shell. (a). SEM image *A* shows after sulphidation of ZnO/ZnS core-shell and image *B* is the EDX pattern recorded from A. (b). Image *C* shows the SEM before sulphidation(ZnO nanorod) and image *B* shows the EDX pattern recorded from C.

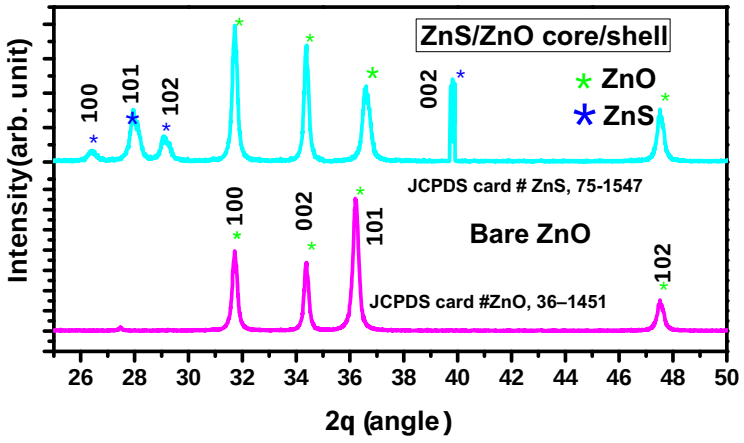

Figure 4.8: XRD patterns of bare ZnO and ZnS/ZnO core-shell).

Fig. 4.7 (A) depicts the plane-view of SEM image of nanorod core-shell arrays after sulphidation in 160 mmol Na_2S solution at 75 for a period of 90 min. It is evident that ZnS decorated across the ZnO nanorods with less defined side is clearly visible. Fig. 4.7 (C) shows the plane-view of ZnO nanorods grown on Si

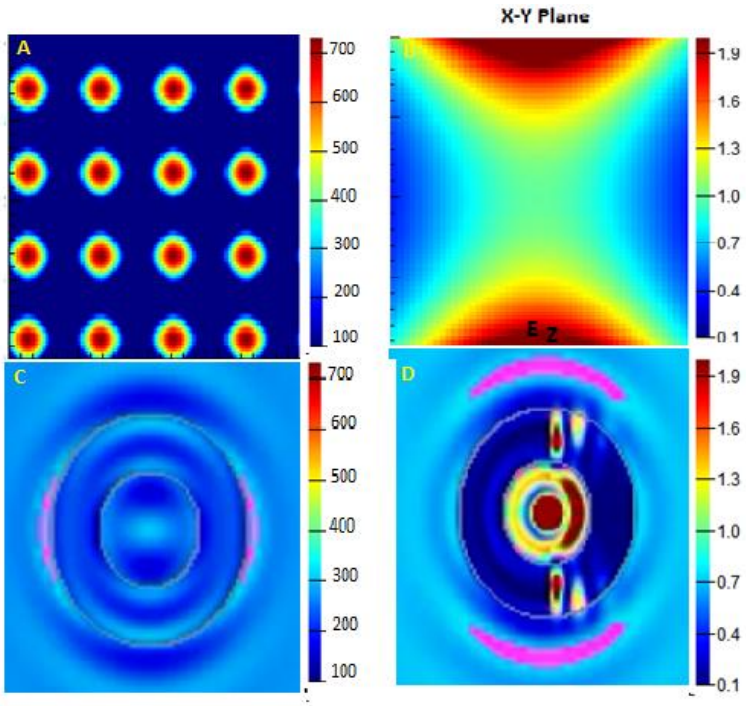

Figure 4.9: Two-dimensional plots of the modulus of the local electric field of core-shell structures. The color bar indicates the normal scale in V m^{-1} unit. (a) Resonant state of array of inclusions in the matrix. (b) Field patterns for E_z in the x-y plane (one unit cell) for single rod. (c) Resonant state of single inclusion in the unit cell. (d) Off-resonant state of single inclusion in the matrix

.

substrate before sulphidation experienced as core-shell and the nanorods are random, dense and not well aligned. The EDX results were predominantly used as a qualitative assessment tool as in Fig. 4.7 (B) clearly demonstrates that the EDX spectra recorded from sample 4.7 (A) has sulfur after sulphidation together with oxygen and zinc. The presence of Si peak results from the substrate. However, the EDX spectra recorded from sample Fig. 4.7 (C)in Fig. 4.7 (D) confirms the presence of Zn, O and Si in the ZnO nanorods viewed. The composition of ZnS(shell) was further confirmed by XRD. Fig. 4.8 shows, the nanorod core-shell arrays were found to be composed of a single-crystalline ZnO core and ZnS shell via the presence of the (100), (101), (102), and (002) from 2θ angle for face centred cubic (fcc) ZnS(JCPDS Card No.$75-1547$). Fig. 4.9 shows corresponding local electric field in the core-shell structure. When subjected to a constant applied electric field, the local fields exhibit strong spatial fluctuations as shown for resonant and

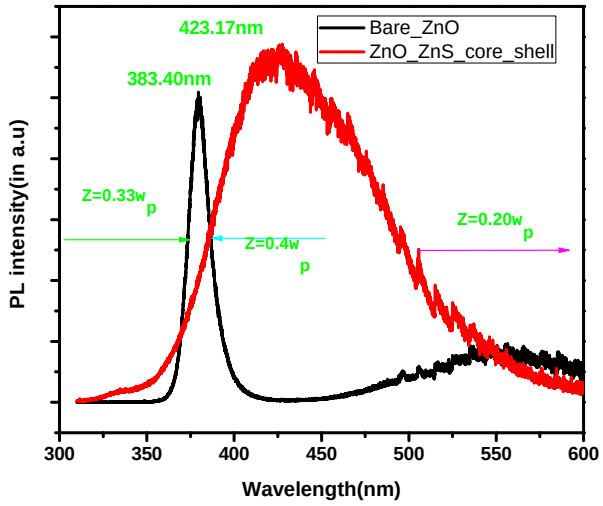

Figure 4.10: PL intensity vs wavelength emission observed from ZnS coated ZnO nanorod arrays for theoretical comparison.

off-resonant, even though the non uniform electric field distribution is apparent from these figures, the field inside the core is spatially uniform (see Figs. 9A and 9C). Light emission from core-shell nanowire/nanorod arrays can be tuned by, field resonant enhancement, dipole position and nanowires length [93, 94]. The spectrum of PL in Fig. 4.10 depicts the emission is visible in two distinct energy windows, which shows ZnO/ZnS core-shell spectrum is very broad and intense than the bare ZnO. Photoluminescence mediated by the semiconductor NW array is theoretically addressed by Paniagua et al. [135] and Joshua et al. [101] in the context of light-coupling into guided modes. In their report emission can be modified upon varying the dipole position along the NW length. Therefore, slight modification of the real and imaginary components of refractive index can affect qualitatively and quantitatively photoluminescence spectra. In the next section, similar calculations were extended to the 4×4 array of cylindrical core-shell inclusions using FDTD simulation. By comparison to the case of the single inclusion in the unit cell (Figs. 4.3 and 4.4), it is to be noted that the the real part and imaginary part of refractive index depends on the volume fraction of the core shell. Electric field enhancement can be substantial and pronounced, as illustrated in

Fig. 4.9 in the core-shell which seems in agreement with the proposed theoretical speculation when the the value of p get larger. It seems that the cylindrical core-shell inclusions have advantage to obtain the intrinsic resonance at lower volume fractions. Compared to the actual features observed for homogeneous inclusions for the same set of model parameters[108, 112], the imaginary parts are present if the materials are lossy. The shifts of the resonant position due to the coating effect and volume fraction are significant, in the explored range of f as depicted in Figs. 4.5 and 4.6. For instance, the resonant peak increased by 20 % in going from $f = 0.001$ to $f = 0.004$. ZnO/ZnS core-shell nanorod array was compared with the numerical calculations and the agreement was notable as shown in Fig. 4.10. The photoluminescence emission originated from the core-shell nanorod array could be the result of average dipole emission from all excited modes and polarization [136]. Negative values of ϵ_h'' can be achieved in composite media near resonances, which generally implies very dispersive properties showing the fact that metals or other materials with negative permittivity are required for the heterostructure to have localized resonance [137] The peaks observed around 3.23 eV (383.4) nm and 2.92 eV (423.17) nm are in good agreement with theoretical calculations in the range of volume fraction $p = 0.9$, $p = 0.85$ and $p = 0.95$, particularly $(0.35\omega_p,\ 369.6\ nm)$ as demonstrated in Fig. 4.10. Generally, one should always remember that no one of the mixing models could offer exact value for a certain volume fraction, because in random mixtures, all values between Wiener limits are possible. However, it is very probable that a mixture with a large number of inclusions is almost isotropic and therefore combination of mixing models and FDTD results seem to offer reasonable limits. This method finds tuning the volume of the constituents(f) in the core-shell inclusion and the dielectric properties, are useful to vary the operating frequency and wavelength over a large range to design new materials.

4.5 Conclusion

In this work, the optical properties of two-dimensional metal-semiconductor core-shell arrays embedded in amplifying host matrix has been studied theoretically. The condition of introducing negative value of dielectric function of the host matrices that is necessary to compensate the absorption in composite has been demonstrated by careful choice of numerical calculations. The presented theoretical model has been compared with experimental data. Continuous ZnS(shell), thick ($255nm$), and uniform coating was grown on ZnO nanorods using chemical synthesis process. This predominantly polycrystalline ZnS shell was grown at relatively low temperatures and with high growth rates by sulfidation. With an increase in shell thickness, filling factor(f) and volume fraction the contributions from both ZnO and ZnS were discussed. The study provides a good indication of tuning the UV emission of the ZnO-ZnS core-shell nanorod arrays by changing index of the substrate.

Moreover, this core-shell nanostructure can be used for the fabrication of well aligned hollow ZnS/ZnO core-shell nanorod arrays of desirable thickness on the surface of active host medium. Finally; our results clearly illustrate the introduction of active host medium is responsible for the optical absorption greater than the expected Lambert-Beer law. To explain similar phenomenon in core-shell nanowire, earlier studies used tuning the shape and geometry of nanowire/nanorod arrays, [91, 92, 93] the readers are referred to Refs. [71], for Ge InP, Si, and GaP nanowires, relevant for applications in solar cells [72, 73]. However our result suggest that the model is promising than previously reported techniques to achieve optimal absorption efficiency and designing arrays of core-shell nanorods and nanowires[76, 77].

Chapter 5

Rapid synthesis of blue emitting ZnO nanoparticles for fluorescent applications

5.1 Introduction

Semiconductor nanostructures are promising candidates for future electronic and photonic devices. Nanostructures based on wide bandgap semiconductors such as GaN and ZnO are of particular interest because of their applications in short wavelength light emitting devices and field emission devices [1, 2, 3, 4]. ZnO is a potential competitor of GaN for blue and UV emission and characterized by direct band gap of 3.37 eV at room temperature with large exciton binding energy of 60 meV compared to GaN (28 meV) [5, 6, 7].

In addition to the UV emission ZnO is also known to emit in the visible region [81]. The photoluminescence spectrum of ZnO is normally composed of two parts: excitonic near band edge emission with energy around the band gap of ZnO and defect related deep level emission in the visible range. ZnO is n-type semiconductor due to oxygen vacancies, impurities like Al, H and and interstitial Zn ions which act as donors in ZnO lattice. These native defects are believed to be responsible for visible photoluminescence. The UV emission is due to excitonic related recombination [12, 13]. The exact mechanism for deep level emission is still controversial although intrinsic defects such as oxygen vacancies, oxygen interstitial, zinc vacancies and extrinsic impurities are all considered as a possible origin [14, 15, 16]. However, understanding the origin of photoluminescence in

ZnO nanoparticles and improving the emission efficiency is still a major challenge.

Synthesis and characterization of zinc oxide (ZnO) nanoparticles has found widespread interest during past few years due to their unique electro optical properties, which can be employed in devices such as ultraviolet (UV) light-emitting diodes (LEDs) and blue luminescent devices [11].

Searching of new methodology to synthesize ZnO NPs with a uniform morphology, size and reproducibility is of great importance both for fundamental studies and practical application. In the past, several crystal-growth technology, have been explored, among which are sol-gel, spray pyrolysis, chemical-vapor transport, vapor-phase growth, chemical bath deposition (CBD), direct precipitation methods and hydrothermal growth which also had the additional motivation of doping with Li in an effort to obtain p-type material [1, 24, 25, 26]. However, these methods involve a strictly controlled synthesis environment, complicated procedures, high-temperature synthesis processes and expensive equipment. Despite extensive research over the past several years, some fundamental properties of the low-temperature photoluminescence in the ZnO synthesized by thermal decomposition are not fully understood and rarely reported.

In this paper, we therefore report on ZnO NPs that emit in the visible region without the requirement of additional doping. The temperature-dependent PL for samples of ZnO prepared at a temperature of 200 ^0C and 300 ^0C were discussed with their underlying mechanism. Moreover, the structural and optical properties of ZnO NPs synthesized via thermal decomposition method has been studied.

5.2 Experiment

5.2.1 Sample preparation

The zinc acetate dihydrate ($Zn(CH_3COOH)_2.2H_2O$) $>$ 99%, purity purchased from Sigma Aldrich, were used as precursor without further purification to prepare ZnO NPs. In order to determine possible decomposition temperature of zinc acetate dihydrate into ZnO NPs, samples were annealed at various temperature

for 2 hr. Four sets of 5 gm of Zn $(CH_3COOH)_2.2H_2O$ was put into sample holders, the crucible and annealed at a temperature of 200, 300, 400 and 500 ^0C for 2 hr in muffle furnace in air to produce the ZnO NPs.

5.2.2 Characterizations

The crystal structures of the samples were determined with a Bruker AXS D8 ADVANCE Discover diffractometer(XRD), with Cu Ka (1.5418) radiation. Surface morphologies and elemental compositions were studied using a scanning electron microscope(SEM) (Shimadzu model ZU SSX-550 Superscan) equipped with EDX. The optical absorption measurements were carried out in the $200 - 600$ nm wavelength range using a Perkin Elmer UV/Vis Lambda 20 powder Spectrophotometer. Luminescence measurements were done using a photoluminescent (PL) laser system 5.0 (Photon systems, USA), which uses a He-Cd laser with an excitation wavelength of 248.6 nm.

5.3 Results and discussion

5.3.1 Structural analysis

Fig. 5.1 shows the XRD pattern of ZnO NPs synthesized by thermal decomposition method for various annealing temperatures. XRD pattern of ZnO NPs exhibits various peaks which could be indexed according to ZnO diffraction peak (JCPDS card No. $36 - 1451$).

The presence of various diffraction peaks reveals hexagonal wurtzite phase of ZnO which suggests polycrystalline nature of ZnO. The diffraction peaks at scattering angle (2θ) of 31.74^0, 34.43^0, 36.25^0 and 47.5^0 belongs to 100, 002, 101 and 102 diffraction planes from ZnO, and the other peak marked with asterisks $*$ corresponds to zinc acetate. It can be clearly seen that by increasing the growth temperature from 200 ^0C to 500 ^0C ZnO peaks became prominent and prevailed. No other impurities are observed except for zinc acetate related peaks in the

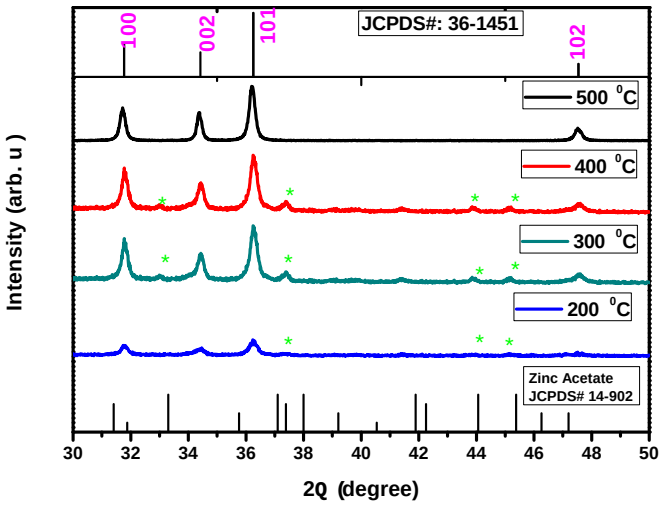

Figure 5.1: XRD pattern of ZnO nanoparticles synthesized at various temperatures for 2hr.

.

samples prepared at lower temperature, but fully decomposes for the higher temperature. The estimated lattice constants slightly increased as the decomposition temperature increased from 200 ^0C to 500 ^0C as summarized in Table 7.1. The increase of the lattice parameter of ZnO NPs with increase in temperature was calculated using the Eq. 5.3.1:

$$\frac{1}{d_{101}^2} = \frac{4}{3}(\frac{1}{a^2}) + \frac{1}{c^2} \tag{5.3.1}$$

where d is the interplanar distance, a and c are the lattice parameters.

Table 5.1: Measured properties of ZnO nanoparticles at various temperature

Temp. (^{0}C)	Particle diameter $R_0 \pm 0.5$ (nm)	Lattice parameter, a ($\mathring{A}$)	Lattice parameter, c ($\mathring{A}$)
200	16.3	3.245	5.299
300	17.8	3.247	5.302
400	19.6	3.249	5.305
500	19.7	3.250	5.307

Fig. 6.3 shows the variation of FWHM as measured from diffraction plane 101 and particle size of ZnO NPs synthesized at various decomposition temperatures

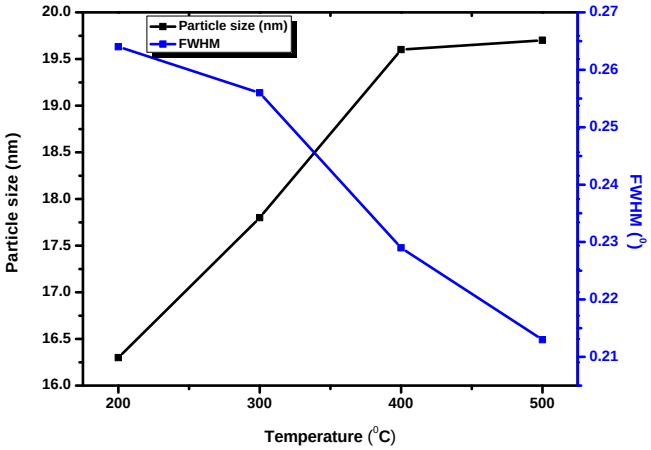

Figure 5.2: Variation of FWHM of (101) x-ray diffraction peaks and estimated particle sizes plotted against decomposition temperature.

for annealing time of 2 hr. The FWHM, which is an indication of the crystalline quality of the prepared ZnO NPs, decreases significantly as the decomposition temperature increases. Fig. 5.3 depicts variation of lattice parameter, a and c with increasing annealing temperature respectively confirming the increase in grain size at higher decomposition temperature.

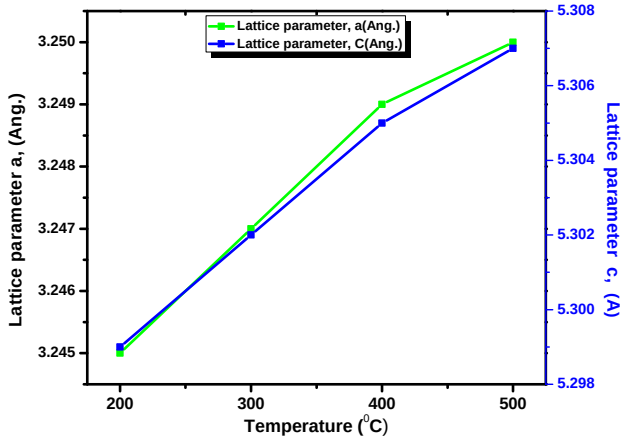

Figure 5.3: Variation of lattice parameter, a and c as a function of temperature.

.

The average crystallite size of prepared ZnO NPs can be estimated from the

FWHM of the 101 diffraction peak estimated using the Debye Scherrers Eq 5.3.2:

$$D = \frac{0.9\lambda}{\beta \cos\theta} \tag{5.3.2}$$

where D is the crystallite size, λ is the wavelength ($\lambda = 0.15402$ nm) of radiation used, θ is the Bragg angle and β is the full-width at half-maximum measured in degrees. The estimated average particle sizes were 16.3, 17.8, 19.6 and 19.7 nm corresponding to the 200, 300, 400 and 500 ^0C decomposition temperatures. The estimated particle sizes increases with annealing temperature and it has highest value at of 500 ^0C due to narrowing of the diffraction peak. According to Ostwald ripening the increase in the particle size is due to the merging of the smaller particles into larger ones as suggested by Nanda et al. [52] and is a result of potential energy difference between small and large particles and can occur through solid state diffusion. The intensity ratio, $\frac{I_{(002)}}{I_{(101)}}$ of the peaks presenting (002) and (101) at 500 ^OC is equal to 0.53 which is higher than the corresponding standard value of 0.44 of bulk hexagonal wurtzite ZnO [53] suggesting the prepared ZnO structure is preferred the (002) orientation.

5.3.2 Morphological analysis

Fig. 5.4(A, B, and C) illustrates the SEM images of ZnO NPs prepared at a temperature of 300, 400 and 500 ^0C respectively. The SEM images clearly indicate that the surface morphology of the ZnO NPs depending on the synthesis temperatures.

It is interesting to observe the formation of spherical ZnO NPs which is fully noted when the decomposition temperature was increased to 500 ^0C (see the inset in Fig. 5.4 C). It is observed that as decomposition temperature increases, the structural defects(dislocation) for the ZnO NPs prepared at a temperature of 200 ^0C reduces as compared to 500 ^0C causing uniform ZnO NPs which are purely spherical in shape. Fig. 5.4 (D, E and F) shows chemical stoichiometry of the ZnO nanoparticles prepared at a temperature of 300, 400 and 500 ^0C. The results presented shows that the prepared material contains C, O and Zn elements. The

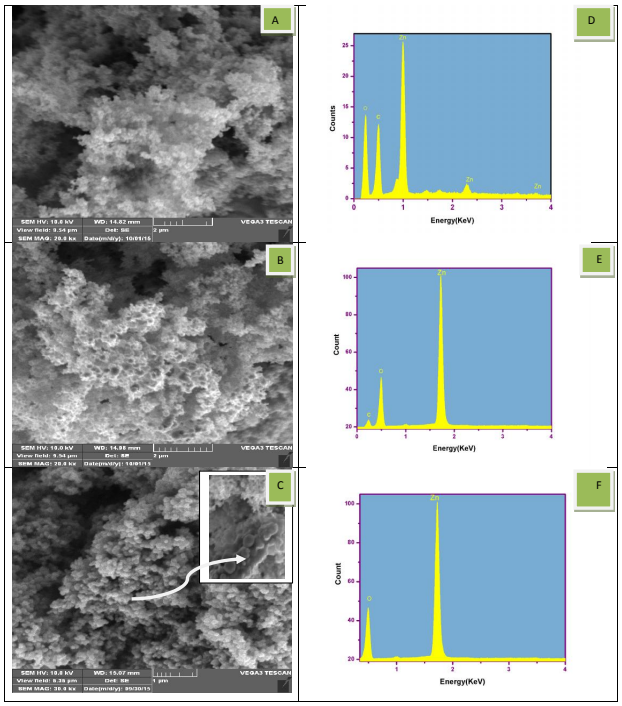

Figure 5.4: SEM micrograph and EDX spectrum of ZnO nanoparticles at: (A)300 ^0C. (B)400 ^0C. (C)500 ^0C for 2h, and D, E and F are the corresponding EDX spectra.

decrease in the C concentration with increasing synthesis temperature is suggested to be as a result of efficient evaporation of the acetate-group.

5.4 UV-visible spectrophotometer analysis

Fig. 5.5 shows room-temperature UV-visible absorption spectrum of ZnO nanoparticles synthesized for various decomposition temperatures. The prepared ZnO NPs have band edge absorption peaks at 362.2 nm, 389.4 nm, 429.72 nm and 455.32 nm for samples prepared at a temperature of 200, 300, 400 and 500 ^0C respectively. These absorption peaks conform to the well-known intrinsic band gap absorption of ZnO. The absorption edge around 389.4 nm was assigned to intrinsic band-gap absorption of ZnO due to the electron transitions from the the valence band

to the conduction band $O_{2p} \rightarrow Zn_{3d}$ [17] and the other possible explanation are given in terms of structural defects associated with Zn interstitial as reported in Refs. [53, 54]. It is observed from the spectra that the absorbance of the samples reduces slightly with increase in decomposition temperature and the absorption edge slightly shifts to lower energy [146, 147, 148, 149]. Furthermore this red shift indicated the shrinkage effect in the band gap energy as a function of temperature. They obtained ZnO which exhibited a high absorption band in the UV region ($\lambda < 380nm$).

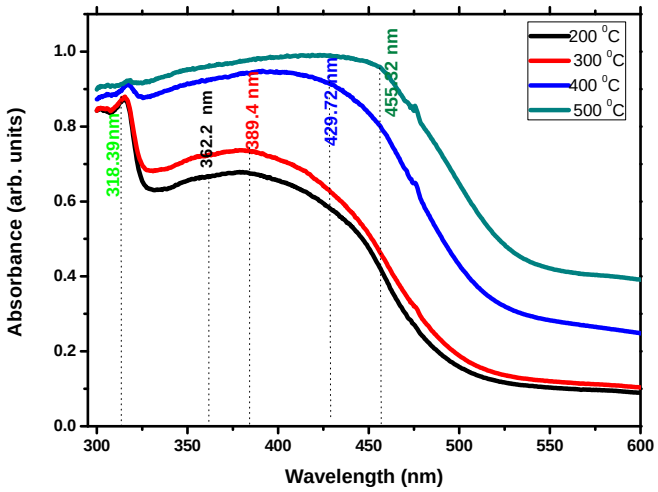

Figure 5.5: UV-Vis absorbance spectra of ZnO nanoparticles synthesized at different annealing temperatures.

Fig. 5.6 represents the relationship $(\alpha h\nu)^2$ versus the photon energy $(h\nu)$ from which the optical band gap of the nanoparticle was determined by extrapolating the linear part of the spectrum. The characteristic's change of the band gap with increase in size of the ZnO nanostructure has been studied by the observation of the red shift in photoluminescence peak position. Thus photoluminescence is useful for the study of quantum confinement of electrons. The direct bandgap energy of the synthesized ZnO nanoparticles was estimated using Tauc's plots relation [109]. ZnO nanoparticles synthesized have estimated band gap values of $3.28eV$, $3.29eV$, $3.33eV$ and $3.39eV$ for samples prepared at a temperature of 500,

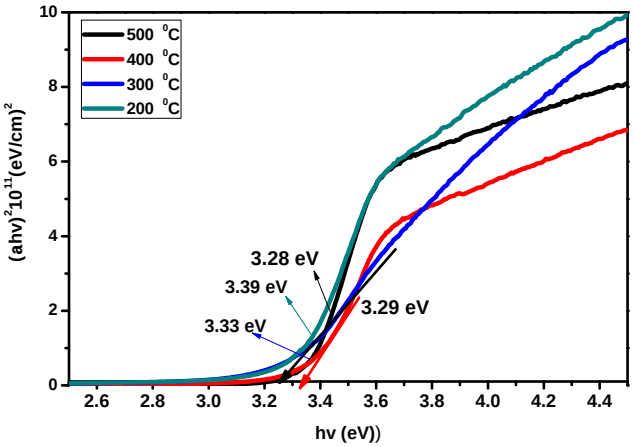

Figure 5.6: The optical absorption energy band gap estimated using Tauc's plot relation for ZnO nanoparticles synthesized at different annealing temperatures.

.

400, 300 and 200 ^0C respectively. Thus, the estimated band gap energy of the ZnO nanoparticles was found to decrease with the increase in the decomposition temperature and similar results were obtained by Kathalingam et al. [28]. It is clear that when the particle size increases, the electronic states are not discrete as a result the band gap energy reduces and the oscillator strength decreases [59, 60].

5.5 Photoluminescence analysis

Fig. 5.7 shows the PL spectra of ZnO NPs prepared at various annealing temperatures. In the PL spectrum, four emission bands, including band edge emission at 398.3 nm (3.11 eV), 402.8 nm (3.07 eV), 406.9 nm (3.04 eV) and 409.6 nm (3.02 eV) for ZnO prepared at a temperature of 500, 400, 300 and 200 ^0C respectively were observed. The visible emission in ZnO is due to different intrinsic defects such as oxygen vacancies (V_o), zinc vacancies (V_{Zn}), oxygen interstitials (O_i), zinc interstitials (Zn_i) and oxygen antisites (O_{Zn}) [32, 33]. Band edge emission centered at around 398.3 nm should be attributed to the recombination of excitons and V_{Zn} [34, 35]. However the origin of violet emissions centered at 3.07 eV(402.79 nm), 406.9 nm (3.04 eV) and 409.6 nm (3.02 eV) are ascribed to an electron transition from a shallow donor level of neutral Zn_i to the top level of the valence band

[44, 45, 46]. The broad deep level emission that started from UV to the visible region 360 -480 nm with the maximum peak at 409.64 nm for the sample prepared at 200 ^0C was observed. The decrease in PL intensity with increase in decomposition temperature can be attributed to formation of better ZnO stoichiometry and near surface band bending caused by surface impurities[47, 48, 49]. In samples of ZnO prepared at higher decomposition temperatures, the increase in grain size will reduce the relative contribution from recombination near the grains, resulting in strongly reduced violet emission. On the other hand, as the decomposition temperature increases more and more ZnO NPs with less deep defects form and as the result the transition line for the emission will decrease causing the the PL intensity to decrease [50] . The other possible explanation can be given as the existence of high dislocation density(defects) at the lower decomposition temperature. The dislocation density (δ) [123], which represents the amount of defects in the sample is defined as the length of dislocation lines per unit volume of the crystal and is calculated using the Eq.5.5.1:

$$\delta = \frac{1}{D^2} \tag{5.5.1}$$

where D is the crystallite size. Calculating the dislocation density (δ) of ZnO NPs synthesized at 200 ^0C and 500 ^0C using table 7.1 and Eq. 5.5.1 it has value of 25.76×10^{-4} $(nm)^{-2}$ and 37.63×10^{-4} $(nm)^{-2}$ respectively, suggesting high dislocation density at 200 ^0C and the lattice imperfection decrease with increase in particle size. Moreover, defect density decreases with synthesis temperature in the present study. For samples synthesized at low temperature, a number of lattice defects which can act as radiative recombination centers are suggested. The reduction of these defect related radiative centers after annealing at 500 ^0C in air is likely related to formation better stoichiometric ZnO NPs. This hypothesis can be supported by the fact that surface defects strongly depend on morphology(SEM), with suppression of the emission as discussed under PL section.

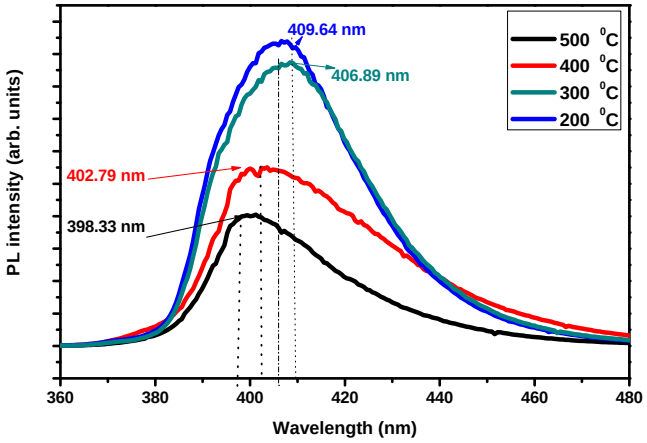

Figure 5.7: PL emission of ZnO nanoparticles synthesized at various temperatures.

5.6 Temperature dependent PL

Relative changes in state population with temperature provide evidence that PL peaks originate in the same part of the sample and that carriers are free to move between the available states. This feature can be useful because thermal quenching can hide sparse low-energy states and thermal broadening can obscure important details in the spectrum, low temperature PL experiments were conducted for samples prepared at 200 and 300 ^0C. Fig. 5.8 and 5.9 A, depicts the temperature dependent PL spectra of synthesized ZnO NPs prepared at 200 ^0C and 300 ^0C respectively studied at a temperature of 300 K, 273 K, 173 K, 123 K and 73 K. It is well known that the donor-acceptor pair transition energy decreases along with the band gap energy when the temperature is increased causing the PL intensity to decrease. The experimental data for the temperature dependence of PL band intensity can be fitted by the following expression [129]:

$$I(T) = \frac{I_0}{1 + Ae^{-\frac{E_a}{K_\beta T}}} \tag{5.6.1}$$

where I_o is the peak intensity at temperature $T = 0$ K, A is assumed to be constant, E_a is the activation energy of the thermal quenching process, and K_b is the Boltzmann's constant. Fig. 5.9 (B) is a plot of the integrated intensity of the 3.21 eV transition versus reciprocal temperature for the ZnO NPs prepared at

a temperature of 300 ^0C in the luminescence as one step quenching process and fitted by the Eq.5.6.1. The best fit, demonstrated by the solid curve has been achieved with parameters $I_0 = 1020$, $E_a = 12.9$ meV. A range of experimental values have been reported for the quenching of the dominant bound exciton for ZnO nanorods as 13.2 meV and 13.1 meV for bulk ZnO [13, 93].

Haynes' empirical rule E_a = a + b E_D can be used to calculate the donor binding energy E_D, using the value obtained for $E_a = 12.9$ meV. Different values have been reported for the constants a and b in the above relation. In our opinion, the most accurate values have been reported by Meyer et al. [113], namely $a = -3.8$ meV and $b = 0.365$ meV. Using these values, E_D was calculated to be 45.8 meV. This agrees with the value reported in Ref. [72]. In the prepared ZnO NPs, it seems entirely plausible that hydrogen (from precursor) is the dominant donor.

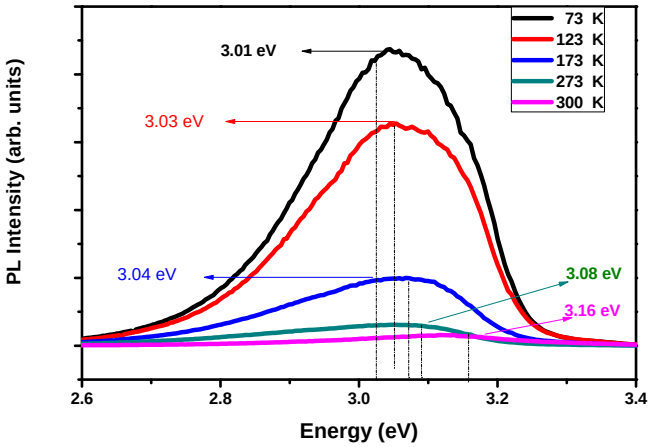

Figure 5.8: Temperature dependent PL emission of ZnO nanoparticles prepared at 200 ^0C.

Fig. 5.8 shows temperature-dependent PL for ZnO NPs prepared at a temperature of 200 ^0C, for which five distinct deep-level emission peaks at 3.01 eV, 3.03 eV, 3.04 eV, 3.08 eV and 3.16 eV were observed which was ascribed to native defects. The temperature-dependent PL spectra shown in Fig. 5.9(A), for sample of ZnO NPs prepared at 300 ^0C clearly depicts thermal redistribution among states compared to the ZnO sample prepared at 200 ^0C. The transition line at 3.01 eV were attributed to native defect(V_{zn}) and the near-band-edge (NBE) emission

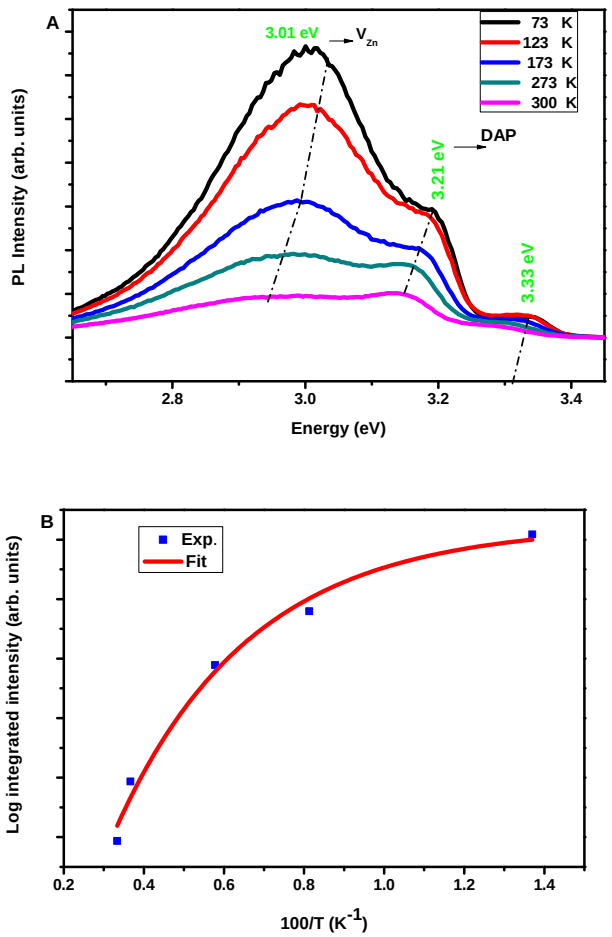

Figure 5.9: (A). Temperature dependent PL emission of ZnO nanoparticles prepared at 300 ^0C and (B). shows thermally activated luminescence quenching of the 3.21 eV emission for the ZnO NPs prepared at a temperature of 300 ^0C.

.

peak at 3.21 eV were assigned to DAP. The peak labeled in 3.21 eV gains strength with decreasing temperature, in contrast, peak labeled 3.01 eV is strong at low temperature because carriers are trapped at these sites and do not have enough thermal energy to escape, but it disappears at room temperature(300 K) because the states are sparse relative to the intrinsic bands. With increasing temperature, the DAP emission energy was shifted to the low energy side because carriers on DAP with small donor-acceptor distance are released into the band [13, 17, 133]. The transition at 3.33 eV is ascribed to excitons bound to structural defects. This transition line at 3.33 eV was previously observed in various ZnO samples and tentatively ascribed to donor bound excitons (DX), acceptor bound excitons,

transitions of intrinsic point defects and excitons bound to extended structural defects. In their work, the 3.33 eV emission line was attributed to recombination of excitons bound to extended structural donor defect complexes which disappear at temperature of 10 K. Study done by Urgessa et al. [93] on ZnO nanorods growth for temperature dependent PL also observe dominance of donor-bound exciton as possible reason for this emission.

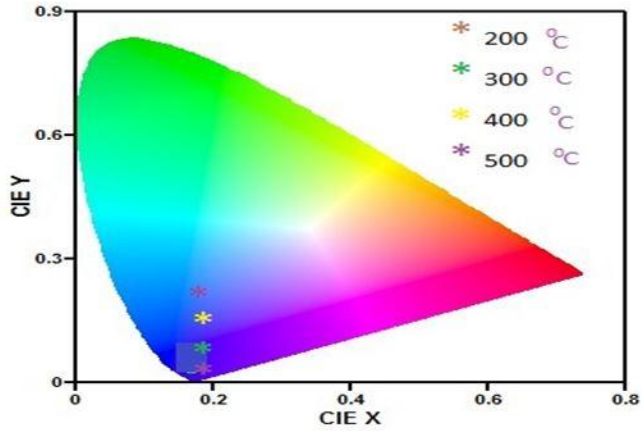

Figure 5.10: CIE diagram for temperature dependent PL sample and ZnO prepared at various measuring temperature.

.

Fig. 6.11 illustrates the Commission Internationale de l'Eclairage (CIE) chromaticity diagram of ZnO NPs prepared at various growth temperatures calculated using photoluminescence data and color calculator software. The coordinates were shown deep blue region with the increase in annealing temperature indicating growth temperature play a major role in tuning the emission color of the ZnO NPs.

5.7 Conclusion

In conclusion, the luminescent properties of ZnO NPs prepared from zinc precursor at various decomposition temperatures have been investigated. The samples of ZnO NPs synthesized at a temperature from $200-500\ ^0C$ exhibits broad visible emission. ZnO NPs with crystallite size of $16-20$ nm and hexagonal wurtzite

structure was successfully produced. A linear increase in lattice parameters and grain size with temperature was observed. It was demonstrated that the morphology and band gap energy of ZnO NPs can be tuned with annealing temperature. The temperature dependent PL spectra of ZnO NPs prepared at a temperature of 300 ^0C shows three transition lines at 3.01 eV, 3.21 eV and 3.33 eV which are ascribed to zinc vacancy (V_{zn}), donor-acceptor pairs (DAP) and excitons bound to structural defects respectively. The activation and binding energy for the transition at 3.21 eV were calculated to be about 12.9 meV and 45.8 meV respectively. Depending on the hydrogen concentration in the precursor and these energy values, hydrogen was suggested to be the possible impurity acting as donor in our material. It is believed that ZnO NPs produced using this method would be quick and cost effective synthesis method for blue light emitting fluorescent applications.

Chapter 6

Wide visible emission and narrowing band gap in Cd-doped ZnO nanopowders synthesized via sol-gel route

6.1 Introduction

The possibility of engineering band gap and influencing physical, chemical, and electronic properties by varying the dimensions of the system has provided a strong impetus to study nanocrystals and other nanodimensional material [1]. However, it is being realized that tuning the band gap by changing the diameters of nanocrystals is not well suited for use in some applications such as some types of fluorescent imaging and nanoelectronics [142, 143, 150]. The rationale is that changes in diameters lead to changes in the nature of nanocrystals such as its reactivity and its ability to self-assemble. Therefore, attempts have been made to tune band gap by varying the composition of nanocrystals instead of the diameter. Furthermore, it is possible to increase as well as decrease the band gap by the use of the right dopants, as opposed to size induced tuning, wherein the band gap can only be increased [126]. It appears, that successful doping of nanocrystals can be achieved by involving nanocrystals of the right size, morphology and choosing surfactants that do not bind too strongly to the dopant ions [106, 145]. Therefore, considerable recent research has focused on alternative doping schemes.

ZnO, a wide band-gap ($3.37eV$) semiconductor, has been extensively studied due to its intrinsic properties and potential for uses in devices, such as field-effect

transistors, resonators, gas sensors, solar cells, and as a catalyst to further widen its useable wavelength range and improve the efficiency [110, 111, 112]. Although Al-doped ZnO have shown some intriguing features, there remains an unresolved problem concerning the environmental stability. ZnO has been doped with Mg to enlarge the band gap and with Cd to narrow the band gap [113, 114, 115, 116]. In either case, alloys of the form $Mg_xZn_{1-x}O$ or $Cd_yZn_{1-y}O$ with hexagonal zincite structure have been formed. In this regard Cd: ZnO has been shown to be an interesting option. Importantly, Cd doping reduces the energy band gap and results in a red-shift of absorption edge [117, 118, 119, 120]; hence, one can envision varying the Cd-doping concentration to tailor the electronic gaps to produce materials of interest as they are isoelectronic transition metals. In addition, incorporation of Cd into ZnO produces a material with increased conductivity [121, 122, 123, 124]. and increased carrier concentration (up to $2.69x10^{20}cm^{-3}$) versus the parent ZnO. Such characteristics of Cd: ZnO make it desirable for PV applications, including UV sensors, UV LEDs, and UV protecting layers [125, 126].

Investigations on the synthesis and modification of nanosized ZnO have attracted tremendous attentions. Different synthesis methods have been developed, including sol-gel, mechanochemical, spray pyrolysis and drying, thermal decomposition of organic precursor [106, 109, 127], self assembling, hydrothermal processing, vapor transport, sonochemical or microwave-assisted synthesis, direct precipitation and homogeneous precipitation are mentioned. Among these techniques, sol-gel is appealing because of many advantages like easy for compositional modification, simple and inexpensive equipment, and minimum variables to control the growth of sample with excellent control on stoichiometry [128, 129, 130].

In light of the above observations, we thought it would be interesting to carry out doping ZnO nanocrystals with Cd compositional variation with diameters in a range unaffected by quantum confinement effects using a sol-gel route. In the present work, we report the changes in the optical and structural properties of ZnO nanocrystals brought about by successful doping with Cd.

6.2 Experiment

6.2.1 Preparation

A simple and versatile sol-gel route has been adopted to prepare nanopowders $Zn_{1-X}Cd_XO$ $(0.15 \leq X \leq 0.45)$. All the chemicals used were purchased from Sigma Aldrich and used without further purification. In this typical sol-gel method appropriate proportions of zinc acetate dihydrate $Zn(CH_3COO)_2 2H_2O$ (99.9%) and cadmium acetate dihydrate $Cd(CH_3COO)_2 2H_2O$ (99.9%) were dissolved into 120 mL of anhydrous ethanol and heated to reflux at 80^0C for 3 hr. Then, the required $Cd(CH_3COO)_2 2H_2O$ was then added to form the desired molar ratio (X=Cd/Cd+Zn), $(0.15 \leq X \leq 0.45)$. Simultaneously, LiOH (0.3024 g) was dissolved in 20 mL of anhydrous ethanol and kept in an ultrasonic bath for 30 min. This solution was slowly added to the Zn^{2+} and Cd^{2+} solution under a reflux condenser at 80^0C for $1:20$ hr. The solution was repeatedly washed with n-hexane to remove unwanted ions, and the obtained precipitate was dried in a vacuum oven to afford Cd-doped ZnO as white powders.

6.2.2 Characterization

The crystal structures of the samples were determined with a Bruker AXS D8 ADVANCE Discover diffractometer (XRD), with Cu Ka (1.5418 A 0) radiation operating at 40 kV and 40 mA, the diffraction spectra were recorded in the 2 hr range $30 - 70$. Surface morphologies were studied using a scanning electron microscope(SEM) (Shimadzu model ZU SSX-550 Superscan) equipped with EDX. The optical measurements were carried out in the $300 - 650$ nm wavelength range using a Perkin Elmer UV/Vis Lambda 20 powder Spectrophotometer. Luminescence measurements were done using a photoluminescent (PL) laser system 5.0 (Photon systems, USA), which uses a He-Cd laser with an excitation wavelength of 248.6 nm.

6.3 Result and discussions

6.3.1 Structural studies

Fig. 7.1 shows XRD patterns of the ZnO for different concentration of Cd produced via the sol-gel method. It shows series of broad diffraction peaks (2θ) at 31.63, 34.50, 36.25, 47.50, 56.60, 62.80 and 67.92; which could be correspondingly indexed as the diffraction of (100), (002), (101), (102), (110), (103) and (112) planes of ZnO (JCPDS card No. $36-1451$) and were indexed as a hexagonal wurtzite structure of ZnO. Because no impurity peak associated with Cd clusters or CdO was detected, indicating the prepared nanopowders ($Zn_{1-X}Cd_XO$, $0.15 \leq X \leq 0.45$) are entirely consisting of ZnO phase with hexagonal wurtzite structures. Therefore, the broadening of the XRD peaks (i.e., Scherer broadening) gave a clear indication of the formation of nanosized ZnO, and the wurtzite phase was not disturbed by the addition of Cd^{2+} during the sample preparation. The crystallite size of the ZnO with different Cd concentration were estimated using the Debye-Scherer Eq.6.3.1 :

$$D = \frac{0.9\lambda}{\beta \cos\theta}, \tag{6.3.1}$$

where D is the crystallite size, λ is the wavelength of radiation used, θ is the Bragg diffraction angle and β is the full width at half maximum. It is observed that the (101) characteristic peak of the ($Zn_{1-X}Cd_XO$, $0.15 \leq X \leq 0.45$) moved to the lower angle monotonously from 36.25 to 34.50, while the c value gradually increased from 0.520 to 0.524 nm with increase in Cd concentration. This can be explained in terms of Bragg's relation: $2dsin\theta = \lambda$ where d is the interplanar distance, θ is the degree of diffraction, and λ is the wavelength of incident ray to be a constant. Considering that the Cd and Zn electronegativities on Pauling scale (1.69 and 1.65 respectively) are comparable and the ionic radii of Cd^{+2} (0.97) are larger than the ionic radii of Zn^{+2} (0.74) [104, 105].

Cd ions can easily substitute into Zn ions on the equivalent crystallographic position. The replacement of Zn by Cd makes the lattice parameter of the

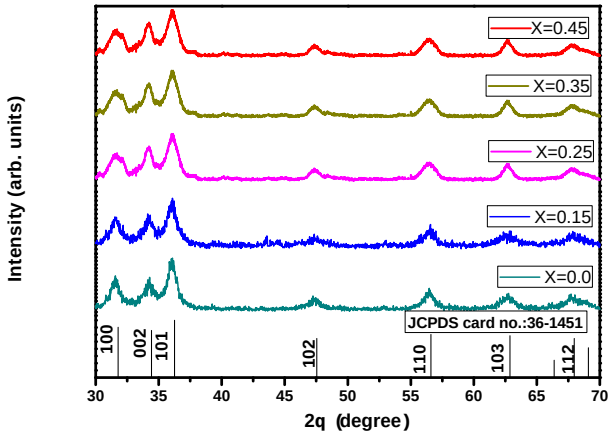

Figure 6.1: XRD patterns of the $Zn_{1-X}Cd_XO$ and undoped ZnO as-synthesized.

.

($Zn_{1-X}Cd_XO$ nanoparticles larger; therefore, increasing d will decreases the values of θ slightly towards lower 2θ value. This shift arises because of band gap modulation during increase in Cd content and similar results are reported in Refs. [107, 111]. The lattice parameters a and c of wurtzite structure are calculated using Eq. 6.3.2:

$$\frac{1}{d^2} = \frac{4}{3}\left(\frac{h^2 + hk + k^2}{a^2}\right) + \frac{l^2}{c^2} \tag{6.3.2}$$

where (hkl) are the Miller indices and d is interplanar spacing. It is observed that the calculated values of lattice parameter increases and the average crystallite size decreases with increase in Cd concentration which is ascribed to the higher ionic radius of the Cd^{2+} as compared to Zn^{2+} in the ZnO lattice. Fig. 6.2 shows the trends in 2θ angle vs C-axis lattice constant showing slight shift towards lower angle with increase in Cd concentration, implying the existence of lattice expansion in the c-axis orientation. Moreover, the evident increase of the FWHM with increase in Cd concentration (X) was observed in Fig.3 suggesting the increase of lattice defects and grain boundary defects as compared to SEM images. The fact that FWHM increases with increase in Cd concentration suggests that the prepared samples have a deterioration of the crystalline quality and decrease in crystallite size. Quantitative information concerning the preferential

crystallite orientation was obtained using the relation [103]. $I = I_{002}/I_{101} \sim 0.63$ which is higher than the corresponding standard value of 0.44 of bulk hexagonal wurtzite ZnO [1] suggesting the prepared ($Zn_{1-X}Cd_XO$ alloys preferred the (002) orientation.

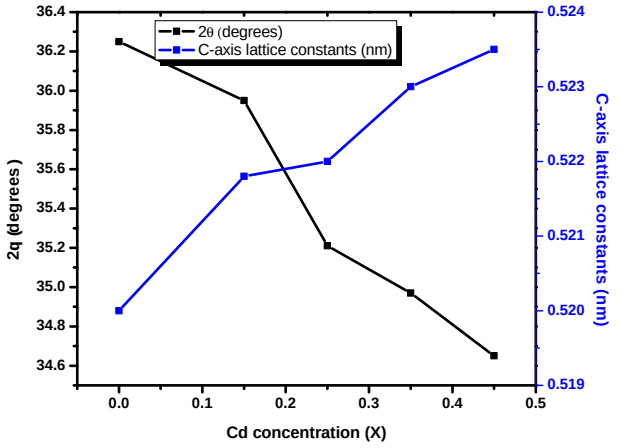

Figure 6.2: XRD pattern (Variation of 2θ) vs C-axis lattice constant.

.

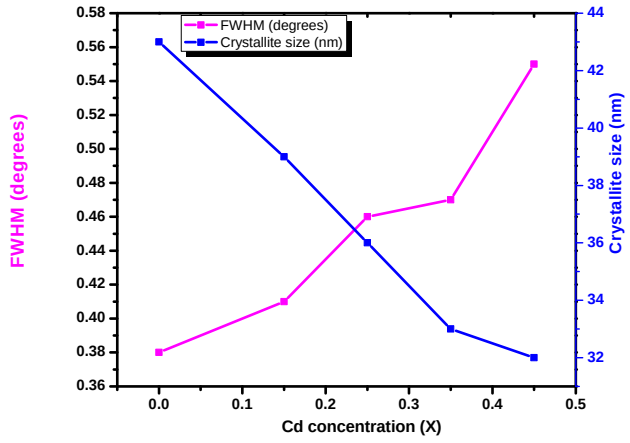

Figure 6.3: The variation in Crystallite size versus 2θ of FWHM (degree)

.

Fig. 7.2 shows the SEM images of the sample prepared for X=0.15 in (A) and, X=0.25 shown in (B) and the corresponding EDX pattern results are shown in (D) and (C) respectively. SEM measurement result shows that the sizes of the ($Zn_{1-X}Cd_XO$, $0.15 \leq X \leq 0.45$) nanoparticles are in the range of $32 - 44$ nm

which is in agreement with the calculated results. The EDX spectrum of Cd-ZnO (Fig. 7.2 C and D) confirms the presence of only Cadmium, Zinc and Oxygen in the prepared sample.

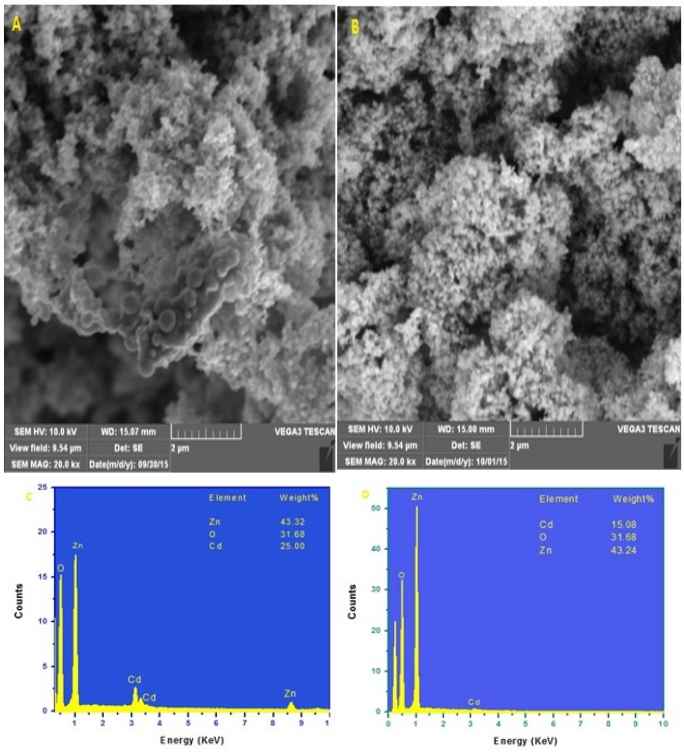

Figure 6.4: SEM image of sample prepared ($Zn_{1-X}Cd_XO$, $0.15 \leq X \leq 0.45$), for X=0.15(A) and X=0.25(B) and corresponding point EDX C and D results

.

6.3.2 Optical properties

The theory of optical transmission gives the relationship between the absorption coefficient (α) and photon energy ($h\nu$) for direct transition as $(\alpha h\nu) = A(h\nu - Eg)^n$ [109]. Where E_g is the optical band gaps corresponding to a particular sample, A is the band edge constant, ν is the transition frequency and 'n' can take the values 1/2, 3/2, 2 or 3, when the transition are direct allowed, direct forbidden, indirect allowed and indirect forbidden, respectively. The ZnO and Cd: ZnO both are considered as materials with direct band gap energy [81, 150, 151] and hence $n = 1/2$ is expected for direct allowed transition.

The transmittances of the prepared samples were collected by using UV-visible spectrophotometer as shown in Fig. 6.5. It was observed that the samples were

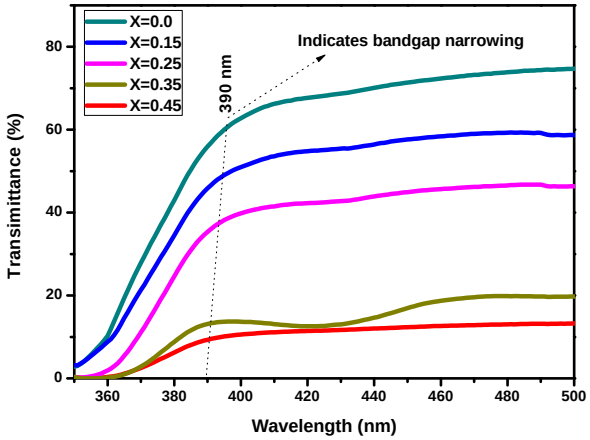

Figure 6.5: Transmittance spectra of $Zn_{1-X}Cd_XO$, $0.15 \leq X \leq 0.45$ and undoped ZnO.

highly transparent in the visible region and the transmittance was low in the ultraviolet region. Cd doping results a decrease in the transmittance. The samples exhibits in the range 50 and 10 % transmittance in the visible region and sharp ultraviolet absorption edge corresponding to undoped ZnO sample suffers significant red shift with the increase of cadmium content. The decrease in the transmittance might be due to band gap narrowing and free electron absorption and confirms that carrier concentration increases with increasing Cd concentration in doped samples [125, 126]. Fig. 6.6 depicts The absorbance spectra of undoped ZnO along with Cd doped samples. For undoped ZnO, an absorption edge rising steeply around 382 nm and 450 nm, where as ($Zn_{1-X}Cd_XO$, $0.15 \leq X \leq 0.45$) samples exhibit red shift of absorption edge and significant enhancement of light absorption in the range from 360 to 600 nm with increasing Cd concentartion. The 382 nm UV NBE has been well understood to be owing to the excitonic recombination. The bluegreen emission at (450 nm) is well known in ZnO based materials and which might be attributed to defects such as single ionized oxygen vacancies and high quantity of oxygen vacancies as suggested by Wang et. al. [117] for Cd doped ZnO nanotubes. The rise in absorption, observed on dopant concentration, can be, thus, largely attributed to the observed decrease in crystallinity of the material as confirmed from XRD. It can be noticed that main effect of the dopant

concentration is a red shift of the absorption edge accounting for reduction of the band-gap. This red-shift behavior of E_g might be attributed to the modification of electronic structure of ZnO with Cd doping.

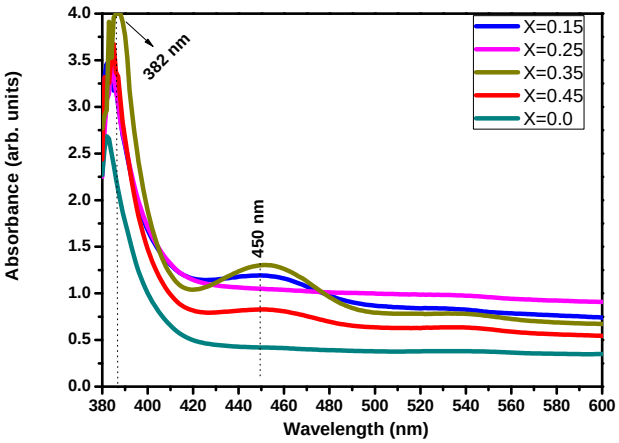

Figure 6.6: Absorbance spectra of $Zn_{1-X}Cd_XO$ ($0.15 \leq X \leq 0.45$).

Incorporation of Cd can enhance s states. With increasing Cd-doping concentrations, the s states at the bottom of the conduction band become stronger hence leads to a conduction band shift and band gap modulation. Fig. 6.7 shows band gap (E_g) of undoped ZnO and ($Zn_{1-X}Cd_XO$, $0.15 \leq X \leq 0.45$) are estimated using Tauc's equation as $(\alpha h\nu)^{\,2}$ versus $(h\nu)$[109]. The inset in Fig. 6.6 shows the plot of band gap versus Cd concentration (X) showing the narrowing band gap with increase in Cd for ZnO and ($Zn_{1-X}Cd_XO$, $0.15 \leq X \leq 0.45$). This band gap energies can be estimated by extrapolation of the linear portion of an $((\alpha h\nu)^2)$ vs $(h\nu)$ plot. This plot gives band gap energies 3.15 eV for pure ZnO and 3.05, 2.89, 2.79 and 2.76 eV for X= 0.15, 0.25,0.35 and 0.45 respectively. It leads to decrease in the ionic character of the X-O (X=Zn and Cd) on substitution of Cd in place of Zn. Moreover, Zhang et al. [118] reported that the bottom of the conduction band consists of Zn 4s and O $2p$ states, and the Zn $4s$ states are dominant. This band gap shift is plotted for comparison with the optical band gap speculated by transmittance spectrum. It is seen that both speculations gives nearly similar values and same variation trends. The variation of the peaks position in PL or

the band gap energy can be explained by the Cd doping. When Cd atoms substitute Zn atoms and enter into ZnO lattice, due to lower electron affinity of ZnO, the free electrons in the bottom of conduction band decrease and the number of vacancies increases, which alter the Fermi level to a lower position of conduction band [123]. Thus, the excitation energy necessary for electrons transition from valence band to the Fermi level in the conduction band becomes small, i.e. the radiative recombination of these excitons may lead to the observed red shift in the band gap.

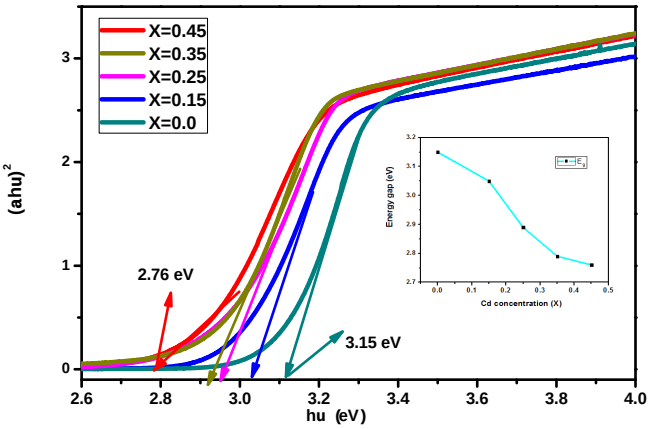

Figure 6.7: Band gap energy as a function of undoped ZnO and $Zn_{1-X}Cd_XO$, $0.15 \leq X \leq 0.45$ samples calculated using $((\alpha h\nu)^2)$ vs $(h\nu)$. The inset shows the band gap energy as a function of Cd concentration (X).

The room-temperature PL of undoped ZnO and ($Zn_{1-X}Cd_XO$, $0.15 \leq X \leq 0.45$) are shown in Fig. 7.3 which has two emission region. It can be seen that, only a strong UV emission was observed at $\sim$ 378.8 nm, which originates from a near-band-edge(NBE) transition of the wide band gap due to the annihilation of excitons , indicating that all prepared samples exhibit a pure wurtzite ZnO structure. In addition the PL spectra show very wide visible light emission outspreading from 425 to 600 nm emission which is attributed to both the intrinsic property $Zn_{1-X}Cd_XO$ and the introduction of vast crystalline defects due to the high doping concentration of Cd. This phenomenon is frequently observed in alloy semiconductors [130]. Such wide PL spectra consist of a series of visible light

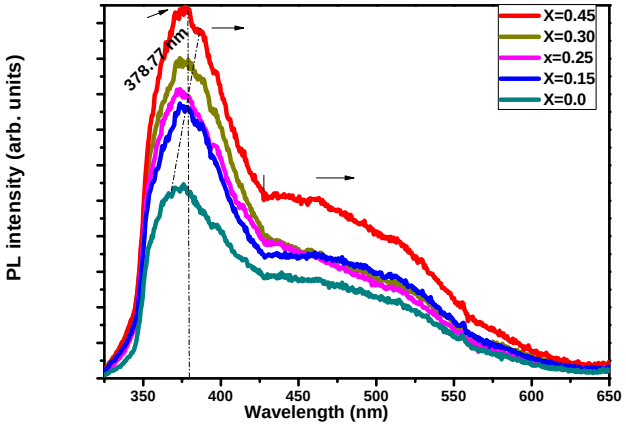

Figure 6.8: Room-temperature PL spectra of undoped ZnO and ($Zn_{1-X}Cd_XO$, $0.15 \leq X \leq 0.45$

.

corresponding to the violet, blue, green and yellow emissions and so on. Also it is obvious that with increasing X, the NBE emission from the ($Zn_{1-X}Cd_XO$, $0.15 \leq X \leq 0.45$) nanopowder is red-shifted. Because ZnO is a direct band-gap semiconductor, the PL peak energy of NBE emission can represent the value of band-gap. Therefore the variation of the peaks position is attributed to the modulation of band-gap caused by Cd substitution. This phenomenon suggests that the cadmium has been successfully incorporated into ZnO and can effectively adjust the band gap of ZnO. The observed red-shift UV emission peaks was attributed to the variation of the Fermi level to a lower position of conduction band, which can be explained by the decrease of free electrons in the bottom of conduction band caused by Cd atoms entering into ZnO lattice [129]. Fig. 6.9 shows the Gaussian deconvoluted room temperature PL spectra of powders with undoped ZnO(B), (X=0) and ($Zn_{1-X}Cd_XO$ for $X = 0.45$. The spectrum consists of a narrow and weak ultra-violet(UV) near-band-edge(NBE)emission at 378 nm and broad blue-green emission at around 463 nm shifted to 468.4 nm. Compared with that of the undoped ZnO, the UV NBE emission is slightly red-shifted due to the modulation of band-gap caused by Cd substitution. We note that the full-width

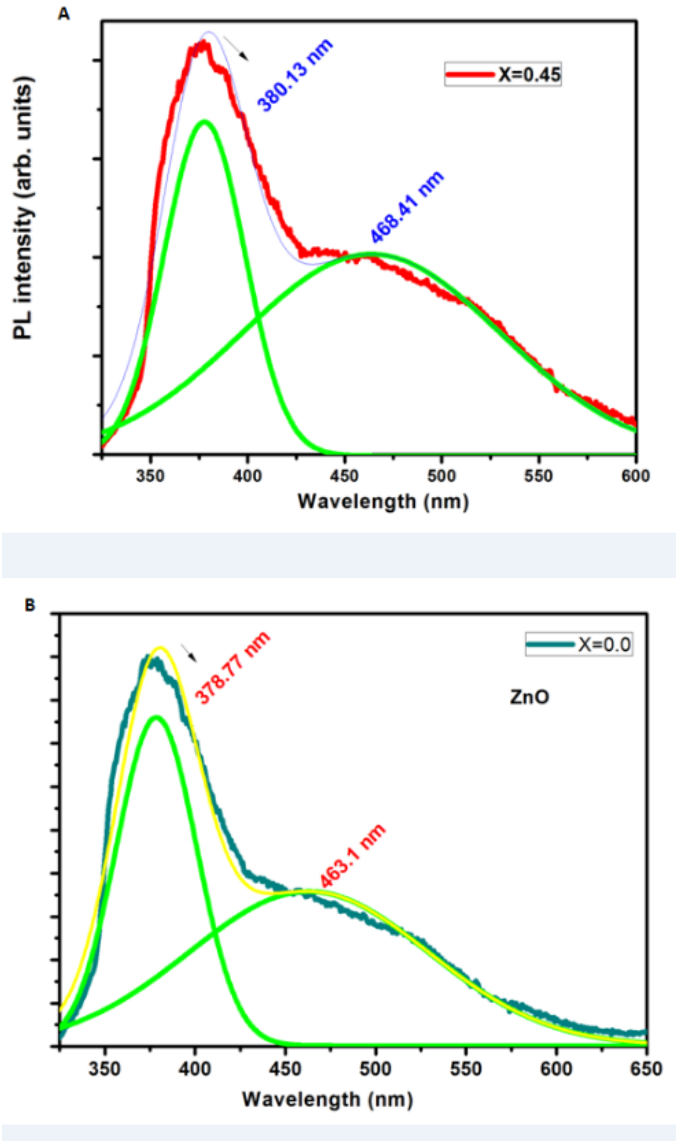

Figure 6.9: Gaussian deconvoluted room temperature PL spectra of powders with undoped ZnO(B), (X=0) and ($Zn_{1-X}Cd_XO$ for $X = 0.45$, as shown in A

.

at half-maximum (FWHM) of the NBE emission is slightly broadened. The inhomogeneous broadening has frequently been observed in alloy semiconductors and might be due to variation in Cd concentration or crystallographic defects, and strain-induced band-gap modification [114, 138].

The FTIR spectra of Cd doped ZnO samples are recorded in the region of $400 - 4000\ cm^{-1}$ as shown in Fig. 6.10. A series of absorption peaks from 1000 to $3500\ cm^{-1}$ are observed corresponding to the vibration modes of impurities. The absorption band in the region of $3426\ cm^{-1}$ corresponds to the O-H stretching

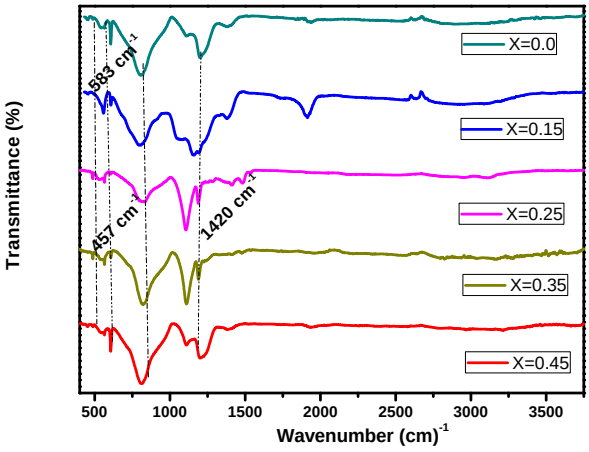

Figure 6.10: FTIR spectra of undoped ZnO and ($Zn_{1-X}Cd_XO$, $0.15 \leq X \leq 0.45$) as-synthesized samples

.

vibrations of water present in the powder sample. The FTIR band around 2900 cm^{-1} belongs to C-H stretching vibrations of the alkane. The band in the region 1600-1500 cm^{-1} corresponds to the vibrations of a carboxyl group(CO). The well known stretching mode of Cd=O was observed at 1420 cm^{-1}. Clear Zn-O-Zn stretching modes were observed at 457 cm^{-1}, and these stretching modes were indicative of the substitution of heavier Cd^{2+} ions into the Zn-O lattice, as previously confirmed by XRD. The absorption bands observed around 850 cm^{-1} and 1000 cm^{-1} corresponds to C-OH. The characteristic wurtzite lattice vibrations (Zn-O) are corresponding to the broadband in the range $400 - 600$ cm^{-1}. These Zn-O lattice vibrations can be assigned to the infrared active phonon modes A1(TO), E1(TO) and the corresponding surface phonon modes of TO bands [103, 104]. Fig. 6.11 illustrates the Commission Internationale de l'Eclairage (CIE) chromaticity diagram of undoped ZnO and ($Zn_{1-X}Cd_XO$, $0.15 \leq X \leq 0.45$) calculated using photoluminescence data and color calculator software. The result indicates that careful choice of dopant play a major role in tuning the emission color of the ZnO.

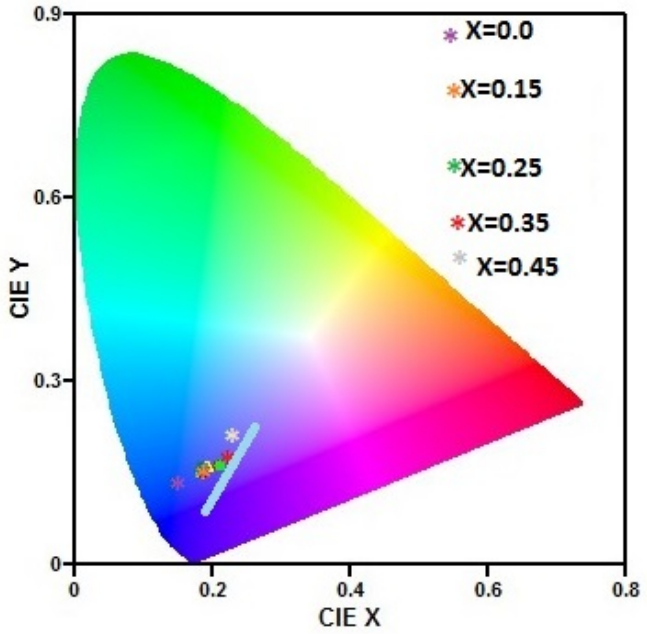

Figure 6.11: CIE diagram of undoped ZnO and ($Zn_{1-X}Cd_XO$, $0.15 \leq X \leq 0.45$) samples.

6.4 Conclusion

We have synthesized successfully Cd doped ZnO powders by simple and cost effective sol-gel method. The effects of Cd doping on the structure and optical properties of ZnO are investigated. XRD, and FTIR spectroscopy confirm the formation of wurtzite structure of ZnO for Cd concentration. The SEM images and EDX spectra shows that the crystallite size decrease with increase in Cd concentration and there are no foreign element other than Zn, Cd and O in the prepared samples. The PL spectra shows strong UV emission at 378.8 nm and very wide visible light emission outspreading from 425 to 600 nm which is frequently observed in alloy semiconductors. The UV-vis spectroscopy study reveals that the optical band gap ($Zn_{1-X}Cd_XO$, $0.15 \leq X \leq 0.45$) alloys show red-shift. Cd-doping can effectively adjust and tune ZnO for narrow band gap appilications. In summary, we suggest that the method employed would be efficient to synthesize material for devices operating in the visible region as well as for developing heterojunction (Cd:ZnO) structures.

Chapter 7

Defect-induced room temperature ferromagnetic properties of the Al-doped and undoped ZnO nanostructure

7.1 Introduction

Currently, ZnO presents a great interest for the scientific community due to its applications like UV light emitters, varistors, transparent high power electronics, surface acoustic wave devices, piezoelectric transducers, gas sensing and as window material for display and solar cells [1, 2, 3, 4]. Doping semiconductor with foreign elements to manipulate their electrical and magnetic properties is an important aspect for the realization of various types of advanced nanodevices [11, 12, 13, 14, 15]. The most promising dopants for obtaining p-type conductivity are the elements from the V^{th} group. The group III elements (Al, Ga, and In) are typical shallow donors in single crystals of ZnO. Aluminum (Al) is among the dopant that can be used to enhance phonon scattering promoted by Al induced grain reinforcement and is one of the most intriguing candidates for replacing traditional tin-doped indium oxide(ITO)transparent conducting oxide(TCO) films [111, 112, 113], which are essential components for a large variety of optoelectronic devices,acting as transparent electrical contacts or electrodes [114]. Al-doped ZnO based heterojunctions were successfully assembled into various kinds of optoelectronic devices [115], and also be applied as attachments of gold nanoparticles in nonlinear optical nanocomposite materials [116].

The most significant impediment in developing and exploiting zinc oxide based materials in electronic and photonic applications is the difficulty in carrier doping (achieving a p-type material); n-type conductivity of ZnO is relatively easy to realize using excess Zn or by doping zinc oxide with Al, Ga and In [117, 118, 119]. By using electron paramagnetic resonance (EPR) spectroscopy, the In and Ga shallow donors were identified on the basis of the resolved hyperfine (HF) structure in EPR spectra [112]. After the theoretical prediction of room temperature ferromagnetism (RTFM) in Mn-doped ZnO by Dietl et al.[125], ZnO doped with magnetic transition metal (TM) ions was intensively studied due to its potential applications in future spintronic devices, magneto-optics and magnetoelectronics. Hundreds of experimental and theoretical papers devoted to the research of ferromagnetism in doped ZnO, e.g., with Mn, Fe, Co, have been published [123]. It was also reported that even doping with "nonmagnetic" atoms, such as Cu or Bi, leads to RTFM in ZnO [117, 118, 119]. More recently, ferromagnetism had been observed in undoped ZnO, which opened an extensive debate on the origin of ferromagnetism (FM) as discussed in Refs. [121, 122]. Therefore, some researches suggested that induced FM is due to oxygen defects in ZnO, not TM ions or secondary phases [128].

More importantly the saturation magnetization of ZnO can be dramatically increased by doping with transition metals. There has been a considerable interest in the fabrication of transition metal-doped ZnO as a promising material for the discovery of room temperature ferromagnetism (RTFM) in implementing spintronic devices [123, 124, 125]. Nowadays various methods have been presented for preparing AZO nanopowders such as solgel, spray pyrolysis, precipitation , and hydrothermal processes [125]. Among these methods, the solgel process had attracted considerable attention because of its simplicity, inexpensive equipment, and minimum variables to control the growth of sample with excellent control on stoichiometry and the crystalline quality of the ZnO prepared by the solgel process [129, 130, 131, 132, 133].

In this paper, we therefore report on hyperfine splitting through the paramagnetic resonance (EPR) measurements, the morphological, magnetic and optical properties of ($Zn_{1-X}Al_XO$, $0.1 \leq X \leq 0.30$). Moreover, from EPR signal it is demonstrated that ZnO nanocrystals can be doped with Al to form shallow substitutional donors and the underlying mechanism for hyperfine splitting and origin of ferromagnetism are also presented.

7.2 Experiment

7.2.1 Preparation

AZO were prepared by a facile solgel technique reported elsewhere [18-22]. All the chemicals used were purchased from Sigma Aldrich and used without further purification. Zinc acetate [$Zn(CH_3COO)_2.2H_2O$] were dissolved in a 2-methoxyethanol-mono ethanolamine(MEA) deionized water solution at room temperature. The molar ratio of MEA and deionized water to zinc acetate was kept between 1 and 0.3, respectively, and the concentration of zinc acetate was 0.75 mol/L. Then appropriate amounts of aluminum doping were achieved by adding $AlCl_3.6H_2O$ to the precursor solution. In order to study an effect of the Al-doped concentration on magnetic, optical, and structural properties of the AZO samples, five solutions with doped concentration of $Al/Zn = 0.1, 0.15, 0.2, 0.25, 0.3$ respectively were used. Then these solutions were stirred at 80 ^0C for 45 min to yield clear and homogeneous solutions. Finally,the samples were washed with deionized water and dried in the air at 90 ^{0}C.

7.2.2 Characterization

The crystal structures of the samples were determined with a Bruker AXS D8 ADVANCE Discover diffractometer(XRD), with Cu Ka (1.5418) radiation. Surface morphologies and elemental compositions were studied using a scanning electron microscope(SEM) (Shimadzu model ZU SSX-550 Superscan) equipped with EDX. The optical absorption measurements were carried out in the $200 - 600$ nm

wavelength range using a Perkin Elmer UV/Vis Lambda 20 powder Spectrophotometer. Luminescence measurements were done using a photoluminescent (PL) laser system 5.0 (Photon systems, USA), which uses a He-Cd laser with an excitation wavelength of 248.6 nm. The microwave absorption measurements were carried out using a JEOL electron paramagnetic resonance (EPR) spectrometer operating at 9.4 GHz (x-band) at room temperature (298 K). The powder were placed in the cavity centre at a position where the microwave magnetic field is maximum. The DC static field HDC was slowly swept between 0 and 500 mT. The microwave power was kept at 5 mW to avoid saturation. The DC field was modulated with a superposed ac field whose amplitude was varied between 1 mT and 6 mT at 100 kHz frequency. The microwave response was measured as a derivative of microwave absorption signal.

7.3 Result and discussions

7.3.1 Structural studies

Fig. 7.1 shows XRD patterns of undoped and Al doped ZnO nanocrystalline powders for different Al concentrations in the 2θ range 2080. It shows series of broad diffraction peaks at (2θ) = 31.63, 34.50, 36.25, 47.50, 56.60, 62.80 and 67.92; which could correspondingly be indexed from (100), (002), (101), (102), (110), (103) and (112) planes of ZnO (JCPDS card No. $36 - 1451$) and were indexed as a hexagonal wurtzite structure of ZnO. Figure 1B shows $\omega - scan$ (rocking curve) for the samples indicating the shifts towards the higher angles. Here, no other impurity peaks were observed in the XRD patterns which show the purity of the nanoparticles formation. This result suggested that the nano powders have a polycrystalline hexagonal wurtzite structure with well developed crystallinity. The preferred crystal orientation in the sample corresponds to the (101) plane. The calculated lattice parameter and the shift in peak towards the larger angle are displayed in Table 7.1. Increase in crystallite size on Al doping arises due to reduction in the densities of nucleation centres are observed thus

to grow resulting in large crystallites this might because of decrease in sintering rate that occurred during the solgel process [135]. It was noted that from rocking

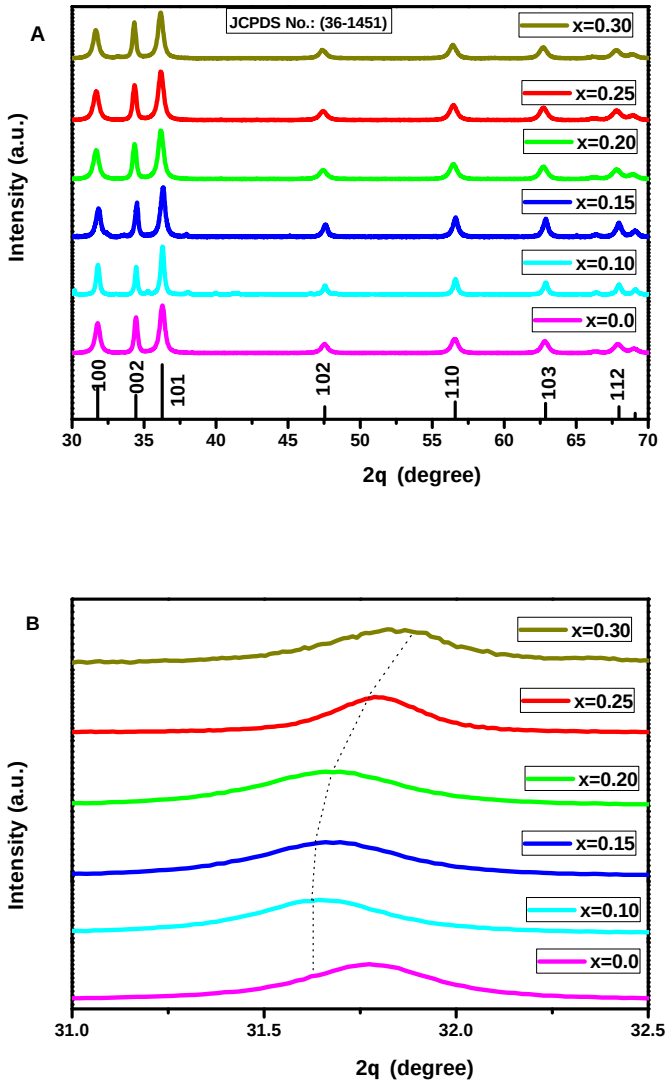

Figure 7.1: A.XRD patterns of undoped and Al doped ZnO nanocrystalline powders for different Al concentrations B. ω_{scan} (rocking curve) for samples having Al concentration at x=0.15, x=0.20, x=0.25, x=0.30.

.

curve(Fig. 7.1 B) the shift is indicative of a compressive stress incorporated in the ZnO lattice which likely shows Al^{+3} ions incorporated in Zn^{+2} sites.

The morphological and structural studies were investigated using scanning electron microscopy (SEM) as shown in Fig. 7.2(A, B C, D and E). These micrographs exhibited the formation of rod-like structures having diameters almost

Table 7.1: The calculated lattice constants of Al doped and undoped ZnO

Al Concent.	2θ	Lattice constants, a ($\mathring{A}$)	Lattice constants, c ($\mathring{A}$)
0.00%	31.46	3.248	5.299
0.10%	31.47	3.247	5.302
0.15%	31.67	3.245	5.305
0.20%	31.71	3.243	5.307
0.25%	31.77	3.241	5.307
0.30%	31.87	3.240	5.307

ranging from 0.6 to 1 μ m. Moreover the randomly oriented and packed rods become more visible as the concentration of Al increases. This demonstrates that Al doping would result in ZnO grains growing preferentially with c-axis parallel to the ZnO host crystal. The EDX pattern shown in Fig. 7.2 F, G, H, I, J and K confirms the existence of all expected elemental compositions (Zn, O and Al) in the samples.

Electron Paramagnetic Resonance (EPR) spectroscopy is an effective tool to investigate the origin and nature of un-paired electrons in an atom. These un-paired electrons which are 10,000 times lighter than atoms have their intrinsic spin contributing to some sort of magnetism [153, 154, 155]. Incorporating transition metal like Mn, is believed to alter the electron spin (magnetism) of semiconducting materials hence called diluted magnetic semiconductors (DMS). Fig. 7.4 A shows the derivative of microwave absorption as a function of magnetic flux density (DC field) for the un-doped and Al-doped ZnO nanopowders for different concentration of Al. The plots display two absorption peaks centred at HDC . 150; and 250 mT which are all assigned to paramagnetism and ferromagnetism resonant field respectively, at different atomic layers. The observed paramagnetism is due to the different magnetic clusters of defects situated near the surface and/or inside bulk. These are coming from electron spin trapped in defected areas. With increasing Al^{3+} concentrations, however, the hyperfine lines are overlapped to form a single broad line due to exchange interactions taking place between Al^{3+} ions as depicted

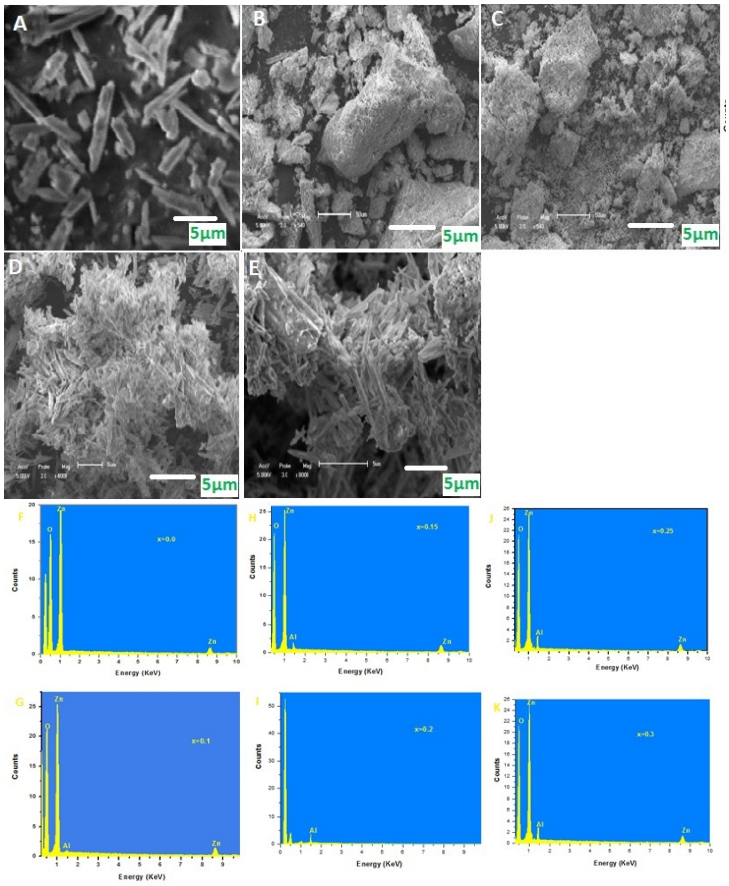

Figure 7.2: SEM micrograph and EDX spectrum of ZnO nanoparticles at: (A)undoped ZnO. (B)$x = 0.1$. (C)$x = 0.15$ (D)$x = 0.20$ (E)$x = 0.30$ and F, G, H, I, J and K are the corresponding EDX spectras of $x = 0.0$, $x = 0.1$, $x = 0.15$, $x = 0.20$, $x = 0.25$ and $x = 0.3$, respectively.

in Fig. 7.4 B.

In the present work, XRD and EDX analyses clearly demonstrated that the samples have a single wurtzite phase and there is no formation of secondary phases. Therefore we speculate that magnetism is from an intrinsic exchange interaction of magnetic moments in undoped ZnO. Although the exact mechanism of intrinsic FM in undoped oxides is still under debate, defects have greatly been suggested to play an important role in the FM origin in the undoped ZnO system. As it supported by our PL analysis section such vacancies may very likely carry a net moment for the origin of ferromagnetism in our observation.

To investigate the presence of defects, the RT photoluminescence (PL) spectra of ZnO for Al doped and undoped ZnO has been investigated. Fig. 7.3 shows

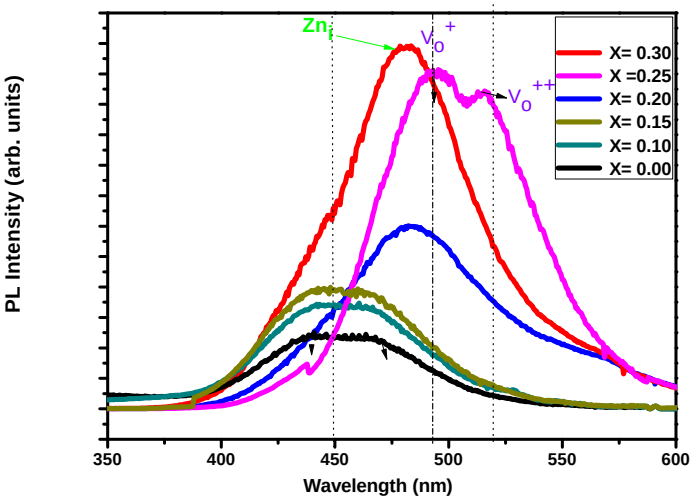

Figure 7.3: PL emission of ZnO nanoparticles synthesized at various temperatures.

room temperature PL spectrum which is enhanced with increase in Al concentration. In the PL spectra, a strong UV near band edge and two, emission peaks related to blue and green emissions are observed at around 435, 490 and 520 nm, respectively, for the undoped ZnO. The 435 nm peak is attributed to the exciton recombination process. the blue luminescence around 450 nm is assigned to electronic transitions from Zn interstitial levels (Z_{ni}) to valence band [151, 152]. The green emission around 490 nm is generally attributed to the recombination of electrons trapped in singly ionized oxygen vacancies (V_o^+) with photo generated holes. The emission at 520 nm is related to the doubly ionized oxygen vacancy (V_o^{++}) [1, 130]. These defects in ZnO have been attributed to be responsible for room temperature FM observed in un-doped ZnO structures [123].

According to the combination of results from the PL, EDX and EPR measurements, a positive correlation between the FM and the intensity of Zn interstitials (Z_{ni}) and oxygen vacancies (V_o^+) has been observed. PL and EPR analyses revealed that as the emission related to Z_{ni} and V_o^+ decreases, then the FM ordering also decrease with the Al concentration. Hence, one can conclude the observed FM in un-doped ZnO nanoparticles is due to both the Z_{ni} and V_o^+. However, the

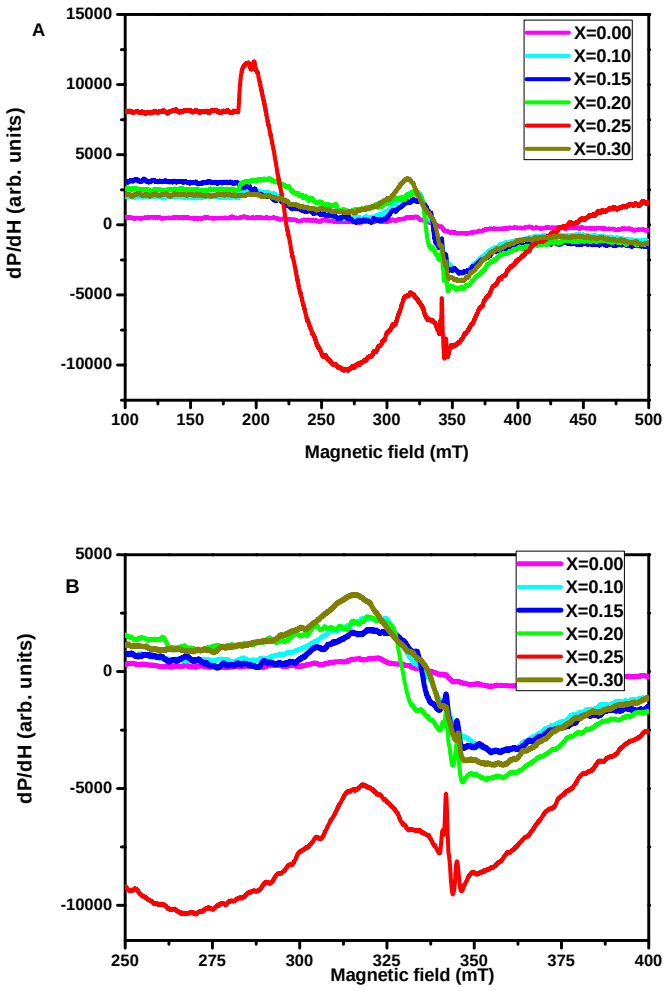

Figure 7.4: A. EPR measurements for the undoped and Al doped ZnO . B. Shows the enlarged EPR measurements which is highlighted in between 250-400 mT

role of defects in mediating the FM in undoped ZnO still needs further theoretical and experimental research.

7.4 Conclusion

We have synthesized successfully undoped ZnO and Al doped ZnO nanostructures by facile sol-gel approach. The effects of Al concentration on magnetic, optical and structural morphology are investigated. EPR and PL measurements confirms defects in particular, zinc interstitials and singly ionized oxygen vacancies, is the origin of ferromagnetic in undoped ZnO nanostructure. However, in the Al-doped

ZnO nanostructure, the suppression of FM ordering might be ascribed to the formation of Al short range orders. The structural analysis done by XRD, SEM images and EDX spectra reveals the presence of wurzite structure of ZnO, without any formation of impurities. In addition it is observed that Al^{3+} was successfully incorporated into the ZnO lattice. The PL spectra also supports the presence of defects in the synthesized materials.

Chapter 8

Conclusions and future work

8.1 Conclusions

In this thesis, the growth of ZnO nanostructures using a cost-effective, simple and environmentally friendly synthesis technique (sol-gel and chemical bath deposition) was studied. Theoretical and experimental study of core-shell structured ZnO/ZnS and growth mechanism of un-doped and doped ZnO nanomaterials has been investigated in detail. The salient results are summarized in this chapter, followed by suggestions for future work. Nanorods have been successfully synthesized on silicon substrates by a two-step process. ZnS coated ZnO nanorods were prepared by a simple, cost effective, two-step chemical synthesis process. This method provides a continuous, uniform ZnS coating on ZnO nanorods at relatively low temperature, by preventing shadowing effects, a significant drawback in vapour deposition techniques. The structure and morphology of the as-grown and sensitised nanorods were examined using scanning electron microscope (SEM) which are systematical related with theoretical calculations.

Our results also highlight prominently the importance of accurate determination of absorption coefficients and propagation length using effective medium theory and experimental parameters in WZ ZnO-ZnS hybrid systems. Possible variation of this parameter appears to affect the tendency of the peak intensity of the linear absorption coefficient with respect to the shell thickness in the conventional structure and also the threshold energy of the absorption coefficient and refractive index change in core-shell structures. Despite of this, we believe that

the present results would be useful not only in the elucidation of the fundamental physics but also for possible devices application based on ZnO/ZnS hybrid systems. Our theoretical calculations and numerical simulation demonstrate that the use of active host (amplifying) medium to compensate absorption at metallic inclusions plays great role.

Synthesis method of ZnO which is cost effective and rapid has been developed. The method requires only zinc precursor to produce NPs that can emit visible emission without external doping. X-ray diffraction (XRD) patterns confirm the prepared ZnO NPs is polycrystalline structure with wurtzite phase. The observed variation in scanning electron microscopy (SEM) images showed spherical shape of the ZnO NPs. It was found that the NPs exhibited the estimated direct bandgap (Eg) of 3.28 eV, 3.29 eV, 3.33 eV and 3.39 eV for a decomposition temperature of 500, 400, 300 and 200 ^0C. It has been suggested that ZnO NPs produced using this method would be ideal for blue light emitting fluorescent application as it is catalyst free growth, uses simple equipment, less hazardous and easy to control particle size and morphologies by scalable temperature. The low temperature PL characteristics were also systematically studied. In the case of as-grown samples and samples annealed at lower temperatures the dominant bound exciton line (I_4) was asymmetrically broadened on the low energy.

Cd doped ZnO has been synthesized by facile sol-gel approach. Importantly, Cd doping reduces the energy band gap and results in a red-shift of absorption edge. The observed red-shift UV emission peaks was attributed to the variation of the Fermi level to a lower position of conduction band, which can be explained by the decrease of free electrons in the bottom of conduction band caused by Cd atoms entering into ZnO lattice. In addition Cd-doping can effectively adjust and tune ZnO for narrow band gap applications. In summary, we suggest that the method employed would be efficient to synthesize material for devices operating in the visible region.

ZnO doped with magnetic transition metal (TM) ions was intensively studied

due to its potential applications in future spintronic devices, magneto-optics and magnetoelectronics. In this thesis, the origin of ferromagnetism in undoped ZnO Al doped ZnO has been investigated in detail using electron paramagnetic resonance. Although the exact mechanism of intrinsic FM in undoped oxides is still under debate, defects have greatly been suggested to play an important role in the FM origin in the undoped ZnO system. As it supported by our PL and EPR analysis section such vacancies may very likely carry a net moment for the origin of ferromagnetism in our observation.

8.2 Future work

A number of questions regarding ZnO nanomaterials from the point of view of its synthesis and its characterization have been addressed in this thesis. However, several topics remain unsolved and further investigations need to be completed in order to produce device quality material. Future work should include:

- Further studies of the formation of the interfacial layer, and effect of host amplifying medium
- Better control of the thickness and optimization of the ZnO/ZnS core-shell, layer studies in order to improve the surface quality and efficiency
- Detailed understanding of the underlying mechanism controlling the observed morphology and electrical properties.
- Studies to establish the formation mechanism of the stacking faults in order to reduce their density.
- The study related with p-type conduction and ferromagnetic behavior when doped with other transitions metals and their application in a type II(ZnS/ZnO) band alignment has been among the list of future works.

Publications

- **Leta T. Jule**, Francis B. Dejene, Abdub G. Ali, Kittessa T. Roro, Aiat Hegazy, Nageh K. Allam, Essam El Shenawy: Wide visible emission and narrowing band gap in Cd-doped ZnO nanopowders synthesized via sol-gel route, Journal of Alloys and Compounds 687 (2016) 920-926.

- **Leta Jule**, Francis Dejene, Kittessa Roro: Enhancing absorption in coated semiconductor nanowire/nanorod core-shell arrays using active host matrices, Optics Communications 380 (2016) 186-194.

- **Leta T. Jule**, Francis B. Dejene, Kittessa T. Roro, Zelalem N. Urgessa, Johannes R. Botha: Rapid synthesis of blue emitting ZnO nanoparticles for fluorescent applications, Physica B 497 (2016) 71-77.

- **Leta Jule**, Vadim Malnev, Belayneh Mesfin, Teshome Senbeta, Francis Dejene, and Kittessa Roro: Fano-like resonance and scattering in dielectric (core)-metal (shell) composites embedded in active host matrices, Phys. Status Solidi B 252, No. 12, 2707-2713 (2015).

- **Leta Jule**, Francis Dejene, Kittessa Roro, Bonex Mwakikunga, Abdub G. Ali: Defect-induced room temperature ferromagnetic properties of the Al-doped and undoped ZnO rod-like nanostructure, Materials Letters 199, 151-155 (2017).

- **Leta Jule**, Francis Dejene, Kittessa: Theoretical and computational study of ZnO/CdO core/shell heterostructures, (submitted on 7^{th} South African Conference on Photonic Materials, possibly published on Physica B).

Bibliography

[1] Ozgur, Alivov, Ya.I.; Liu, C.; Teke, A.; Reshchikov, M.A.; Dogan, S.; Avrutin, A.; Cho, S-J.; Morko, H. A comprehensive review of ZnO materials and devices. J. Appl. Phys. 2005, 98, 041301103

[2] Willander, M.; Nur, O.; Zhao, Q.X.; Yang, L.L.; Lorenz, M.; Cao, B.Q.; Zuniga Perez, J.; Czekalla, C.; Zimmermann, G.; Grundmann, M.; Bakin, A.; Behrends, A.; Al-Suleiman, M.; Al- Shaer, A.; Che Mofor, A., Postels, B.; Waag, A.; Boukos, N.; Travlos, A.; Kwack, H.S.; Guinard, J.; Le Si Dang, D. Topical review: Zinc oxide nanorods based photonic devices: Recent progress in growth, light emitting diodes and lasers. Nanotechnology 2009, 20, 332001

[3] Ahn, H.A.; Kim, Y.Y.; Kim, D.C.; Mohanta, S.K.; Cho, H.K. A comparative analysis of deep level emission in ZnO layers deposited by various methods. J. Appl. Phys. 2009, 105, 013502

[4] Liu, W.; Gu, L.S.; Ye, D.L.; Zhu, S.M.; Liu, S.M.; Zhou, X.; Zhang, R.; Shi, Y.; Hang, Y.; Zhang, C.L. Blue-yellow ZnO homo-structural light emitting diode realized by metal organic chemical vapour deposition technique. Appl. Phys Lett. 2006, 88, 092101

[5] Gao, P.X.; Ding, Y.; Wang, Z.L. Crystallographic orientation aligned ZnO nanorods grown by Tin catalyst. Nano. Lett. 2003, 3, 13151320

[6] Klingshirn, C. Review article: ZnO: From basics towards applications. Phys. Stat. Sol. B 2007, 244, 30273073

[7] Klingshirn, C.; Mollwo, E. Light scattering experiments with heavily Li-doped ZnO crystal. Zeitschrift fur Physik A 1972, 254, 437446

[8] Lander, J.J. Reactions of Lithium as a donor and an acceptor in ZnO. J. Phys. Chem. 1960, 15, 324334

[9] Zwingel, D. Trapping and recombination processes in the thermoluminscence of Li-doped ZnO single crystal. J. Lumin. 1972, 5, 385405

[10] Look, D.C.; Claflin, B. P-type doping and devices based on ZnO. Phys. Stat. Sol. B 2004, 241, 624630

[11] Bunn, C.W. The lattice dimensions of zinc oxide. Proc. Phys. Soc. London 1935, 47, 835842

[12] Gao, P.X.; Wang, Z.L. High-yield synthesis of single crystal nano-springs of ZnO. Small 2005, 1, 945949

[13] Fuller, M.L. Twinning in zinc oxide. J. Appl. Phys. 1944, 15, 164170

[14] Janotti, A.; van de Walle, C.G. Native point defects in ZnO. Phys. Rev. B 2007, 76, 165202165222

[15] Van de Walle, C.G.; Neugebauer, J. First principle calculations for defects and impurities: applications to III-nitrides. J. Appl. Phys. 2004, 95, 38513879

[16] Mooney, P.M. Identification of Defects in Semiconductors in Semiconductors and Semimetals; Academic press: San Diego, CA, USA, 1999; Volume 51B, 93152.

[17] Look, D.C.; Hemsky, J.W.; Sizelove, J.R. Residual native shallow donors in ZnO. Phys. Rev. Lett. 1999, 82, 25522555

[18] Krger, F.A. The Chemistry of Imperfect Crystals; North Holland press: Amsterdam, The Netherland, 1964

[19] Tuomisto, F.; Saarinen, K.; Look, D.C.; Farlow, G.C. Introduction and recovery of point defects in electron irradiated ZnO. Phys. Rev. B 2005, 72, 085206085211

[20] Tuomisto, F.; Saarinen, K.; Look, D.C. Irradiation induced defects in ZnO studied by positron annihilation spectroscopy. Phys. Stat. Sol. C 2004, 201, 2219-2224

[21] Look, D.C.; Farlow, G.C.; Reunchan, P.; Limpijumnong, S.; Zhang, S.B.; Nordlund, K. Evidence of native defect donors in n-type ZnO. Phys. Rev. Lett. 2005, 95, 225502

[22] Kroger, F.A.; Vink, H.J. The origin of florescence in sled activated ZnS, CdS, and ZnO. J. Chem. Phys. 1954, 22, 250-252

[23] Kohan, A.F.; Ceder, G.; Morgan, D.; van de Walle, C.G. First principles study of native point defects in ZnO. Phys. Rev. B 2000, 22, 1501915027

[24] Oba, F.; Nishitani, S.R.; Isotani, S.; Adachi, H.; Tanaka, I. Energetics of native point defects in ZnO. J. Appl. Phys. 2001, 90, 824828

[25] van de Walle, C.G. Hydrogen as a doping cause n ZnO. Phys. Rev. Lett. 2000, 85, 10121015

[26] Reynolds, D.C.; Look, D.C.; Jogai, B.; Morkoc, H. Similarities in the band edge and deep-center photoluminescence mechanisms in GaN and ZnO. Sol. Stat. Comm. 1997, 101, 643646

[27] Liu, M.; Kiati, A.H.; Mascher, P. Point defects and luminescence centers in ZnO and ZnO doped with manganese. J. Lumin. 1992, 54, 3542

[28] Zhong Lin Wang, Zinc oxide nanostructures: growth, properties and applications, J. Phys.: Condens. Matter 16 (2004) R829-R858

[29] Kassai, P.H. Electron spin resonance studies of donors in ZnO. Phys. Rev. 1963, 130, 989995

[30] Studenikin, A.; Golego, N.; Cocivera, M. Fabrication of green and orange photoluminescence, undoped ZnO films by spray pyrolsis. J. Appl. Phys. 1998, 84, 22872294

[31] Yamauchi, S.; Goto, Y.; Hariu, T. Photoluminescence studies of un-doped and nitrogen-doped ZnO layers grown by plasma assisted epitaxy. J. Cryst. Growth 2004, 260, 16

[32] Zhao, Q.X.; Klason, P.; Willander, M.; Zhong, H.M.; Lu, W., Yang, J.H. Deep level emissions influence by O and Zn implantation. Appl. Phys. Lett. 2005, 87, 211912:1211912:3.

[33] Borseth, T.M.; Svensson, B.G.; Kuznetsov A.Y.; Klason, P.; Zhao, Q.X.; Willander, M. Identification of zinc and oxygen vacancy optical signals in ZnO. Appl. Phys. Lett. 2006, 89, 262112

[34] Klason, P.; Brseth, T.M.; Zhao, Q.X.; Svensson, B.G.; Kuznetsov, A.Y.; Willander, M. Temperature dependence and decay times of zinc and oxygen vacancies related photoluminescence in ZnO. Sol. Stat. Commun. 2008, 145, 321326

[35] Schirmer, O.F.; Zwingel, D. The yellow luminescence of ZnO. Sol. Stat. Commun. 1970, 8, 15591563

[36] Liu, M.; Kitai, A.H.; Mascher, P. Point defects and luminescence centers in zinc oxide and zinc oxide doped with manganese. J. Lumin. 1992, 54, 3542

[37] Wu, X.L.; Siu, G.G.; Fu, C.L.; Ong, H.C. Photoluminescence and cathodoluminescence studies of stochiometric and oxygen deficiency in ZnO. Appl. Phys. Lett. 2001, 78, 22852287

[38] Li, D.; Leung, Y.H.; Djurisic, A.B.; Liu, Z.T.; Xie, M.H.; Shi, S.L.; Xu, S.J. Different origin of visible luminescence in ZnO nanostructures fabricated by the chemical and evaporation methods. Appl. Phys. Lett. 2004, 85, 16011603

[39] Magnus Willander, Omer Nur, Jamil Rana Sadaf, Muhammad Israr Qadir, Saima Zaman, Ahmed Zainelabdin, Nargis Bano and Ijaz Hussain, Materials 2010, 3, 2643-2667

[40] Greene, L.E.; Law, M.; Goldberger, J.; Kim, F.; Johnson, J.; Zhang, Y.; Saykally, R.J.; Yang, P. Low temperature wafer-scale production of ZnO nanowires arrays. Angew. Chem. Int. Ed. 2003, 42, 30313034

[41] Gomi, M.; Oohira, N.; Ozaki, K.; Koyano, M. Photoluminescence and structural properties of precipitated ZnO fine particles. Jpn. J. Appl. Phys. 2003, 42, 481485

[42] Djurisic, A.B.; Leung, Y.H.; Tam, K.H.; Hsu, Y.F.; Ding, L.; Ge, W.K.; Zhong, C.; Wong, K.S.; Chan, W.K.; Tam, H.L.; Cheah, K.W.; Kwok, W.M.; Phillips, D.L. Defect emissions in ZnO nanostructures. Nanotechnology 2007, 18, 095702

[43] Lima, S.A.M.; Sigoli, F.A.; Jafelicci, M.; Davolos, M.R. Luminescent properties of lattice defect correlation in zinc oxide. Int. J. Inorg. Mater. 2001, 3, 749754

[44] B. K. Meyer, H. Alves, D. M. Hofmann, W. Kriegseis, D. Forster, F. Bertram, J. Christen, A. Hoffmann, M. Straburg, M. A. Dworzak, U. Haboeck, A. V. Rodina, Bound exciton and donor-acceptor pair recombinations in ZnO, phys. stat. sol. (b), vol. 241, pp. 231 260, 2004

[45] G. A. Shi, M. Saboktakin, M. Stavola, and S. J. Pearton., Hidden hydrogen in as-grown ZnO, Appl. Phys. Lett., vol. 85, p. 5601, 2004

[46] B. K. Meyer, J. Sann, D. M. Hofmann, C. Neumann, A. Zeuner, Shallow donors and acceptors in ZnO, Semicond. Sci. Technol. , vol. 20, pp. S62S66, 2005.

[47] H. Morkoc, U. Ozgur, Zinc Oxide: Fundamentals, Materials and Device Technology., ISBN: 978- 3-527-40813-9, Ed. Germany: WILEY-VCH, 2009

[48] N. H. Nickel, Evgenii Terukov, ZnO: A material for micro-Oproelectronic applications, NATO science series, research output Vol. 194, 2004

[49] Xiaogan Liang, Zengli Fu, and Stephen Y. Chou*, Nano Lett. Vol. **7** No. 12 38403844 (2007)

[50] J.S. Lee, K. Park, M. I. Kang, I. W. Park, S. W. Kim, W. K. Chom, H. S. Han, S. Kim, ZnO nanomaterials synthesized from thermal evaporation of ball-milled ZnO powders, J. Cryst. Growth, vol. 254, p. 423, 2003

[51] Q. X. Zhao, P. Klason, M. Willander, Growth of ZnO nanostructures by vapor liquid solid, Appl. Phys. A, vol. 88, p. 27, 2007

[52] I. Ivanov, J. Pollmann, Electronic structure of ideal and relaxed surfaces of ZnO: A prototype ionic wurtzite semiconductro and its surface properties, Phys. Rev. B, vol. 24, p. 7275, 1981

[53] J. R. Haynes, Experimental proof of the existence of a new electronic complex in silicon, Phys. Rev. Lett. , vol. 4, pp. 361363, 1960

[54] Y. Gu, I. L. Kuskovsky, M. Yin, S. OBrien, G. F. Neumark, Quantum confinement in ZnO nanorods, Appl.Phys.Lett., vol. 85, p. 3833, 2004

[55] Z. N. Urgessa, Growth and Characterization of ZnO Nanorods using chemical bath deposition, NMMU PhD thesis, 2012

[56] B. Weintraub, Z. Zhou, Y. Li, Y. Deng, Solution synthesis of one-dimensional ZnO nanomaterials and their applications, Nanoscale, vol. 2, pp. 1573-1587, 2010

[57] G. Yi, C. Wang, M. Park, ZnO nanorods: synthesis, characterization and applications, Semicond. Sci. Technol., vol. 20, pp. S22-S34, 2005

[58] G. Yi, C. Wang, M. Park, ZnO nanorods: synthesis, characterization and applications, Semicond. Sci. Technol., vol. 20, pp. S22-S34, 2005

[59] M.D. Barankin, E. Gonzalez, A.M. Ladwig, R.F. Hicks, Plasma-enhanced chemical vapor deposition of zinc oxide at atmospheric pressure and low temperature, Sol.Energy.Mater.Sol., vol. 19, pp. 924930, 2007

[60] C. F. Bohren and D. R. Huffman, Absorption and Scattering of Light by Small Particles (JohnWiley and Sons, New York, 1983)

[61] D. Aaron R. Barkhouse, Richard Haight, Noriyuki Sakai, Homare Hiroi, Hiroki Sugimoto, and David B. Mitzi, Appl. Phys. Lett. **100**, 193904 (2012)

[62] R. R. LaPierre, A. C. E. Chia, S. J. Gibson, C. M. Haapamaki, J. Boulanger, R. Yee, P. Kuyanov, J. Zhang, N. Tajik, N. Jewell, and K. M. A. Rahman, Phys. Status Solidi RRL **7**, 815 (2013)

[63] P. Fan, U. K. Chettiar, L. Cao, F. Afshinmanesh, N. Engheta, and M. L. Brongersma, Nature Photon. **6**, 380 (2012)

[64] S. Z. Oener, S. A. Mann, B. Sciacca, C. Sfiligoj, J. Hoang, and E. C. Garnett, Appl. Phys. Lett. **106**, 023501 (2015)

[65] S. A. Mann and E. C. Garnett, Nano Lett. **13**, 3173 (2013)

[66] Young Heon Kim, Dong Woo Park, Sang Jun Lee, KwangMoo Kim, Yun Chang Park, J. Appl. Phys. **116**, 245101 (2014)

[67] G. Grzela, R. Paniagua-Domnguez, T. Barten, Y. Fontana, J. A. Snchez-Gil, and J. G. Rivas, Nano Lett. **12**, 5481 (2012)

[68] A. Tuniz, B. T. Kuhlmey, P. Y. Chen, and S. C. Fleming, Opt. Express **18**, 18095 (2010)

[69] Pavan Kumar Kasanaboina, Estiak Ahmad, Jia Li, C. Lewis Reynolds Jr., Yang Liu, Shanthi Iyer, Appl. Phys. Lett. **107**, 103111 (2015)

[70] A. Mirzaei, I. V. Shadrivov, A. E. Miroshnichenko, and Y. S. Kivshar, Opt. Express **21**, 10454 (2013)

[71] Ron Gurwitz, Rotem Cohen, Ilan Shalisha, J. Appl. Phys. **115**, 033701 (2014)

[72] X. Wang, K. L. Pey, C. H. Yip, E. A. Fitzgerald, D. A. Antoniadis, J. Appl. Phys. **108**, 124303 (2010)

[73] A. Kim, Y. Won, K. Woo, C.H. Kim, and J. Moon, ACS Nano **7**, 1081 (2013)

[74] S.K. Kim, R. W. Day, J. F. Cahoon, T. J. Kempa, K.D. Song, H.G. Park, and C. M. Lieber, Nano Lett. **12**, 4971 (2012)

[75] S. Albaladejo, R. Gmez-Medina, L. S. Froufe-Prez, H. Marinchio, R. Carminati, J. F. Torrado, G. Armelles, A. Garca- Martn, and J. J. Senz, Opt. Express **18**, 3556 (2010)

[76] Abdelilah Mejdoubi and Christian Brosseau **102**, 094104 (2007)

[77] A. D. Mallorqu, F. M. Epple, D. Fan, O. Demichel, and A. Fontcuberta Morral, Phys. Status Solidi A, **209**, 1588 (2012)

[78] Shaobo Shi, Jianping Xu, Xiaosong Zhang, and Lan Li, J. Appl. Phys. **109**, 103508 (2011)

[79] S. Ramadurgam and C. Yang, Scientific Reports **4**, 1 (2014)

[80] W. Liu, A. E. Miroshnichenko, R. F. Oulton, D. N. Neshev, O. Hess, and Y. S. Kivshar, Opt. Lett. **38**, 2621 (2013)

[81] Zi-Qiang Cheng, Yu-Ting Zhong, Fan Nan, Jia-Hong Wang, Li Zhou, Qu-Quan Wang, J. Appl. Phys. **115**, 224302 (2014)

[82] Kyung YongKo, Hyemin Kang, Jungkil Kim, Materials Science in Semiconductor Processing **27**, 297 (2014)

[83] Jingnan Cai, Yasuhiko Ishikawa, and Kazumi Wada, Opt. Express, **21**, 7162 (2013)

[84] J. D. Jackson, Classical electrodynamics, (John Wiley, New York, 1999)

[85] Leta Jule, Vadim Malnev, Belayneh Mesfin, Teshome Senbeta, Francis Dejene, and Kittessa Roro, Phys. Status Solidi B **252**, 2707 (2015)

[86] Reed, Jennifer, Electronic Theses and Dissertations. Paper 2781 (2013).

[87] R.Paniagua-Dominguez, D.R.Abujetas, L.S.Froufe-Perez, J.J.Saenz, J.A.Sanchez-Gil, Opt.Express **21**, 22076 (2013)

[88] Zhiyong Fan, Rehan Kapadia, Paul W. Leu, Xiaobo Zhang, Yu-Lun Chueh, Kuniharu Takei, Kyoungsik Yu, Arash Jamshidi, Asghar A. Rathore, Daniel J. Ruebusch, Ming Wu, and Ali Javey, Nano Lett. **10**, 3823 (2010)

[89] Otto L. Muskens, Jaime Gmez Rivas, Rienk E. Algra, Erik P. A. M. Bakkers, and Ad Lagendijk, Nano Lett. **8**, 2639 (2008)

[90] Jinyao Tang, Ziyang Huo1,Sarah Brittman, Hanwei Gao, and Peidong Yang, Nature Nanotechnology **6**, 568 (2011)

[91] X. H. Li, P. C. Li, D. Z. Hu, D. M. Schaadt, and E. T. Yu, J. Appl. Phys. **114**, 044310 (2013)

[92] Rodrguez-Gonzalez B., Attouchi F., Cardinal M. F., Myroshnychenko V., Stephan O., Garca de Abajo F. J., Luis Marzan, L. M. Kociak, M. Langmuir **28**, 9063 (2012)

[93] Haridas Kumarakuru a, Zelalem N. Urgessa, Ezra J. Olivier, Johannes R. Botha, Andre Venter, Johannes H. Neethling, Journal of Alloys and Compounds **612**, 154 (2014)

[94] Viktor Myroshnychenko, Jessica Rodriguez-Fernandez, Isabel Pastoriza-Santos, Alison M. Funston, Carolina Novo, Paul Mulvaney, Luis M. Liz-Marzanb, F. Javier Garcia de Abajo, Chem. Soc. Rev. **37**, 1792 (2008)

[95] Abdelilah Mejdoubi and Christian Brosseau, Phys. Rev. B **74** 165424 (2006)

[96] Shaobo Shi, Jianping Xu, Xiaosong Zhang, Lan Li, J. Appl. Phys. **109**, 103508 (2011)

[97] Zaiping Zeng, Christos S. Garoufalis, Andreas F. Terzis, and Sotirios Baskoutas, J. Appl. Phys. **114**, 023510 (2013)

[98] Abdelilah Mejdoubi and Christian Brosseau, J. Appl. Phys. **103**, 084115 (2008)

[99] A. Mejdoubi, M. Malki, M. Essone Mezeme, Z. Sekkat, M. Bousmina, and C. Brosseau, J. Appl. Phys. **110**, 103105 (2011)

[100] B. K. Meyer, H. Alves, D. M. Hofmann, W. Kriegseis, D. Forster, F. Bertram, J. Christen, A. Hoffmann, M. Straburg, M. A. Dworzak, U. Haboeck, A. V. Rodina, phys. stat. sol. (b), vol. 241, pp. 231-260, (2004).

[101] M. Mehrabian, R. Azimirad, K. Mirabbaszadeh, H. Afarideh, M. Davoudian, Physica E, vol. 43, pp. 1141-1145, (2011).

[102] B. K. Meyer, J. Sann, D. M. Hofmann, C. Neumann, A. Zeuner, Semicond. Sci. Technol. , vol. 20, pp. S62-S66, 2005.

[103] S. Anantha Ramakrishna and J. B. Pendry, Phys. Rev B. **67**. 201101 (2003)

[104] S. Sadofev, S. Blumstengel, J. Cui, J. Puls, S. Rogaschewski, P. Schfer, F. Henneberger, Applied Physics Letters 89 (2016) (20)

[105] M. Lange, C. P. Dietrich, K. Brachwitz, T. Bntgen, M. Lorenz, M. Grundmann, Journal of Applied Physics 112 (10)

[106] W.J. Yin, L. Dai, L. Zhang, R. Yang, L. Li, T. Guo, Y. Yan, Journal of Applied Physics 115 (2)

[107] P. J. T. Y. S. Wang, , P. O'Brien, The Journal of Physical Chemistry B 110 (43) (2006) 21412-21415

[108] B. U. Haq, R. Ahmed, S. Goumri Said, Solar Energy Materials and Solar Cells 130 (2014) 6-14

[109] G.B. Arfken, H.J. Weber, Mathematical Methods for Physicists, Elsevir Science, 2001.

[110] Y. Azizian Kalandaragh, A. Khodayari, Materials Science in Semiconductor Processing 13 (4) 2010 225-230

[111] F. Yakuphanoglu, S. Ilican, M. Caglar, Y. Caglar, Superlattices and Microstructures 47 (6) (2010) 732-743

[112] L. T. Jule, F. B. Dejene, K. T. Roro, Z. N. Urgessa, J. R. Botha, Physica B, 497 (2016) 71-77

[113] Leta T. Jule, Francis B. Dejene, Abdub G. Ali, Kittessa T. Roro, Aiat Hegazy, Nageh K. Allam, Essam El Shenawy, Journal of Alloys and Compounds 687 (2016) 920-926.

[114] N. Rana, S. Chand, A. K. Gathania, Ceramics International 41 (9, Part B) (2015) 12032-12037.

[115] B. Zheng, J. Lian, L. Zhao, Q. Jiang, Applied Surface Science 257 (13) (2011) 5657-5662

[116] A. Acharya, S. Moghe, R. Panda, S. Shrivastava, M. Gangrade, T. Shripathi, D. Phase, V. Ganesan, Thin Solid Films 525 (2012) 49-55

[117] Y. Sui, Y. Cao, X. Li, Y. Yue, B. Yao, J. Lang, X. Li, J. Yang, Physica E: Low-dimensional Systems and Nanostructures 70 (2015) 46-51

[118] L. Duan, X. Zhao, Y. Wang, H. Shen, W. Geng, F. Zhang, Journal of Alloys and Compounds 645 (2015) 529-534

[119] L. Jule, F. Dejene, K. Roro, Optics Communications 380 (2016) 186-194

[120] A. Kaushal, D. Pathak, R. Bedi, D. Kaur, Thin Solid Films 518 (5) (2009) 1394-1398

[121] S. Bai, S. Chen, Y. Zhao, T. Guo, R. Luo, D. Li, A. Chen, J. Mater. Chem. A 2 (2014) 16697-16706.

[122] J. Tauc, A. Menth, Journal of Non-Crystalline Solids 8 (1972) 569-585

[123] Y. Huang, M. Liu, Z. Li, Y. Zeng, S. Liu, Raman spectroscopy study of zno-based ceramic films fabricated by novel solgel process, Materials Science and Engineering: B 97 (2) (2003) 111-116.

[124] B. Yu, Y. Fu, P. Wang, Y. Zhao, L. Xing, X. Xue, Phys. Chem. Chem. Phys. 17 (2015) 10856-10860

[125] T. Dietl, H. Ohno, F. Matsukura, J. Gilbert, and D. Ferrand, Science 287, 1019 (2000)

[126] M. R. Wagner, G. Callsen, J. S. Reparaz, J.-H. Schulze, R. Kirste, M. Cobet, I. A. Ostapenko, S. Rodt, C. Nenstiel, M. Kaiser, A. Hoffmann, A. V. Rodina, M. R. Phillips, S. Lautenschlager, S. Eisermann, and B. K. Meyer, Phys. Rev. B 84, (2011) 035313

[127] S. W. Jung, S. J. An, and G. C. Yi, Appl. Phys. Lett. 80, 4561 (2002)

[128] N. H. Hong, J. Sakai, and V. Brize, J. Phys.: Condens. Matter 19, 036219 (2007)

[129] Y. Belghazi, G. Schmerber, S. Colis, J. L. Rehspringer, A. Dinia, and A. Berrada, Appl. Phys. Lett. 89, 122504 (2006)

[130] T. S. Herng, S. P. Lau, S. F. Yu, J. S. Chen, and K. S. Teng, J. Magn. Magn. Mater. 315, 107 (2007)

[131] D. Q. Gao, Z. H. Zhang, J. L. Fu, Y. Xu, J. Qi, and D. S. Xue, J. Appl. Phys. 105, 113928 (2009)

[132] B. B. Straumal, A. S. Mazilkin, S. G. Protasova, A. A. Myatiev, P. B. Straumal, G. Schutz, P. A. V. Aken, E. Goering, and B. Baretzky, Phys. Rev. B 79, 205206 (2009)

[133] Weijing Liu, Wenwu Li, Zhigao Hu, Zheng Tang, and Xiaodong Tang, J. Appl. Phys. 110, 013901 (2011)

[134] Serguei B. Orlinskii and Jan Schmidt, Pavel G. Baranov, Volker Lorrmann and Ingo Riedel, Daniel Rauh and Vladimir Dyakonov, Phys. Rev. B 77, 115334 (2008)

[135] Xuan Yu, Xiaoming Yu, Jianjun Zhang, Hongjun Pan, Mater. Lett. 161 (2015) 624-627

[136] D.E. Motaung, I. Kortidis, D. Papadaki, S.S. Nkosi, G.H. Mhlongo, J. Wesley Smith, G.F. Malgas, B.W. Mwakikunga, E. Coetsee, H.C. Swart, G. Kiriakidis, S.S. Raya, Appl. Surf. Sci. 311 (2014) 14-26

[137] K.J. Chen, T.H. Fang, F.Y. Hung c, L.W. Ji, S.J. Chang, S.J. Young, Y.J. Hsia, Appl. Surf. Sci. 254 (2008) 5791-5795

[138] Libing Duan, Xiaoru Zhao, Yajun Wang, Hao Shen, Wangchang Geng, Fuli Zhang, J. Alloys. Comp. 645 (2015) 529-534

[139] Jing Wang, Sichao Hou, Haoyuan Chen, and Lan Xiang, J. Phys. Chem. C 118 (2014) 19469-19476

[140] X.D. Zhang, M.L. Guo, W.X. Li, C.L. Liu, J. Appl. Phys. 103 (2008) 721

[141] F. Pan, C. Song, X.J. Liu, Y.C. Yang, F. Zeng, Mat. Sci. and Eng. R 62 (2008) 135

[142] M. Ghosh, N.Dilawar, A.K.Bandyopadhyay, A.K.Raychaudhuri, J. Appl. Phys. 106 (2009) 084306

[143] Shuai Ning, Peng Zhan, Qian Xie, Weipeng Wang, Zhengjun Zhang, J. of Mater. Sci. and Tech. 31 (2015) 969-978

[144] Kamal Baba, Claudia Lazzaroni, Mehrdad Nikravech, Thin Solid Films 595 (2015) 129-135

[145] D. Mondelaers, G. Vanholyland, H. Van den Rul, J. DHaen, M.K. Van Bael, J. Mullens, MRS Bull. 37 (2002) 901

[146] S. Suwanboon, P. Amornpitoksuk, A. Haidoux, J.C. Tedenac, J. Alloys. Comp. 462 (2008) 335-339

[147] Robert R. Piticescu, Roxana M. Piticescu, Claude J. Monty, Journal of the European Ceramic Society 26 (2006) 2979-2983

[148] Yung Kuan Tseng, Guo Jhan Gao, Shih Chun Chien, Thin Solid Films 518 (2010) 6259-6263

[149] T. Moe Brseth, B. G. Svensson, A. Yu. Kuznetsov, P. Klason, Q. X. Zhao and M. Willander, Appl. Phys. Lett. 89, (2006) 262112

[150] Jun-Ho Kima, Yoon Jong Moon, Sun Kyung Kim, Young ZoYoo, Tae Yeon-Seong, Ceram.Int. 41 (2015) 3064-3068

[151] Libing Duan, Xiaoru Zhao,Yangyang Zhang, Hao Shen, Ruidi Liu, Mater.Lett. 162 (2016) 199-202

[152] Pin Chuan Yao, Shih Tse Hang, Yu Shuan Lin, Wen Tsai Yen, Yi-Cheng Lin, Appl. Surf. Sci. 257 (2010) 14411448

[153] Samia Tabassum, Eiji Yamasue, Hideyuki Okumura, Keiichi N. Ishihara, Appl. Surf. Sci. 377 (2016) 355-360

[154] A. P. Thurber, G. L. B. II, G. A. Alanko, J. J. Anghel, M. S. Jones, L. M. Johnson, J. Zhang, C. B. Hanna, D. A. Tenne, A. Punnoose, Journal of Applied Physics 109 (7), 07C305 (2011).

[155] H. Fukushima, T. Kozu, H. Shima, H. Funakubo, H. Uchida, T. Katoda, K. Nishida, in: Joint IEEE Int. Symp., pp. 28-31 (2015).